AN ABSTRACT OF THE DISSERTATION OF

Hoda Tahami for the degree of Doctor of Philosophy in Civil Engineering presented on July 29, 2020.

Title: Monitoring and Prediction of Severe Weather Phenomena through GNSS Meteorology

Abstract approved:

_____

Dr. Jihye Park

While primary use of Global Navigation Satellite System (GNSS) is positioning, navigation, and timing (PNT), various GNSS applications have emerged over the past decades that includes GNSS meteorology. GNSS meteorology is the remote sensing of the atmospheric constituents in the neutral atmosphere – mostly in the troposphere - using GNSS to deliver information about the state of atmosphere. Precipitable water vapor (PWV) is the total amount of water vapor in a column of air above the earth surface that varies rapidly with short temporal and spatial-scale during severe meteorological phenomena. The amount of PWV contained in the neutral atmosphere can be retrieved from GNSS signals received by ground-based GNSS observations. GNSS is an excellent tool where it is not affected by weather conditions (e.g., presence of clouds, which derive a challenge to traditional weather monitoring technologies). Another benefit of GNSS is the data availability and accessibility.

This dissertation focuses on developing a PWV prediction model using GNSS observations to monitor and forecast the path of severe precipitations induced by

hurricanes. By using the GNSS-derived PWV and meteorological variables, the trend of the water vapor distribution is determined for the time frames of *before*, *during*, and *after* the severe precipitation. For each time frame a unique prediction model is developed suing a principle component regression (PCR). The developed model can forecast the severe precipitation track induced by a hurricane up to 24 hours in advance. In this dissertation the prediction models are examined using a proposed statistical model for different types of hurricanes. The case studies are: 1) Hurricane Mathew in 2016, 2) Hurricane Harvey in 2017, 3) Hurricane Irma in 2017, and 4) Hurricane Florence in 2018. In each hurricane case study the patterns of the GNSS-derived PWV fluctuations are analyzed. In particular, a sudden and sharp increment in the PWV followed by sharp descending trends was observed a few hours prior to the onset of precipitation. Also, the predicted PWV rate of change is dramatically increased prior to a severe precipitation. Moreover, in each case study, the probability of precipitation rapidly increased when the PWV reached a threshold in the range of 50 mm to 55 mm. The threshold is determined by analyzing the correlation between PWV fluctuations and occurrence of rainfall during the hurricane lifetime. The threshold is applied for classification of prediction models into the "*right before*", "*during*" and "*right after*" models based on the hurricane development stage. It should be emphasized that this study specially focuses on "*right before*" model, which is the most useful model to analyze the movement of hurricane.

The proposed method was validated by analyzing the distribution pattern of the predicted PWV residual, its magnitude, and the actual observed PWV in the test site. For a robust analysis considering the uncertainty from the measurement noise and other

error sources in the GNSS-derived PWV, the prediction residual at multiple sites in a local area are evaluated within the grids in the test area. The grid size is determined with the consideration of the test site and the geometric distribution of available CORS. The high probably location of heavy precipitation location by the grid-based prediction well agreed with the observed rain pattern that can be used for predicting the hurricane path. In addition, the negative correlation between the residuals of PWV measurements to the prediction model and the magnitude of precipitation was revealed. It shows the magnitude of the predicted model residuals can be used for hurricane tracking and potentially applies to evaluate the storm intensity.

This study demonstrates the feasibility of GNSS for monitoring severe precipitations and proves the effectiveness of the statistical model for forecasting the precipitation path during the hurricane that is potentially applied to a hazard early warning system.

Monitoring and Prediction of Severe Weather Phenomena through GNSS
Meteorology

by
Hoda Tahami

A DISSERTATION

submitted to

Oregon State University

in partial fulfillment of
the requirements for the
degree of

Doctor of Philosophy

Presented July 29, 2020
Commencement June 2021

Doctor of Philosophy dissertation of Hoda Tahami presented on July 29, 2020

APPROVED:

_____

Major Professor, representing Civil Engineering

_____

Head of the School of Civil and Construction Engineering

_____

Dean of the Graduate School

I understand that my dissertation will become part of the permanent collection of Oregon State University libraries. My signature below authorizes release of my dissertation to any reader upon request.

_____

Hoda Tahami, Author

ACKNOWLEDGEMENTS

TABLE OF CONTENTS

88

TABLE OF CONTENTS (Continued)

LIST OF FIGURES

LIST OF FIGURES (Continued)

LIST OF FIGURES (Continued)

LIST OF FIGURES (Continued)

LIST OF TABLES

LIST OF ACRONYMS

AIRS	Atmospheric Infrared Sounder
APC	Antenna Phase Center
APV	Antenna Phase Center Variation
ARP	Antenna Reference Point
APPS	Automatic Precise Point Positioning Service
CDMA	Code Division Multiple Access
CORS	Continuously Operating Reference Stations
CS	Cycle Slip
DCB	Differential Code Biases
dbHz	decibel-Hertz
ECI	Earth-Centered Inertial
EM	Electromagnetic
FCB	Fractional Cycle Bias
FDMA	Frequency Division Multiple Access
GNSS	Global Navigation Satellite System
GPS	Global Positioning System
IFB	Inter Frequency Biases
IGS	International GNSS Service
ISB	Inter System Biases
ITSO	Inter System Time-scale Offset
MODIS	Moderate Resolution Imaging Spectroradiometer
MERIS	Medium-Resolution Imaging Spectrometer
MCMF	Multi-Constellation and Multi-Frequency
NHC	National Hurricane Center

LIST OF ACRONYMS (Continued)

NWS	National Weather Service
PCO	Phase Center Offsets
PCV	Phase Center variations
PDOP	Position Dilution Of Precision
PNT	Positioning, Navigation, and Timing
PPP	Precise Point Positioning
PWV	Precipitable Water Vapor
PCR	Principal Component Regression
PROC	PWV ROC
DOP	Dilution of Precision
SPP	standard point positioning
SNR	Signal-to-Noise Ratio
PRN	Pseudorange Noise
TEC	Total electron content
TZD	Total Zenith Delay
TDP	Tropospheric Delay Parameter
UCD	Uncalibrated Code Delay
UPD	Uncalibrated Phase Delays
VLBI	Very Long Baseline Interferometry
WVR	Water Vapor Radiometers
ZHD	Zenith Hydrostatic Delay
ZWD	Zenith Wet Delay

CHAPTER 1

1. INTRODUCTION

1.1. Background

Short- and long-term variations in weather systems mostly rely on changes in atmospheric water vapor content. While its shortage in some areas may cause prolonged drought, its rising value over other areas may lead to frequent outbreaks of extreme weather; hence, obtaining and exploiting more high-quality observations about fluctuation in the water vapor content in the troposphere are particularly significant in the time of monitoring and forecasting extreme climate occasions. The moisture content of an atmospheric column is indicated by precipitable water vapor (PWV), which is the height of liquid water obtained by condensation of all water vapor within the atmospheric vertical column over a unit area. In general, a high PWV value prompts substantial precipitation or severe storm (Nykiel et al. 2019); therefore, PWV influences many atmospheric processes, and monitoring PWV fluctuations is helpful in identifying moisture sources and analyzing the development and evolution of severe weather phenomena, such as tropical cyclones and hurricanes. In addition, the atmospheric water content varies quickly in the short temporal and spatial scale during a meteorological phenomenon (Akilan et al. 2015; Benevides et al. 2015). Direct observations of the atmospheric water content by using traditional atmosphere-sensing techniques such as radiosonde and microwave radiometer provide limited capability with their poor temporal and spatial resolution and their operational and calibration cost; therefore, obtaining humidity observations with high spatial–temporal resolution is essential for reliable weather forecasting and climate monitoring. The Global Navigation Satellite System (GNSS) is now an established atmospheric sensing system that can provide high-quality water vapor observations in

the low atmosphere. Compared with traditional techniques, ground-based GNSS measurements have proven to estimate PWV in much improved spatial and temporal resolutions for local and regional water vapor fluctuations (Bevis et al. 1992; Shi et al. 2015). The capability of GNSS for analyzing PWV distribution for weather monitoring and forecasting is the focus of this dissertation.

1.2. Weather monitoring sensors and techniques

There is a variety of instruments and techniques to measure the amount of water vapor in the atmosphere. This section summarizes commonly-used techniques and instruments for measuring atmospheric water vapor content.

Radiosonde

A radiosonde is a balloon-borne instrument platform that can provide vertical profile information of the Earth's atmosphere throughout the troposphere and stratosphere. A radiosonde provides direct measurements of air pressure, temperature, and relative humidity. In particular, the integration of the vertical absolute humidity profiles from the surface to the top of the radiosonde profiles gives the atmospheric water vapor (Ning 2012). Each radiosonde is equipped with a GPS unit and a radio transmitter to measure its position and send the position data back to the ground receivers, respectively. By tracking the position of the radiosonde in flight via GPS, measurements of wind speed and direction are also obtained. All radiosonde sensors, together with the radio transmitter, are attached to a weather balloon, which lifts the radiosonde to altitudes exceeding 35 km and drifts it horizontally more than 200 km from the release point. Within 2 h after the radiosonde is launched, the vertical variations of observed weather elements are reported back to a receiving site. The data are processed, compared with data from other radiosondes, and utilized to project the climate conditions around the world (Ning 2012). The radiosonde data are used to project the current dynamic of the atmospheric parameters and are also used as inputs for weather forecasting models. The radiosonde is the most commonly used instrument for determining the atmospheric water vapor distribution, providing a long and continuous water vapor time series. However, the data quality varies in the upper atmospheric layers like troposphere and is reduced in the stratosphere, and high and low humidity (Schuler 2001).

When short-term fluctuations in atmospheric parameters are small, the radiosonde observations can effectively reflect the atmospheric condition over a location for hours. On the other hand, when the atmosphere varies greatly, for example, during severe weather phenomena, the radiosonde observations may not be valid for more than a minute and may not accurately represent the atmospheric condition over the area (Nash 2015). Moreover, the radiosondes require high-cost calibration, operation, and maintenance, which restrict their use by the US National Weather Service (NWS) and most other national agencies to only twice per day (Niell et al. 2001). Therefore, because they lack long-term stability and traceability and have low spatial coverage, radiosonde data are limited for climate research.

Water Vapor Radiometer (WVR)

Water vapor radiometers (WVR) are another type of instrument used to measure the troposphere brightness temperatures and estimate integrated water vapor contents in the troposphere along a given line of sight (England et al. 1992; Schuler 2001). The fundamental quantities measured by WVR are the line-of-sight brightness temperatures at three frequencies: 20.7, 22.2, and 31.4 GHz. The brightness temperatures are then converted into quantities at each frequency and combined to estimate the integrated precipitable water vapor content of the atmosphere (England et al. 1992). Although the vertical resolution of a WVR is lower than a radiosonde, it has the advantage of high temporal resolution on the order of seconds to minutes (Niell et al. 2001). For weather and climate monitoring, using space and ground-based microwave radiometers, atmospheric parameters such as the vertical profile of temperature and humidity and the amount of atmospheric water vapor can be derived with a high temporal resolution (Schuler 2001). However, the water vapor retrieval process requires a specific setting for required parameters for computing its variations with the season and

geographic location. Therefore, a WVR must be calibrated to the local conditions if obtaining water vapor quantities at the highest precision is desired (Bevis 1992; England et al. 1992). Moreover, WVRs are expensive tools with poor horizontal resolution, and their usage is limited to weather conditions without rainfall (Schumer 2001).

Very Long Baseline Interferometry

Very long baseline interferometry (VLBI) uses radio signals from an astronomical radio source such as a quasar at multiple radio telescopes on Earth or space as known positions. It measures the difference in the time of arrival of radio waves from the sources at stations on the Earth's surface by many telescopes simultaneously (Blewitt 2015). Because the telescopes are at different locations, they receive the signal from the radio source at different time intervals. The time delay can be estimated by connecting the received signals, which depends on the position of the radio source relative to the baseline between the telescopes and the distance between the pair of telescopes (Ning 2012). Using the estimated time delay, various parameters, including telescope positions, Earth rotation and orientation parameters, clock corrections, and zenith wet delay can be obtained (Ning 2012). Although the geodetic VLBI-derived zenith wet delay estimates can be used for continuous monitoring of water vapor over an area, the spatial resolution of VLBI-derived water vapor is a limiting factor. Less than 150 telescopes all over the world are used in geodetic VLBI, and 90% are located in the northern hemisphere (Ning 2012). This shows that the spatial coverage of the VLBI-derived water vapor is limited. However, VLBI observation is less affected by signal multipath than by other techniques because of the very high directivity of the VLBI telescope's antenna. Meanwhile, because the VLBI instrumentation is stable over time, the VLBI technique has the advantage of high long-term stability. Given these advantages, VLBI-derived

water vapor is a useful reference for detecting systematic errors in the water vapor obtained from other techniques (Ning 2012).

Satellite Imageries

Weather satellites, including polar-orbiting and geostationary satellites, are essential observational tools for weather and climate monitoring and forecasting. Observation is typically conducted using a visible and infrared portion of the electromagnetic spectrum. Smoke, haze, wind, clouds, and cloud systems are detected by a visible spectrum and are apparent in visible-light images (Hasler et al. 2008). Infrared satellite imagery is primarily used to determine cloud heights and types that are used to calculate land and surface water temperatures and to detect ocean surface features. Infrared satellite imagery can also be used effectively for detecting tropical cyclones using the differences in temperatures.

Satellite imageries monitor PWV over a wide area. Although a few multispectral images can measure even the vertical distribution of high-resolution PWV, the reliability of imagery-based PWV decreases with the presence of clouds. Space-borne microwave radiometers can acquire measurements for cloudy regions, but they are reliable only over the ocean in general (Gutman et al. 2001). One of the widely used space-based observation methods is the Moderate Resolution Imaging Spectroradiometer (MODIS). MODIS provides water vapor images using near-infrared channels twice a day for the entire world (Liu et al. 2013). The infrared MODIS observes water vapor with a 1 km spatial resolution under cloud-free conditions and/or above clouds over both land and ocean (Gao et al. 2003; Chen et al. 2017). Envisat satellites, including the Medium-Resolution Imaging Spectrometer (MERIS), measure the solar radiation reflected from the Earth's surface and clouds during the daytime in the visible and near-IR portion of the electromagnetic spectrum. MERIS-derived water vapor products above land or ocean surfaces under cloud-free

conditions are provided at two different spatial resolutions: 0.3 km for full-resolution mode and 1.2 km for the reduced-resolution model (Albert et al. 2001; Bennartz et al. 2001, Yu et al. 2017). However, in cloudy conditions, neither MODIS nor MERIS provides reliable water vapor observations above land or ocean surfaces (Yu et al. 2017). Similarly, the atmospheric water vapor can be measured globally by the Atmospheric Infrared Sounder (AIRS) with a vertical resolution of 2 km and a spatial resolution at nadir of 45 km. AIRS only operates in cloud-free or partly cloudy conditions (Bennartz et al. 2001; Chen et al. 2017).

Direct observations of the atmospheric water vapor that use the traditional atmosphere sensing techniques suffer from the lower temporal resolution and spatial coverage and high operational and calibration costs. GNSS is also capable of monitoring the perturbations in atmospheric water content (Bevis et al. 1992; Bordi et al. 2015; Benevides et al. 2015). Ground-based GNSS measurements have proven to estimate PWV in spatial and temporal resolutions for local and regional water vapor fluctuations that are much improved over traditional techniques (Bevis et al. 1992; Shi et al. 2015).

1.3. GNSS Meteorology for Weather Monitoring

While the primary use of the GNSS is positioning, navigation, and timing, various GNSS applications have emerged over the past decades that include GNSS meteorology. GNSS meteorology is the remote sensing of the atmospheric constituents in the neutral atmosphere—mostly in the troposphere—using GNSS to deliver information about the state of the atmosphere.

The troposphere is a non-dispersive medium for signals lower than 30 GHz, including GNSS signals whose frequency range is 1.1–1.6 GHz. Therefore, it cannot be easily eliminated by combining different frequency measurements on a single ray path. Thus, the quantity of the signal delay should be either modeled or estimated to mitigate its impact on high accuracy positioning. The tropospheric delay is related to meteorological parameters such as temperature, humidity, pressure, and the location of the receiver and satellites. About 90% of the delay comes from the hydrostatic component of the atmosphere, which can be modeled with high accuracy. However, the high and random spatial and temporal variations of water vapor in the troposphere make determining the wet component of the atmosphere difficult. The tropospheric wet delay takes about 10% of the total delay: typically, a few tens of centimeters.

GNSS meteorology is a proven technique to measure the atmospheric water vapor content in the troposphere. Although the atmospheric water vapor content can be measured by other methods as introduced in Section 1.2., GNSS meteorology provides several advantages coming from the nature of the GNSS technique as well as well-constructed infrastructure worldwide. The densely distributed GNSS tracking network stations and other ground-based GNSS networks stations provide high spatial and temporal resolution GNSS measurements. Moreover, operating costs are much lower than other techniques, thanks to the pre-existing GNSS infrastructure. The rapid growth in GNSS products and services has facilitated technical advancements in

meteorology, climatology, numerical weather modeling, and atmospheric science. The tropospheric PWV obtained by GNSS precise point positioning (PPP) technique provides a promising opportunity for real-time monitoring of the initiation and development of convective systems. The PPP technique provides a higher temporal resolution of tropospheric parameters using precise real-time products such as the International GNSS Service (IGS) real-time service. Although the close relationship between the PWV and a rainfall is revealed in numerous researches, fewer studies have focused on predicting the path of severe precipitation using GNSS derived PWV.

This dissertation proposes a novel method to forecast precipitation effectively during severe weather events, such as hurricanes and tropical storms, by applying the GNSS meteorology technique. This dissertation analyzes the temporal and spatial variation of the PWV retrieved from GNSS measurements to predict the path of severe precipitation during a hurricane. By taking advantage of GNSS-derived PWV data, this study suggests a multivariate statistical model for forecasting the path and intensity of severe rainfall induced by hurricanes.

This dissertation consists of five chapters. Chapter 1 describes the PWV measurement techniques and introduces GNSS for severe weather monitoring and forecast. Chapter 2 describes an introduction to the GNSS, including a brief history of satellite positioning systems, the functioning principles and provides a summary analysis of the various error sources and computation methods. It also describes characteristics of the ionosphere and troposphere as the signal propagation media and briefly discusses the main applications of the GNSS meteorology to give an overview of the state of the art of this research field. Chapter 3 introduces a multivariate statistical approach for forecasting a severe precipitation path during a hurricane by using GNSS-derived PWV and meteorological parameters. This chapter describes the prediction model

classification during the hurricane lifetime and the procedure to retrieve the models. Chapter 4 demonstrates the experiments, including the data processing procedure, descriptions of a case study, a technical description of the test implementations, and the experimental results. The processing results are shown for different hurricane case studies, and a quantitative comparison of the model performance is given. A comparison of the results relative to different scenarios and conditions is also given. The results are validated with the confirmed observation of the precipitation path and intensity provided by the National Hurricane Center (NHC). This chapter also examines the feasibility of applying the GNSS based forecasting model to different types of hurricanes to demonstrate the performance of the proposed prediction model in different geographic and climate characteristics. Chapter 5 summarizes the main contribution of this research and lists recommendations for future research.

CHAPTER 2

1. GNSS METEOROLOGY

While the primary use of the GNSS microwave signals is to determine the location of a receiving antenna, the information the signals carry can be used for atmospheric remote sensing because the waves passing the atmosphere are affected by the concentration of free electrons in the ionosphere and by the air density in the neutral atmosphere. GNSS meteorology utilizes GNSS radio signals to derive data of atmospheric constituents based on the remote sensing technique using a satellite platform (Pavelyev et al. 2010) and ground stations (Bender et al. 2010). GNSS receivers providing continuous GNSS measurement in a high spatial and temporal resolution is an excellent tool for studying the Earth's atmosphere. Therefore, GNSS meteorology can be a crucial method for numerous meteorological applications.

This chapter starts with a quick review of GNSS observables and parameters, then introduces the error sources and error mitigation strategies. The atmospheric regions and effects of the atmosphere on GNSS radio signal delays are then described in detail. The chapter ends with the literature review of severe weather monitoring using GNSS meteorology, describing the existing limitations and proposing the improvements through this dissertation.

2.1. Overview of GNSS

GNSS is a generic term describing any satellite constellation that provides worldwide positioning, navigation, and timing (PNT) services. Examples of GNSS satellite constellations include the USA's Global Positioning System (GPS), Europe's Galileo, Russia's GLONASS, and China's BeiDou navigation satellite system. The systems differ in their design and frequency range.

The fundamental observation of GNSS is the signal transmission time from a satellite to a receiver. Multiplying the signal's travel time from a satellite to a receiver by the speed of light in a vacuum gives the pseudorange between the satellite and the receiver. Note that the pseudorange is the travel distance of the signal that involves the range between a satellite and a receiver and whose additional terms consist of systematic and random errors. Two types of pseudoranges are obtained by correlating the code or the carrier phase in the received signal to the replica from the receiver, referred to as code or carrier phase measurements, respectively. For navigation purposes with an accuracy of a few meters, code measurements are typically used, whereas carrier phase measurements are mainly used for applications demanding centimeter-level or higher accuracy. Because the phase can be measured to 1% of the wavelength of the carrier signal, using the carrier phase measurements can lead to around 2 mm accuracy for the GPS constellation (Ning 2012). In comparison with GPS, observations from other GNSS can be down-weighted because of the mis-modeling of the satellite orbits and clocks (Kazmierski et al. 2018). An additional factor influencing the quality of GNSS observables is the characteristics of individual signals such as signal-to-noise and related propagation errors. (Cai et al. 2016; Kazmierski et al. 2018). The following sections focus on describing the GNSS positioning and its signal-processing concepts.

GNSS Positioning

The GNSS positioning is based on the trilateration concept, which measures the ranges between satellites and a GNSS receiver. However, these range measurements are affected by various errors, as presented in the equations (2-1) and (2-2) taken from (Li et al. 2015; Håkansson et al. 2017):

$$\Phi_{r,f}^{s,sys} = \rho_r^{s,sys} + c\left(t_r - t^{s,sys} + b_{r,f}^{s,sys} - b_f^{s,sys} + \tau^{s,sys}\right) - I_{r,f}^{s,sys} + m_r T_r + \lambda N_{r,f}^s + \varepsilon_{r,f}^{s,sys} \quad (2-1)$$

$$P_{sig,r}^{sys,s} = \rho_r^s + c\left(t_r - t^{s,sys} + d_{r,f}^{s,sys} - d_f^{s,sys} + \tau^{s,sys}\right) + I_{r,f}^{s,sys} + m_r T_r + e_{r,f}^{s,sys} \quad (2-2)$$

where

$$I_{r,f}^{s,sys} = k_f^{sys} I_{r,1}^{s,sys} \; ; \; k_f = \frac{\lambda_1^2}{\lambda_f^2},$$

where the superscripts s and sys refer to a satellite and the type of GNSS constellation; the subscript r and f indicate a receiver and a carrier frequency, respectively; ρ_r^s denotes the geometric distance between the satellite s and the receiver r; c is the speed of light; $t^{s,sys}$ and t_r are the clock biases of satellite and receiver; $N_{r,j}^s$ is the integer ambiguity; $d_{r,f}^{s,sys}$ is the frequency-dependent receiver hardware code bias (or uncalibrated code delays [UCD]) concerning satellite s and $d_f^{s,sys}$ is frequency-dependent satellite hardware code bias (or UCD); and $b_{r,f}^{s,sys}$ and $b_f^{s,sys}$ are the frequency-dependent receiver and satellite hardware phase bias (or uncalibrated phase delays [UPD]). When multiple GNSSs are used for one positioning solution, different reference times and reference frame between the GNSSs should be taken into account. Therefore, τ^{sys} is the time offset for the system time of the GNSS system concerning a chosen reference; λ_j is the wavelength; $I_{r,1}^{s,sys}$ is the line of sight ionospheric delay of the signal path at frequency f, the ionospheric delays at different frequencies where k_f^{sys} is the frequency-dependent multiplier factor which is independent of the satellite pseudorange noise (PRN) code; and T_r is the tropospheric zenith wet delay at the station r; it should be noted that the slant tropospheric delay consists of the dry and wet components. Each component is being expressed by its individual zenith delay and mapping function. A priori model is usually used to correct the dry component of the tropospheric delay, whereas the wet part of the tropospheric delay is estimated from the GNSS observations; m_r is the wet mapping function; $\varepsilon_{r,f}^{s,sys}$ and $e_{r,f}^{s,sys}$ denote the sum of measurement noise and multipath error for the carrier phase and pseudorange observations. The relativistic effects, Sagnac effect, tidal

loadings, phase windup (only for carrier phase), antenna Phase Center Offsets (PCOs), and variations (PCVs) of satellites and receivers should also be considered to be either corrected or modeled (Kouba, 2009). Note that these are not explicitly included in the equations above. All the variables in the above equations are expressed in meter except for the ambiguity and UPDs, which are expressed in cycles.

GNSS Observables

The GNSS observables indicate the signals where measurements yield the range or distance between the satellite and the receiver. Two types of observables occur: Pseudorange (code) and carrier-phase measurements. In general, the travel time of the received signals in a GNSS receiver can be estimated by analyzing the time shift required to align the code received from a satellite with a replica simultaneously generated in the receiver. This estimated signal travel time is then multiplied by the speed of light to obtain the code measurements, which is sometimes called code pseudorange. The prefix "pseudo" is used because of a difference between this quantity and the actual receiver satellite distance caused by error sources. The code measurements for each constellation are formulated as follows:

$$P_{r,f}^G = \rho_r^G + c\left(t_r - t^G + B_{rG,f} - d_f^G\right) + k_{fG} I_{r,1}^G + m_r^G T_r + e_{r,f}^G \quad (2-3)$$

The carrier phase measurements consist of two parts: an integer and a fractional part, in terms of carrier cycles. A receiver can directly measure the fractional part of the carrier phase, whereas the integer part can be estimated in post-processing using specific algorithms (referred to ambiguity solutions). The phase difference between the signal transmitted by the satellite and received by the receiver and the signal replica generated in the receiver is measured in the receivers as phase measurement. Because of the unknown initial integer number of carrier cycles during the signal travel between satellite and receiver, the phase measurement contains the ambiguity term.

The full mathematical expression for GNSS pseudo-range measurement on Φ_f frequency is as follows:

$$\Phi_{r,f}^G = \rho_r^G + c\left(t_r - t^G + b_{rG,f} - b_f^G\right) - k_{fG}I_{r,1}^G + m_r^G T_r + \lambda_{fG}N_{r,d}^G + \varepsilon_{r,d}^G \ (2-4).$$

GNSS Parameters

Many parameters in GNSS observables can be modeled or corrected by applying external models. The parameters are listed below.

Solid Earth Tides

The gravitational forces of the Sun and the Moon cause variations in the Earth's crust and are called solid Earth tides. The effects of solid Earth tide on positioning error is up to several decimeters and can be computed and corrected with good approximation. The movements of the Earth's crust can be detected by GNSS geodetic networks. The periodic vertical and horizontal site displacements caused by tides can be modeled using geophysical models and spherical harmonics. These harmonics are weakly dependent on station latitude and tidal frequency that must be considered when a position precision of 1 mm is desired. The Love number h_{nm} and the Shida number l_{nm} with the spherical harmonic degree (n) and order (m) characterize site displacements caused by the tidal effect of the gravitational force from the Sun and Moon. The latitude dependency and a small inter-band variation are caused by the Earth's ellipticity and the Coriolis force, which is due to the Earth's rotation. It should be noted that solid Earth tides errors are much larger than the minor effects of polar tides or ocean loading (Kouba 2009).

Pole Tides

Polar motion is the change of the Earth's spin axis related to the Earth's crust. The change in the Earth's centrifugal potential causes periodical deformations. Polar motion affects the determination of the receiver and satellite position in the reference frame and causes up to a few

centimeters of positioning error. The effects of the polar tide cannot be neglected for applications required sub-centimeter position precision, and the polar tide corrections must be applied. Contrary to the effects of the solid Earth tides and the ocean loading, the pole tides do not approach zero over a 24 h period (Kouba 2009).

Ocean Tide Loading

Ocean tides are caused by a temporal deformation of the ocean mass and the relative load on the Earth's crust. Similar to solid Earth tides, ocean tide loading is mainly influenced by diurnal and semi-diurnal periods (Lou 2013). While the magnitude of the displacement is smaller than those caused by the solid Earth tide, ocean loading is still considered because it has a localized impact and is not consistent (Kouba 2009). The ocean tides can be modeled as a harmonic series of the main tidal constituents. The main tidal constituents include the semi-diurnal, the diurnal, and the long-period tidal constituents. Each main tidal constituent has its own amplitudes and phases. The magnitude of the amplitudes and phases depends on the station's location. To estimate the amplitudes and phases of these main tidal constituents, a global ocean tide model such as FES2004 is used (Kouba 2009). A global ocean tide model can be developed using the sea surface height data provided by tide gauges and satellite altimeters. Using the Green's function obtained by the Earth's elastic models, the station-specific amplitudes and phases of these main tidal constituents can be estimated. The amplitudes and phases of the main tidal constituents for each station can be obtained directly and free of charge through the online ocean loading service of the Onsala Space Observatory at froste.oso.chalmers.se/loading (Kouba, 2009). With the obtained station-specific amplitudes and phases of these main tidal constituents, the site displacement caused by ocean tide loading can be estimated (Bayram 2016). In general, the ocean loading tidal corrections can reach up to 100 mm. Worth mentioning is that the closer the site is to the ocean,

the more significant ocean tide loading displacements can be produced. Ocean loading effects can be neglected for stations located far from the ocean. This effect is also negligible for any static positioning over a 24 h period and also for any single epoch positioning that requires less than a 5 cm precision level (Antonini 2013). In other positioning modes such as kinematic or precise point positioning near the coastal area, even though the observation period is less than 24 h, ocean load effects must be taken into account. Moreover, the ocean load effects must be taken into account when the tropospheric delay or clock parameters are required in the positioning solutions, even for a more than 24 h static precise point positioning. This effect can be safely neglected if the station is far from the nearest coastal region (>1000 km). Otherwise, the effects of ocean loading should be considered in the tropospheric and clock solutions (Antonini 2013).

Relativistic Effects

An inertial cartesian coordinate system is used in GNSS to measure and determine the satellites' orbits and is called the Earth-Centered Inertial (ECI) reference system. The origin of this reference system, located at the center of mass of the Earth, the Earth's equatorial plane corresponds with its x-y plane and the x, y axis is directed toward determined positions over the celestial sphere; the z axis is perpendicular to the x-y plane oriented to the north direction. Because of the extensive motion velocities in GNSS satellites, the circular shape of satellites' orbit, the Earth's rotation, and the existence of a gravitational potential difference between the satellite and the receivers, the relativistic effects cannot be negligible. The difference between the gravitational field at the satellite and the observation site and the motion of the satellite influences the frequency of the satellite clock (according to general and special relativity). According to general relativity theory, clocks at high altitudes above the Earth and moving with low relative velocity run faster than clocks located on the Earth's surface and moving with higher velocity because of less gravity

and according to the special relativity theory. This relativistic effect should be added to the precise satellite clock product (Kouba, 2009; Takasu, 2013). Furthermore, in the presence of the Earth's gravitational field, the speed of light changes, thus affecting signal propagation. As a result, the magnitude given by (Subirana et al. 2013) should be added to the geometric range. Besides, during the signal propagation from the satellite to the receiver, the Earth rotates, and the related relativistic effect known as the Sagnac effect should be formulated. A GNSS receiver clock located on the Earth's surface is moving about 500 m/s at the equator because of the Earth's rotation. This causes 10 ns receiver clock error (1 ns causes 30 cm range error) after 3 h (Hofmann et al. 2008). However, this effect is generally corrected by the receiver software or absorbed by the receiver clock offset. Therefore, the relativistic effect corrections can be expressed as a combination of following corrections:

- Relativistic effect corrections applied to carrier-phase measurements (in meters)

- Relativistic effect correction applied to the satellite precise clock correction (in seconds)

- Relativistic effect correction applied to geometric range (in meters)

In general, even after applying the corrections, some relativistic effects always remain because of the orbit oscillations and the perturbations in Earth's gravitational field.

Receiver Clock Bias

The geometric distance between each satellite and a receiver can be accurately determined using precise measurement of the signal travel time with a clock that was set precisely to system time (Hafmann et al. 2008). The clocks in receivers are quartz crystal clocks with different quality than satellite clocks. The precise and more stable atomic clocks are used in satellites. Therefore, there is always an offset between receiver clocks on the ground and satellite clocks concerning the

true time system, which is known as receiver clock bias. This bias causes a difference between a measured distance from the receiver to the satellite and the true geometric range, which should be considered in the positioning solution (Hafmann et al. 2008).

Satellite Clock Bias

The drift in the satellite clock leads to significant errors in the positioning solutions. The satellite clock is monitored by and compared with the GNSS ground control system's clock. The estimate of the satellite clock offset is provided for the users in navigation messages (Hafmann et al. 2008). The clock errors can be compensated by using real-time corrections and precise clock products.

Antenna Phase Center Offsets

The antenna phase center does not coincide with the antenna's geometrical center, making the antenna phase center offset. To model the effect of the antenna phase center, the contribution of the receiver- and satellite-related antenna phase centers must be individually corrected. The typical error is of the order of a few centimeters. It should be noted that the phase center is determined by considering the elevation angle-dependent variation of the incoming signal, which is also dependent on the signal frequencies (Sanz Subirana et al. 2011a). The antenna phase center (APC) varies with the frequency of the signals. Therefore, the antenna reference point (ARP), a point tied to the base of the antenna, is additionally introduced as a more accurate reference (Sanz Subirana et al. 2011b). Manufacturers usually provide technical information about the APC and ARP, compiled by IGS and published as ANTEX files to be utilized for receiver antenna correction. The satellite position in orbit is determined with respect to the center of the mass of the satellite, whereas the actual observation refers to the antenna's phase center. The satellite positions provided by the broadcast ephemeris refer to the satellite's antenna phase center, whereas those

from the precise orbits and clocks refer to the satellite mass center, necessarily considering the Phase Center Offset (PCO) vector. The Phase Center Variation (PCV) should also be considered because the electrical phase center of the antenna varies with the signal frequencies and signal directions. The offset between the center of the mass of the satellite and the antenna phase center is difficult to measure because the phase center depends on the electronic design rather than a mechanical point. The phase center's offset is the direction of the z-axis toward the Earth and the direction of the x-axis, which is on the plane containing the sun in the body frame (Zhu et al. 2003).

Phase Wind-Up Correction

The electric field vector of the signal transmitted by GNSS satellites rotates with an angular frequency. Assuming the receiver spins rapidly (with an angular frequency), the received frequency consists of the two angular frequencies. The resulting phase accumulation is called phase windup (Hofmann et al. 2008).

Hardware Biases

Hardware bias is usually a significant concern in point positioning if code and phase observations are combined. For generating the carriers and the modulations, an in-satellite oscillator with a base frequency (f0) of 10.23 MHz is generally used. The satellite hardware can cause delays when these components are combined. A receiver can also cause a similar delay when the replica of the signal is generated in the receiver. The intra-frequency and inter-frequency differential signal delays caused by satellite and receiver hardware can be estimated with numerous techniques. However, the correlation between GNSS hardware biases, clock offsets, and ambiguity parameters can create complications in determining the absolute delay for a particular signal or modulation. Typically, the hardware biases are merged with the abovementioned parameters (Banville et al. 2008).

GNSS Preprocessing and Error Mitigation Algorithms

Data Screening

- ***Satellite Availability/Dilution of Precision (DOP)***

The satellite visibility and position dilution of precision (PDOP) are significant factors for evaluating the performance of satellite-based positioning technology. The PDOP describes the propagation of random errors in GNSS observations into the noise levels of the unknown parameters (Pan et al. 2017). Therefore, it can be utilized to indicate the geometric strength of observations and the accuracy level of positioning solutions. In multi-GNSS standard point positioning (SPP) or PPP, in PDOP calculation, the mismatch between different satellite systems is considered. The incompatibility of the PDOP calculation may be considered if the satellite constellations are incompatible. In this situation, there is an inter-system time-scale offset (ITSO) that is broadcast to the users through the broadcast ephemeris. In GNSS standard point positioning, the time group delay (TGD) and inter-signal correction (ISC) are two factors in the correction of the satellite-dependent code biases.

On the other hand, in the parameter estimation process, the receiver-dependent code biases will be merged into the receiver clock. The ITSO in broadcast navigation messages also includes the receiver-dependent inter-system code biases relative to the biases for the selected reference satellite system (Pan et al. 2017). To improve the structure of the normal equation, the condition number of the design matrix is introduced in the reference satellite selection method because the condition number indicates an error in the normal equation and improves positioning accuracy and reliability (Gao et al. 2017).

- ***Signal-to-Noise Ratio (SNR)***

The raw carrier-to-noise ratio is stored as SNR observations in the data records and expressed in decibel-Hertz (dbHz). SNR data are routinely recorded by receivers that are sensitive to carrier phase multipath. SNR data is reported in RINEX data files as observable types, and record "raw signal strength" or SNR values as given by the receiver for the phase observations. The ratio of the carrier power indicates the signal power of the tracked satellite and the noise density present in the measurement (Bilich et al. 2007). Signal strength is shown by a scale of 1 to 9. The minimum signal-to-noise ratio is represented by 1; for the medium rate, 5 is used, a maximum possible rate of signal strength is indicated by 9, and 0 or blank represents an unknown rate.

- ***Clock Jumps***

If receiver clock jumps are not completely detected, cycle slip detection can fail, which can cause a repeated re-initialization process or even prevent a convergent positioning solution, resulting in significant errors in the PPP solution. In the occurrence of clock jumps, discontinuities mainly influence the pseudorange, carrier phase measurement, and time parameters (Guo et al. 2014). Clock jumps can result in GNSS observation inconsistency, similar to cycle slips. Note that the temporary loss of lock in the carrier phase tracking causes discontinuities of an integer number of cycles in the carrier phase measurements and leads to cycle slip. However, clock jumps are continuous unique discontinuities introduced by receiver manufacturers to control lock offset size. The resulting inconsistency between pseudorange and carrier phase measurements from clock jumps can be considered receiver clock bias or ambiguity parameter in the positioning solution. However, the clock jumps can be corrected without data screening by applying appropriate data processing techniques such as Kalman filtering (Guo et al. 2014).

Clock jumps cannot be picked up by commonly used linear combinations, such as geometry free linear combination, that are used in cycle slip detection because the phase measurements on all frequencies are identically affected. Depending on the receiver type, clock jump effects show a "sawtooth"-like signature when plotting the time series of the carrier phase or code measurements (El-mowafy et al. 2015). El-mowafy utilized the Multi-Constellation and Multi-Frequency (MCMF) GNSS observations, including both carrier phase and code measurements, to detect and repair the clock jumps. In the proposed algorithm, the average linear combination of code and carrier phase measurements, together with a spline function, is used to approximate the data for a preset time interval before each measuring epoch.

Cycle Slip Detection and Repairs

A Cycle Slip (CS) is a sudden discontinuity in carrier phase measurements represented by an integer number of cycles. Failure or high dynamics of a receiver, signal blockage or interruption, and low signal-to-noise ratio can lead to CS. They must be detected and corrected using the positioning process before the carrier phase (Dai 2012). One of the conventional ways to handle cycle-slips is the following:

1. Detection: Detect CS by observing signals epoch-by-epoch (given that a CS is a random event).

2. Determination: Quantify the amplitude of the detected CS.

3. Validation: Validate the corrected CS.

4. Removal: Subtract the CS after the values are fixed and pass the validation.

Note that the above strategy demonstrates the case of the cycle slip repair. Alternatively, the contaminated observation can be removed entirely, which does not require the

determination/validation steps. Xiao et al. (2018) classified the cycle slip detection and correction algorithms into the following three categories.

The first group contains algorithms based on the analysis of the GNSS observations time series. Cycle slips are determined as sudden jumps in a continuous and smooth signal, which can be modeled by multi-polynomial regression. The TurboEdit algorithm is a typical example of a dual-frequency CS algorithm. TurboEdit is the combination of the Hatched Melbourne Wubbana approaches and ionospheric residual combinations. With high sampling rate data and under high ionospheric activity circumstances, some modifications should be applied to the TurboEdit algorithm to enhance the cycle slip detection (Cai et al. 2013). Another method for CS and outlier detection in this category is to apply Bayesian theory (Lacy et al. 2008; Zhang et al. 2013). The approaches in the first category need the continuity of carrier phase measurements for several minutes before and after a cycle slip (Huang et al. 2016).

The methods in the second category are based on the optimal combinations of multi-frequency observations. The main algorithm in this category is the linear combinations of GNSS observations to eliminate the effects of other parameters, such as geometric terms or ionospheric errors. This type combines multiple carrier phase measurements to mitigate the geometry and all non-dispersive effects (Li et al. 2016). Even after the removal of the first-order ionospheric effect, the performance of the CS detector is influenced and degraded by the high ionospheric activity, specifically with a low sampling rate data (i.e., $\Delta t \geq 30$ s). The occurrence of cycle slips is independent on each signal; therefore, to detect all possible jumps, two independent combinations must be utilized. When two independent combinations are simultaneously used, the inappreciable jumps produced by the combination of ΔN_1 and ΔN_2 in the geometry-free combination can safely detect (Navpedia website). Dai et al. (2009) proposed one example combination algorithm in

which two geometry-free combinations of triple frequency carrier phase measurements are employed for cycle slip detection. Further, triple-frequency carrier phase combinations are used in Huang et al.'s (2016) proposed method to detect and repair cycle slips. De Lacy et al. (2012) presented more than five types of linear combinations based on triple-frequency GNSS measurements for real-time cycle slip detection and repair. Zhao et al. (2017) employed undifferenced triple-frequency GNSS measurements in independent linear combinations for real-time cycle slip detection and correction. As described, a common characteristic of the triple-frequency signals' CS detection methods is the forming of optimal combinations to mitigate the presence of geometric and ionospheric errors (Xiao et al. 2018).

The third category includes the algorithms employing geometry-based and time-differenced models. Banville and Langley (2013) and Zhang and Li (2012) investigated the dual-frequency CS correction algorithm based on a time-differenced model. Similarly, Zhang and Li (2016) applied triple-frequency observations and investigated adding the third frequency on cycle slip detection. In their model, time-difference observation equations are formed between two consecutive epochs and all satellite equations are processed in an integrated adjustment showing great potential for carrier frequency identification of cycle slips (Xiao et al. 2018). However, if discontinuity is detected for one satellite, the algorithm flags all carrier phase frequencies as detected cycle slips (Banville and Langley 2013).

Satellite and Receiver Instrumental Delays and Differential Code Biases

Satellite and receiver hardware biases are one of the main issues in combining code and phase observations in precise point positioning. The carriers and the modulations are generated at the fundamental frequency (f_0) of 10.23 MHz by a satellite oscillator. In general, several delays can occur when code and phase observations are combined. Similarly, when the replica of the

signals is generated in the receivers, delays can occur. Instrumental biases are different based on different codes and frequencies. A separated bias is assigned to each pseudorange observable, including C1 (C/A code on the f_1 frequency), P1 (P code on the f_1 frequency), and P2 (P code on the f_2 frequency). Because of the changes in satellite hardware conditions (such as temperature and wear), and because the hardware biases of satellite and receiver are merged into measurements, the absolute value of instrumental biases cannot be directly retrievable. However, different methods can estimate the intra- and inter-frequency delays for each signal, determination of the delay's absolute value for a particular signal is very complicated. The correlation of the GNSS parameters, including the instrumental biases, clock offsets, and carrier phase ambiguity, leads to the complexity of delay's absolute value retrieval (Banville et al. 2008). Therefore, the combination of biases, which is referred to as Differential Code Biases (DCB), is commonly used in positioning. For error correction purposes, DCB cannot be applied to a single observation but is applied to a combination of observables. The hardware code and phase bias in satellites and receivers are described separately in the following sections.

- ***Satellite and Receiver Hardware Code Biases***

Satellite clock corrections from the broadcast navigation message or IGS products, together with the DCB corrections, are commonly used to eliminate the Satellite hardware code biases from the code observations. For the receiver hardware code biases, some parts of the biases are absorbed in the receiver clock parameter, and the remaining parts propagate into the code residuals and other estimated parameters such as the receiver coordinates (Banville et al. 2008). In PPP, the receiver hardware delays are assumed to be consistent for the satellites of the same type of GNSS constellation, including GPS, Galileo, and BeiDou, which uses the Code Division Multiple Access (CDMA) technique. While it cannot be applied to GLONASS, which employs frequency division

multiple access (FDMA). For GLONASS satellite constellation, the receiver hardware bias will differ for each satellite with different frequencies (Li et al. 2015; Håkansson et al. 2017) and is usually known as inter-frequency biases (IFB). The code IFB must be taken into account in the standard point, positing, and fixing the ambiguity parameters in PPP (Hakansson et al. 2017). Note that the code IFB is dependent on the receiver's firmware version of and antenna type. The code IFB is stable over time; therefore, pre-calibrated values can be utilized in positioning solutions (Antonini 2013). Moreover, because of the various signal structure in different GNSS constellation satellites and different types of frequencies, the code biases are not the same in a multi-GNSS receiver. The differences between these biases are usually called code inter-system biases (ISB) (Hakansson et al. 2017). Code ISB is constant over time and similar in the same type of receiver. Unlike phase ISB, code ISB can be estimated unambiguously as an unknown parameter. When a single satellite transmits two GNSS signals, a time delay between two transmitted signals will occur, known as DCB. Note that DCB includes code biases in the receiver hardware at reception as well as satellite hardware code biases in transmission (Antonini 2013). The DCB is a crucial factor, especially in the application of TEC estimation from the pseudorange and phase data of multi-constellation signals. Even a small amount of DCB equal to 1-ns leads to TEC estimation error as large as 2.9 TECU. For some receivers, the systematic DCB variations, including the seasonal and environmental variations (such as temperature and humidity changes), can cause up to 20 TECU in the TEC estimation (Antonini 2013; Mylnikova et al. 2015).

- *Satellite and Receiver Hardware Phase Biases*

The receiver and satellite hardware can also cause delays in the carrier phase observations. Similar to code biases, the phase delays are also different for GNSS constellations, and their differences are known as phase inter-system biases (ISB). Although satellite phase biases are

different for each satellite and carrier frequency, receiver phase biases are frequency-dependent and are the same for each satellite. The satellite phase biases are merged into the carrier phase ambiguity parameters; therefore, this aspect becomes a major concern for ambiguity resolution. Receiver phase biases are absorbed by the receiver clock, the phase ambiguities, and estimated coordinate (Banville et al. 2008). In GNSS constellations with an identical carrier phase-frequency between the systems (such as combined GPS/Galileo), the double-difference technique can be applied to preserve the integer nature of ambiguities. For the fixed solution in PPP, these delays cause an issue in resolving the integer ambiguity if they are not adequately corrected. Because of satellite phase biases, fixing the phase ambiguities to integer cannot be done in the same way as the double-differenced relative positioning (Hakansson et al. 2017).

Therefore, the full phase ambiguities resolution in a fixed solution is constrained not only by the satellite phase biases but also by the receiver side phase IFB. Moreover, not only do the receiver's hardware biases contain the phase IFB, but the satellite phase bias can also include the phase IFB. Because the phase IFBs and the satellite phase biases are highly correlated, they cannot be separated for the correction. Unfortunately, these biases increase the number of unknown parameters in the positioning solution, which tends to derive a rank deficiency (Teunissen et al. 2015). Therefore, the phase biases should be determined beforehand in case of PPP ambiguity fixed solution because the receiver hardware biases are often assumed to be the same for all satellites in a constellation. Because there is no correlation between the receiver phase bias concerning a satellite and the phase ambiguity, the receiver phase bias can be canceled out with the receiver clock error in the single differences between satellite procedure. Therefore, for fixing the ambiguities in PPP, the satellite clock error and the satellite phase biases should be corrected. The satellite phase biases have short-term stability and must be provided on the user side every 15

minutes. The corrections for satellite phase bias can be in the form of a fractional cycle bias (FCB) (Ge et al. 2008; Geng et al. 2012). In the positioning process, the satellite phase bias can also be integrated into the satellite clock corrections (Collins et al. 2010).

Multipath

The multipath has an impact on both GNSS observables, code, and carrier phases. However, the carrier phase observations are less affected between different types of receivers. The direct effects of multipath error are mainly on the accuracy of pseudorange observations, which are critical in a standard point positioning technique (Tahami et al. 2018). The maximum multipath error could be approximated as half of the code chip length and one-quarter of carrier-phase wavelength. Therefore, the magnitude of the multipath error could be a maximum 150 m for C/A code, 15 m for P(Y) code, and about 5 cm for the carrier-phase measurements. However, its magnitude is generally about 1–5 m in the pseudo-range measurements and 1–5 cm in carrier-phase measurements (Hofmann et al. 2008). The t effects of multipath cannot be eliminated through modeling or differencing techniques. However, its impact may be reduced by an appropriate antenna design (choke ring antenna), selecting the sites protected from highly reflective objects, or applying a mitigation technique. Also, the risk of multipath interference can be reduced if the satellites at low elevations are discarded by setting an elevation cutoff angle. The pseudorange multipath can be estimated by eliminating the satellite-receiver geometry and all atmospheric effects through the linear combination of dual-frequency observations. However, utilizing these combinations cannot resolve the phase ambiguities and eliminate any differential biases. Although the differential biases do not significantly change over time, the ambiguities cannot be assumed as constant over time because of the presence of CSs (Vaclavovic 2016). Thus, the CSs must be detected (and, optionally, repaired) before the multipath estimation. In addition

to the linear combination of various frequencies, the detection and mitigation of the multipath interference can be performed by comparing the carrier-power-to-noise ratio (C/N0) with different frequencies. After detecting the multipath, the affected signals may be either excluded altogether or down-weighted in the position solution (Strode et al. 2016). Another multipath mitigation approach is to select signals by checking the consistency. Because none of the available methods for eliminating the multipath effects on GNSS positioning are entirely reliable, specifically in real-time applications, the effects of multipath are critical for the precise positioning.

Atmospheric error

In GNSS, the Earth's atmosphere is classified into different layers based on their physical characteristics and the impacts of electromagnetic (EM) spectrums. Structure-wise, the atmosphere is divided into the neutral atmosphere and the ionosphere. Although the neutral atmosphere includes the troposphere and the stratosphere, the troposphere is usually used as a representative of the neutral atmosphere in the GNSS community (Hofmann et al. 2008; Antonini 2013). The troposphere can be separated into dry (0–40 km) and wet (0–11km) components. The dry component consists of dry gas molecules and occupies about 90% of the total tropospheric error, whereas the wet component consists of the water molecules and occupies about 10% of the total tropospheric error. The dry tropospheric error can be modeled successfully at zenith direction, but the wet tropospheric error cannot be modeled easily because the atmospheric water content varies considerably over time (Hofmann et al. 2008).

Another effect of atmosphere layers on the GNSS signal is the ionospheric delay. The ionospheric delay, or, more precisely, the ionospheric group delay on code observations and the ionospheric phase advance on the carrier phase observations, is the refraction of radio signals caused by the presence of electron density in the ionosphere. Total electron content (TEC) is

defined as the integral of electron density in one square meter column on the ionosphere along the ray transition path. The TEC unit is represented as TECU, and one TECU is equal to 1016 electrons/m^2. Since the ionosphere is highly variable in space and time, the electron density can be considered a spatiotemporal random function. In basic PPP models, the ionospheric delay can be removed by multiple-frequency ionospheric-free combinations. Alternatively, the ionospheric day for particular locations at a specific time can be computed from any external models (Antonini 2013).

The effects of the atmospheric layer on GNSS signals are described in more detail in Section 2.2.

2.2. Atmosphere and GNSS signals

2.2.1. Atmospheric Region

The physical characteristics of atmosphere and structure of the electromagnetic spectrum are the main factors in the classification of atmosphere. Since GNSS signals operate in L band frequency, in this study the classification of atmosphere is according to L band frequency signal propagation in the atmosphere. In terms of radio signal propagation, the atmosphere is made up of troposphere and ionosphere layers:

- Troposphere: the lowest atmospheric layer to the Earth's surface with the altitude ranging from zero to approximately 50 km. It is part of the electric neutral layer of the atmosphere and is a non-dispersive medium for signal frequencies below 30 GHz. The atmosphere refraction index in the troposphere varies based on the atmospheric pressure, temperature, and water vapor pressure and can be considered constant with frequency (Antonini 2013).

- Ionosphere: a slightly ionized plasma composed of a free electron and extending from an altitude of 50 km to more than 1000 km from the Earth's surface.

The troposphere contains about 75% of the neutral air mass and 99% of atmospheric water vapor content; therefore, many meteorological phenomena such as clouds, precipitations, and storms are formed in this layer (Antonini 2013). It is worth mentioning that in sporadic cases, water vapor presents in the stratosphere layer with an altitude of 20 and 30 km from the Earth's surface. In general, about 99% of the neutral atmospheric mass and all of the atmospheric water vapor content exist in up to 50 km of the Earth's atmosphere; therefore, troposphere and stratosphere layers are similar in terms of radio signal propagation and are commonly categorized as a single layer in GNSS literature (Antonini 2013). Both the troposphere and the ionosphere

cause refractions in GNSS signals. These refractions cause a delay in the signal travel time and therefore are considered error sources for GNSS observations, as described in more detail in the next section.

2.2.2. Effects of Atmosphere on Radio Signal Delay

Ionospheric Delay

The ionosphere is a layer of the Earth's atmosphere in the altitude of 50 to 1000 km from the Earth's surface. This layer contains ionized particles that lead to a delay or expedition in the satellite signals' travel time. The ionospheric delay on code observations and the ionospheric phase advance on the carrier phase observations are the refraction of radio signals due to the presence of electron density in the ionosphere. Moreover, the direction of radio signal propagation is deviated by the ionospheric refraction of the electromagnetic signals. The ionospheric delay decreases at higher elevations of the satellite receiver direction. The opposite effects of the ionosphere on the code and carrier phase measurements are due to the dispersive characteristic of the ionosphere on the signal velocity. The total electron content (TEC) in the ionosphere is used to determine the magnitude of the ionospheric effects, and it varies from 1 to 100 m or more. Reliable modeling of the ionospheric delay is essential to resolve phase ambiguity in GNSS precise point positioning (Gregorczyk et al. 2017). In basic models of PPP, the ionospheric delay can be removed by multiple-frequency ionospheric-free combinations. Alternatively, the ionospheric day for a specified location at a specific time can be computed from any external model.

Tropospheric Delay

The troposphere is a non-dispersive layer causing refractions in the propagation of GNSS radio signals. Refraction takes place during the transition of the radio signal from one medium to another. The refraction effects on the radio signals include 1) a deviation of the signal propagation

direction from a straight line (bending) and 2) a velocity change, with respect to the signal velocity in the vacuum (slowing). The refraction is generally represented by a refractive index n of a medium as follows:

$$n = \frac{c}{v} \quad (2-5)$$

where c is the speed of light in vacuum and v is the speed of light.

The refractive index is used in the electric field (E) for determination of signal propagation in space and time:

$$E(r,t) = E_0 e^{i[n(r)k.r-wt]} \quad (2-6)$$

where $n(r)$ is the refraction index, E_0 is the amplitude of the electric field, r is the position vector in x, y, and z directions, k is the wave vector ($|k| = \frac{2\pi}{\lambda}$), and $w = 2\pi f$ is the angular frequency.

Refractivity (N) can be determined as follows :

$$N = (n-1) \times 10^6 \quad (2-7)$$

In the lower atmosphere, the spatiotemporal variation of the water vapor is much higher than other components, including gases like nitrogen, oxygen, argon, and carbon dioxide. Moreover, the major part of radio signal refractivity is due to the presence of water vapor. The general form of the refractivity, which is directly dependent on the water vapor content, is as follows (Antonini 2013):

$$N = K_1 \frac{P_d}{T} z_d^{-1} + K_2 \frac{e_w}{T} z_w^{-1} + K_3 \frac{e_w}{T^2} z_w^{-1} \quad (2-8)$$

where

$K_1; K_2; K_3$ are empirical constants; P_d denotes the dry air's partial pressure in [hPa]; T is the temperature [K]; e_w is the water vapor's partial pressure of water vapor [hPa]; z_d^{-1} and z_w^{-1} are the

factors for the inverse of compressibility of dry air and water vapor, respectively; and Z is the

compressibility factor for considering the gas ideal behaviors in the real gas relationship

$$PV = ZRT \quad (2-9)$$

where P, V , R , T and are the pressure, volume, universal gas constant, and temperature,

respectively. The compressibility factor is expressed by

$$z_d^{-1} = 1 + P_d \left[57.91 \times 10^{-8} \left(1 + \frac{0.52}{T} \right) - 9.4611 \times 10^{-4} \left(\frac{T_c}{T^2} \right) \right] \quad (2-10)$$

$$z_w^{-1} = 1 + 1650 \frac{e_w}{T^3} [1 - 0.01317 \, T_c + 1.75 \times 10^{-4} T_c^2 + 1.44 \times 10^{-6} T_c^3] \quad (2-11)$$

where $R = 8.31434 \; kJ \; kmol^{-1} \, K^{-1}$ is the universal gas constant; $M_d = 28.9644 \; kg \; kmol^{-1}$ is

the molar weight of dry air; $M_w = 18.0152 \; kg \; kmol^{-1}$ is the molar weight of water vapor; and

$\frac{M_w}{M_d} = 0.621977$.

The total mass density is given by

$$\rho_T = \rho_d + \rho_w \quad (2-12)$$

Using the above quantities in the refractivity equation, and the new coefficient of K_2', the

refractivity can be expressed by

$$K_2' = K_2 - K_1 \frac{M_w}{M_d} \quad (2-13)$$

$$N = K_1 \rho_T \frac{R}{M_d} + K_2' \frac{e_w}{T} z_w^{-1} + K_3 \frac{e_w}{T^2} z_w^{-1} \quad (2-14)$$

In general, the total refractivity can be expressed by two components: the hydrostatic (dry)

refractivity (N_h) and the wet refractivity (N_w):

$$N_h = K_1 \rho_T \frac{R}{M_d} \quad (2-15)$$

$$N_w = K_2' \frac{e_w}{T} z_w^{-1} + K_3 \frac{e_w}{T^2} z_w^{-1} \qquad (2-16)$$

Because the signal delay is associated with the total refractivity, similar components can be used to represent the signal delay. The two components are called hydrostatic and wet delays, respectively.

The radio signals traveling through troposphere experience a path delay. The amplitude of the path delay in the zenith direction and at the sea level varies between 2.30 m to 2.60 m. For a satellite, at an elevation angle of 3 degrees, the delay can be up to 50 m. The delay is considered to be the neutral atmospheric delay, conventionally referred to as the tropospheric delay (TD) because it is mostly affected by the troposphere (Boehm et al. 2006; Benevides et al. 2015)

$$TD = 10^{-6} \int N ds \qquad (2-17)$$

where N is total refractivity along the propagation path, s. The tropospheric delay can also be decomposed in the hydrostatic (dry) and the wet terms:

$$TD = 10^{-6} \int N_{dry} ds + 10^{-6} \int N_{wet} ds \qquad (2-18)$$

The hydrostatic delay causes 90% of the tropospheric delay. This delay occurs in the dry part of the atmosphere, and its amplitude can reach to about 2 m at zenith direction. On the other hand, the tropospheric wet delay, which is significantly smaller than dry delays, happens in the wet atmosphere, and its range varies from 0 m to 0.40 m. Using a mapping function that is related to the satellite elevation angle, the total tropospheric delay on the slant path of the signal can be mapped onto the zenith direction, yielding the total zenith delay (TZD). The TZD is expressed as the sum of the zenith hydrostatic delay (ZHD), and the zenith wet delay (ZWD); their mathematical representation is

$$TZD = \text{ZHD} \times m_h(elev) + \text{ZWD} \times m_w(elev) \qquad (2-19)$$

where $m_h(elev)$ and $m_w(elev)$ are the hydrostatic and wet mapping functions concerning the satellite elevation angle $elev$. The ZWD depends mostly on the distribution of water vapor content along the signal propagation path. Because of the high variability of the atmospheric water vapor, many studies rely on the relatively accurate ZHD model to calculate the ZWD as shown in (Bevis et al. 1992; Rocken 1993):

$$ZWD = \text{TZD} - ZHD \quad (2-20)$$

The PWV can be computed using ZWD measurements from GNSS signals. Retrieving the PWV from the ZWD requires meteorological parameters such as pressure and temperature. Equation (2-5) represents the relation between the PWV and the ZWD (Bevis et al. 1992; Rocken 1993):

$$\text{PWV} = ZWD \times \Pi \quad (2-20)$$

and conversion factor Π is expressed in (2-16):

$$\Pi^{-1} = 10^{-6} \times \rho \times R_v \left(\frac{(3.739 \pm 0.012)10^5}{T_m} + (22.1 \pm 2.2) \right) \quad (2-21)$$

where ρ is the water vapor density (1000 kg m^{-3}) and R_v denotes the specific gas constant of water vapor (461.5 J $kg^{-1}K^{-1}$). T_m is the modeled weighted mean temperature of the troposphere (K), which is computed based on the regression relation between T_s (surface temperature) and T_m from a linear function, $T_m = 70.2 + 0.72\, T_s$ proposed by (Bevis et al. 1992). Although the ZHD and, therefore, PWV computations involve the meteorological parameters, they are relatively stable in time and space and can be obtained by an interpolation method.

In this study, the abovementioned tropospheric zenith delay is calculated using the JPL's GIPSY-OASIS software. An automatic precise point positioning service (APPS) within GIPSY is implemented to process the GPS phase and code measurement. JPL's Final products, JPL's Rapid

products, or JPL's Real-Time products can be used to determine GPS orbit and clock parameters. APPS uses the most accurate orbit and clock products if they are available. Following IGS standards, APPS automatically applies satellite and receiver antenna phase center variation (APV). The antenna type is used to determine the choice of receiver APV maps. When the antenna type is not recognized, APV is not applied in APPS. The 15-degree elevation angle cutoff is applied in APPS for GPS observation processing.

The following parameters are estimated using GIPSY processing of GNSS observations:

- A random walk function is used to derive the Zenith wet delay with a variance of 3 mm^2 per hour

- A random walk function is used to determine the wet delay gradient with a variance of 0.3 mm^2 per hour

To retrieve the tropospheric delay components, GIPSY applies the GMF troposphere mapping function and a priori hydrostatic delay in meters calculating from eq. 2-17:

$$\text{apriori hydrostatic delay} = 1.013 \times 2.27 \times \exp(-0.000116 \times h) \qquad (2-22)$$

where h is the indication of the station height above the ellipsoid in meters. A priori for the wet delay is 0.1 m. Tropospheric gradients are also estimated in the GIPSY positioning process. The Tropospheric Delay Parameter (TDP) file, containing time series for all estimated parameters with their formal errors, are provided as the GIPSY APPS output. The estimated wet delay parameter provided by GIPSY is used in eq. 2-16 to retrieve the PWV.

2.3. Severe Weather Monitoring and Forecasting Using GNSS Meteorology

Several atmospheric factors contribute to the development and occurrence of extreme precipitation. The moisture and water vapor content, instability, and convergence–divergence conditions are vital factors to take into account to forecast heavy precipitation (Kiely et al. 1998; Dayan et al. 2015; Tian et al. 2015). Recently, there has been great interest in using GNSS in meteorology studies. It is due to the proved effectiveness of GNSS for the atmospheric water vapor content estimation in a higher spatial and temporal resolution compared with the study of the classic instruments such as radiosondes and the water vapor radiometers (Haase et al. 2003; Champollion et al. 2004; Vedel et al. 2004; Jade et al. 2005; Jin et al. 2007; Seco et al. 2012). The GNSS infrastructure, with a good distribution of GNSS reference stations, allows for collecting water vapor data in the atmosphere all over the US (Gradinarsky et al. 2002; Jade et al. 2005; Jin et al. 2007; Seco et al. 2012).

The capability of GNSS-based tropospheric parameters for monitoring and prediction of precipitation has been proven in previous studies (Boniface et al. 2009; Benevides et al. 2015; Sapucci et al. 2016; Chen et al. 2017). Askne and Nordius used a ground-based GNSS network to propose a relationship between ZWD, and GNSS derived PWV to detect atmospheric water vapor (Askne, J. & Nordius 1987; Bevis et al. 1994). A correlation between the GNSS-derived PWV and the measured rainfall is shown by Sapucci et al. (2016). Wang showed that tracking the sudden rises in the GNSS-derived PWV in the long-term data can indicate the rainfall occurrence and, therefore, can be used for rainfall forecasts. Wang utilized the combination of the GNSS-derived PWV and other meteorological parameters in a neural network algorithm to propose a rainfall prediction model with a high success rate for 2 h time intervals (Wang et al. 2010). GNSS-derived PWV is used to illustrate the enhancement of the near real-time prediction of precipitation by Cao

et al. (2016). Shi et al. (2015) verified the feasibility of using the real-time GPS-derived PWV in precipitation prediction by analyzing several rainfall events in Wuhan, China. Real-time GNSS-derived PWVs are used to define an empirical threshold for the forecast. Shoji et al. showed the relationship between the time when PWV exceeds a given threshold and rainfall probability increases (Shoji et al. 2013). By using long-term GNSS-PWV and meteorological data in the northeast of Spain, Seco et al. (2012) proposed a method for short-term rainfall forecast. Utilizing the GNSS-derived PWV, Liu et al. (2006) showed that atmospheric water vapor above 25 mm and an increase in water vapor more than 5 mm can cause an increase in rainfall probability by about 50%. During the increased period of GNSS-derived PWV in the PWV time series, Benevides et al. (2015) used the first derivative of PWV to forecast the rainfall with a success rate of about 75% (Yao et al. 2017). Also, Manandhar et al. (2018) proposed a data-driven algorithm using GNSS-PWV and meteorological parameters, including dew point temperature, relative humidity, and solar irradiance, to forecast rainfall with a success rate of 87.4%. Zhao et al. (2018) verified that the relationship between the PWV increases and decreases before and after the occurrence of rainfall, respectively, and used the PWV fluctuations over time to detect and monitor rainfall events. Yao et al. 2018 also proposed a prediction algorithm by utilizing the GNSS PWV data and achieved a rainfall forecast success rate of approximately 80%. Zhao et al. (2018) verified the feasibility of direct utilization of ZTD and its first derivatives in a rainfall forecast algorithm to overcome the observation error associated with the meteorological data and ZWD to PWV conversion error.

When GNSS-based estimated PWV is analyzed with the local atmospheric elements, the formation process of severe precipitation can be observed by assessing the correlation between atmospheric pressure, temperature, and PWV. For example, the low-pressure system leads to

condensation of water vapor as well as the formation of clouds and precipitation. In addition to the low-pressure system, high humidity and temperature contribute to forming precipitation. Past studies found both negative and positive correlations between precipitation and temperature, depending on seasons and locations (Madden and Williams 1997; Weining et al. 1993). Because the PWV fluctuation is the indication of precipitation showing an interrelation with other atmospheric parameters, the PWV rate of change (ROC) over time can be used to track the atmospheric variations. Several studies have shown that the PWV significantly increases a few hours before the most intense rainfall, then sharply decreases when precipitation begins to weaken and finally ceases (Tahami et al. 2020; Realini et al. 2014; Priego et al. 2017; Tahami et al. 2017; Manandhar et al. 2018). The literature found that 1) PWV peaks occur at a few hours before the precipitation onset and 2) the PWV ROC sharply varies before the start of the rain in the most rainfall events. Thus, the significant spatial-temporal variation of PWV and PWV ROC corresponds to the rain event in time and can be identified as essential features for short-term precipitation forecasting purposes (Tahami et al. 2020; Tahami et al. 2017; Yao et al. 2017; Manandhar et al. 2018). While previous studies have discussed the relationship between PWV and rainfall, extensive studies are yet to be done in the precipitation prediction using GNSS-derived PWV. Therefore, a new method of short-term precipitation forecasting during severe weather phenomena such as a hurricane is proposed here based on GNSS-derived PWV.

CHAPTER 3

3. SPATIAL-TEMPORAL ANALYSIS OF METEROLOGICAL DATA

In this chapter, the spatiotemporal variation of PWV and meteorological data, measured by a GNSS and meteorological sensors respectively, during a severe weather event is analyzed to find the correlation between the GNSS-derived PWV variations and severe precipitation. Statistical characteristics of PWV over time, and temporal variation of meteorological parameters including pressure and temperature during severe weather events, are analyzed to introduce the major components in monitoring and forecasting the severe precipitation onset. This chapter proposes a new method that quantifies the relationship between a spatiotemporal atmospheric event's intensification and GNSS derived PWV and meteorological observations.

3.1. GNSS-based PWV processing

The use of GNSS-derived tropospheric delays to measure and monitor the PWV and its variations has been investigated by numerous researchers (Benevides et al. 2015; Shoji et al. 2015; Bonafoni et al. 2016; Realini et al. 2016). To find the relationship between variations of PWV and other atmospheric parameters in the formation of severe weather phenomena, Hurricane Matthew 2016 was selected, and several GNSS Continuously Operating Reference Stations (CORS) and weather stations were used as an example for the analysis. Figure 3-1 shows an example of GNSS and weather stations located in Hurricane Matthew 2016 (further description of the geographical distribution of GNSS CORS with details in the Hurricane Matthew case study are found in Chapter 5).
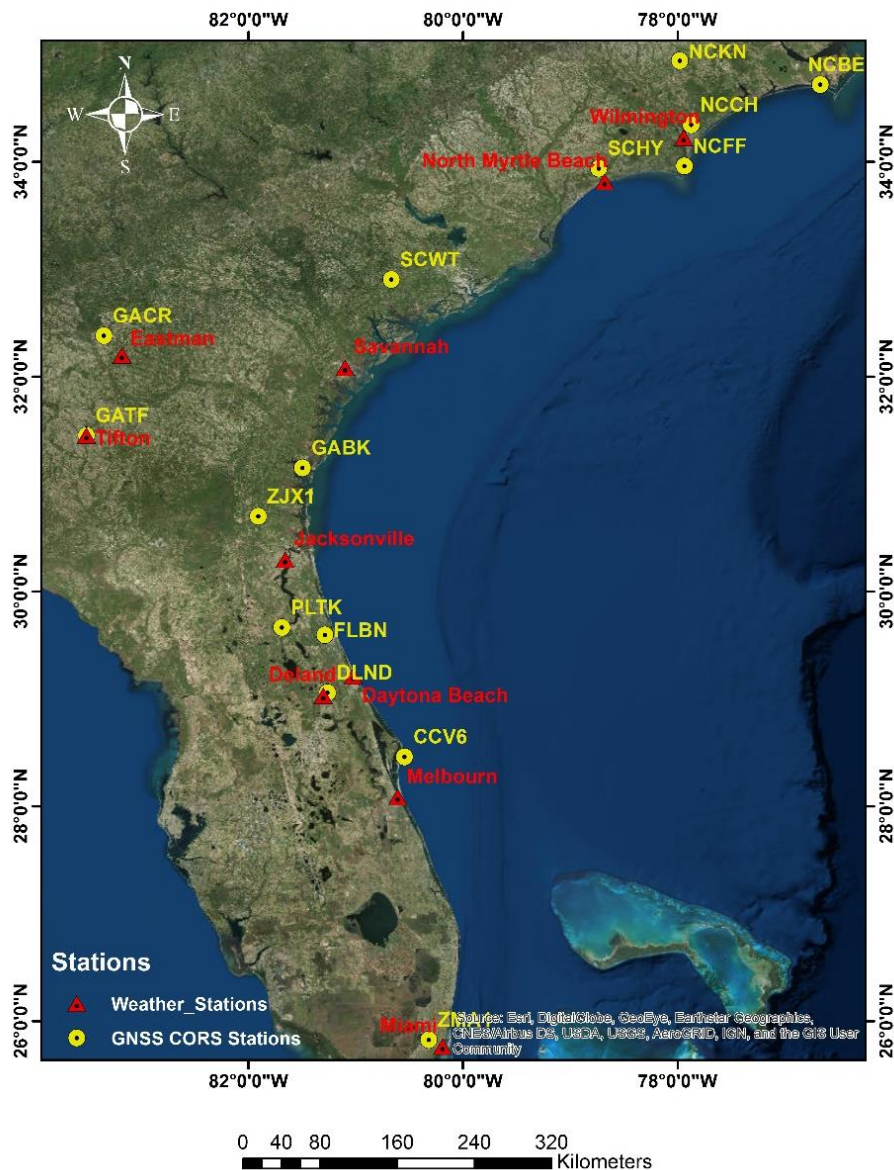
Figure 3-1: Example of distributed GNSS and meteorological stations in Hurricane Matthew 2016 (Base map from ESRI ArcGIS)

As described in Chapter Two on the use of GNSS stations, the GNSS-derived ZTD can be estimated using the automatic precise positioning service (APPS) developed by NASA's Jet Propulsion Laboratory (JPL) (http://apps.gdgps.net). From each ZTD site-dependent value, the ZWD is calculated by subtracting the ZHD from the ZTD, where the former is obtained from the online service at each GNSS site. The ZWD data from the GNSS CORS network are used to

retrieve the PWV above the respective CORS stations as described by Bevis et al. (1992). To provide the PWV for the entire study area rather than the PWV at each GNSS CORS site, the inverse distance weighting (IDW) interpolation method was applied (Yang et al. 2015). Because the water vapor varies with height (Askne et al. 1987), the topography of the study area should be investigated by generating a digital elevation model using GNSS-derived height and geoid height from GEOID12B. In the case study of Hurricane Matthew, the topography of the study area mostly shows insignificant dynamics for the stations located at the coastline area.

The meteorological parameters, such as atmospheric pressure and temperature around the CORS stations, provide superior precision on estimating the tropospheric delay throughout the process (Benevides et al. 2015). Because the surface pressure and temperature measurements are available only at the weather stations in the test area, they should be corrected for the selected CORS stations. In particular, pressure is an important factor in estimating GNSS-derived PWV. Hence, Realini et al. (2014) proposed an approach based on the barometric formula of Berberan-Santos et al. (1997) to adjust the pressure measurements to different heights as shown in eq. (4). This provides sufficiently accurate pressure measurement for each GNSS station.

$$P_{CORS} = P_{MET}.\exp(-\frac{gM_d(H_{MET} - H_{CORS})}{R^* T_{ISA}}) \quad (3-1)$$

where g is the gravitational acceleration constant (9.80665 m s-2), M_d is the molar mass of dry air (0.0289644 kg mol−1), R^* is the gas constant for air (8.31432 J mol-1 K-1), and T_{ISA} is the international standard temperature of the atmosphere at sea level (288.15 K). H_{MET} and H_{CORS} are the orthometric heights of meteorological and CORS stations, respectively. The orthometric height of each CORS station is provided through Online Positioning User Service processing in NAVD88 computed using GEOID12B provided by the National Geodetic Survey.

To compute the orthometric height for all stations in the test area, the IDW interpolation technique is performed. Figure 3-3 shows the computed pressure (P_{CORS}) time series for some of the CORS stations as a dashed line, while the weather station measurements are represented by circles on the graph. The height-corrected pressure data for CORS stations with the meteorological pressure data are used to calculate meteorological-based ZWD delay in the following sections. Because the height variations over the coastal area are small, the height corrections for the CORS stations located near the coast are insignificant. Figure 3-2 shows the corrected pressure for the CORS stations and observed pressure at their corresponding meteorological stations.
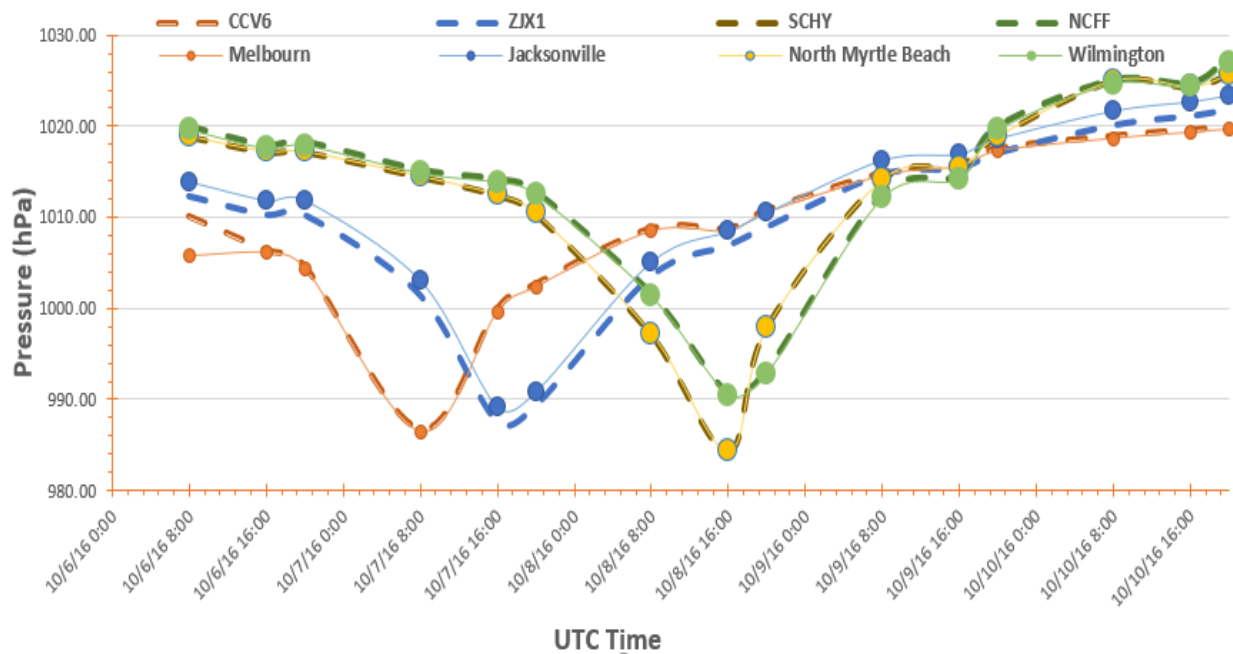
Figure 3-2: Comparison of the observed pressure data with the corrected pressure for the height differences of sample CORS stations: Dash lines represent the corrected pressure at CORS stations, and continuous lines display the observed pressure at the meteorological stations

3.2. Variations in meteorological parameters during severe weather

In addition, the meteorological measurements are interpolated using the IDW technique over the study area by taking into account the height differences between the metrological stations and their nearby CORS stations as described earlier. Figures 3-3 and 3-4 show a sample realization of interpolation for the pressure and temperature, respectively.
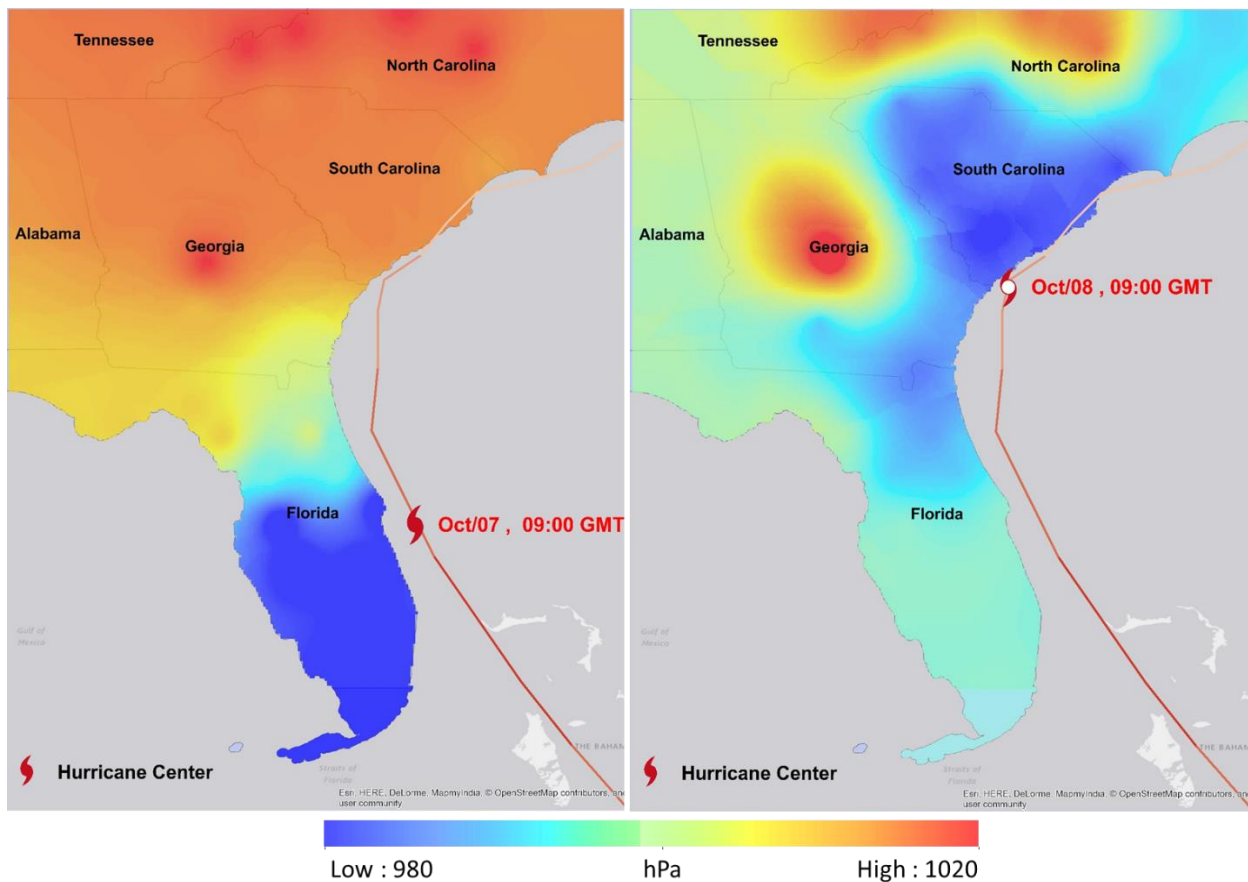
Figure 3-3: Example of pressure fluctuations over the study area on selected time epoch during Hurricane Matthew, which hit October 7, 2016 at 9 a.m. GMT (left) and 24h later on October 8, 2016 at 9 a.m. GMT (right). The red hurricane symbols represent the center of hurricane and time of the hurricane hit as reported by the National Hurricane Center (NHC)

By analyzing the interpolated pressure data, the movement of the low-pressure system from Florida toward South Carolina is identified. The low-pressure system in the area causes air to converge, leading to condensation of water vapor and formation of the clouds and, consequently, precipitation. As an example, the left plot in Figure 3-3 shows the low-pressure center over the study area at Florida on October 7, 9 a.m. GMT, while 24h later on October 8, 9 a.m. GMT, the low pressure system left Florida and arrived in South Carolina. The displayed areas under the influence of low-pressure centers can expect generally cloudy conditions with precipitation.
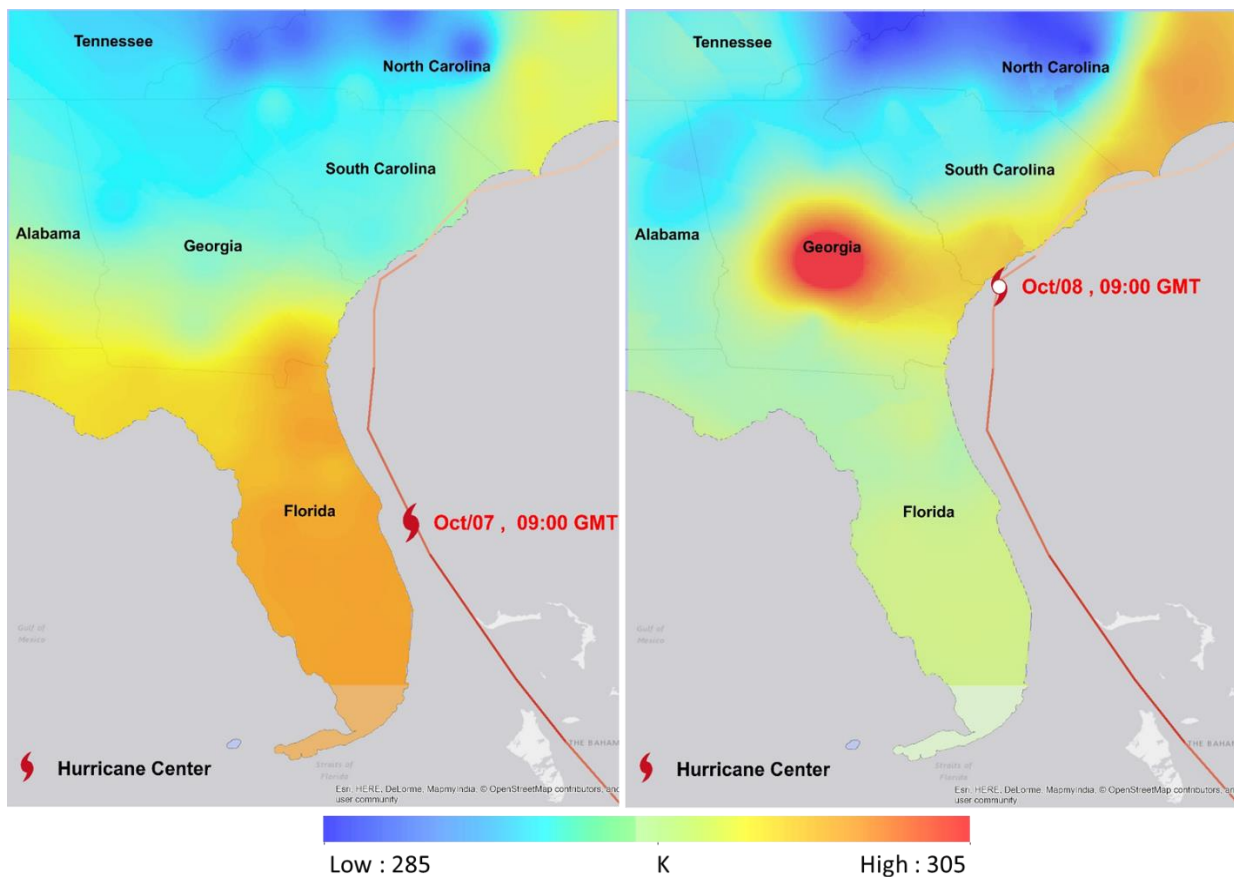
Figure 3-4: Example of temperature fluctuations over the study area on selected time epochs during Hurricane Matthew, which hit October 7, 2016 at 9 a.m. GMT (left) and 24h later on October 8, 2016 at 9 a.m. GMT (right). The red hurricane symbols represent the centers of the hurricane as reported by NHC

In addition to pressure, temperature plays an important role in the formation of precipitation. In high humidity and low temperature, the air pushes together, squeezes out water, and derives precipitation. Therefore, precipitation and temperature are negatively correlated, which indicates that the colder area does not tend to be dry and is likely affected by rain. The right plot in Figure 3-4 illustrates the low temperature on October 7 in Florida that is correlated to the low-pressure center at the same influenced area. Because the elevation differences in the study area are reflected in the GNSS-derived PWV values, the dependency of PWV with respect to the station altitude is investigated and demonstrated in Figure 3-5. As an example, the estimated PWV values in the five-day period from October 6–10 have been plotted with respect to the station's orthometric heights. A visible decrease of PWV by increasing the altitude has been shown in the plot. In addition, owing to the extremely reduced atmospheric pressure and increased temperature range on October 7 (see Figures 3-3 and 3-4), the PWV on October 7 became larger than all other dates at all altitudes. A significant decrease in PWV with increasing altitude is also seen.
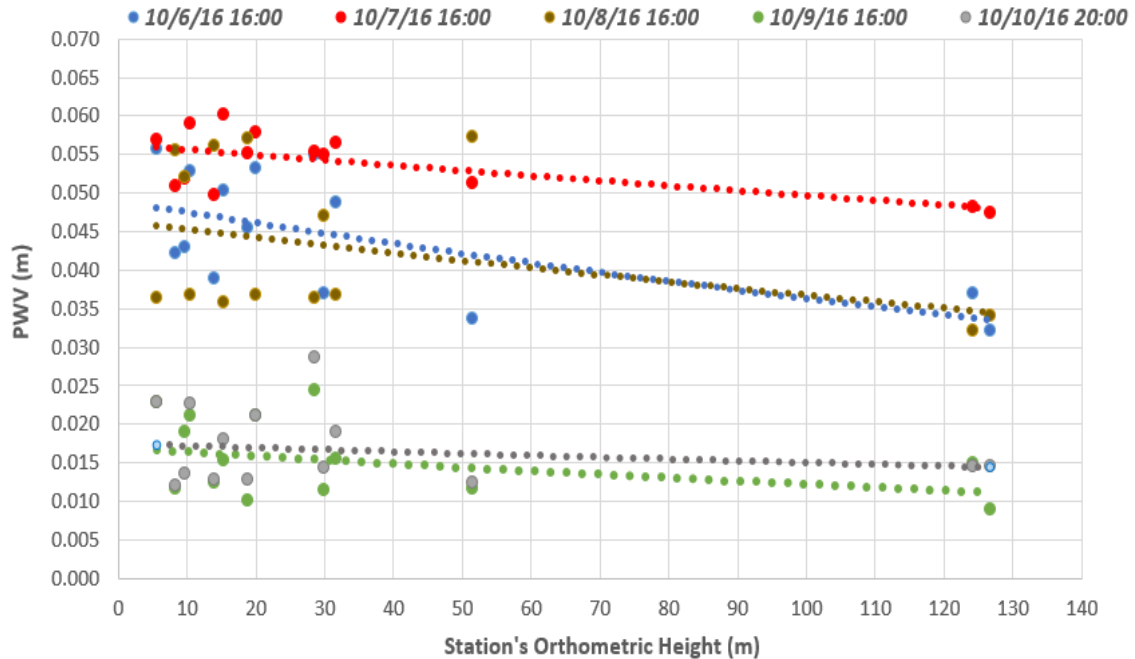
Figure 3-5: PWV changes with respect to CORS station's height

Taking the exponential relationship between the scale height and PWV, Parker et al. (2009) suggested normalizing the PWV based on the heights of a reference station and target stations. However, the altitude effect can be ignored (like in this study) if less variation in the elevation of the study area is observed. Figure 3-6 shows the example of the spatial distribution of PWV interpolated from GNSS-derived PWV by the IDW interpolation method. It can be seen that the highest values were recorded in the area of Florida and South Carolina during the 24h period from October 7, 2016 at 9 a.m. GMT to October 8, 2016 at 9 a.m. GMT.
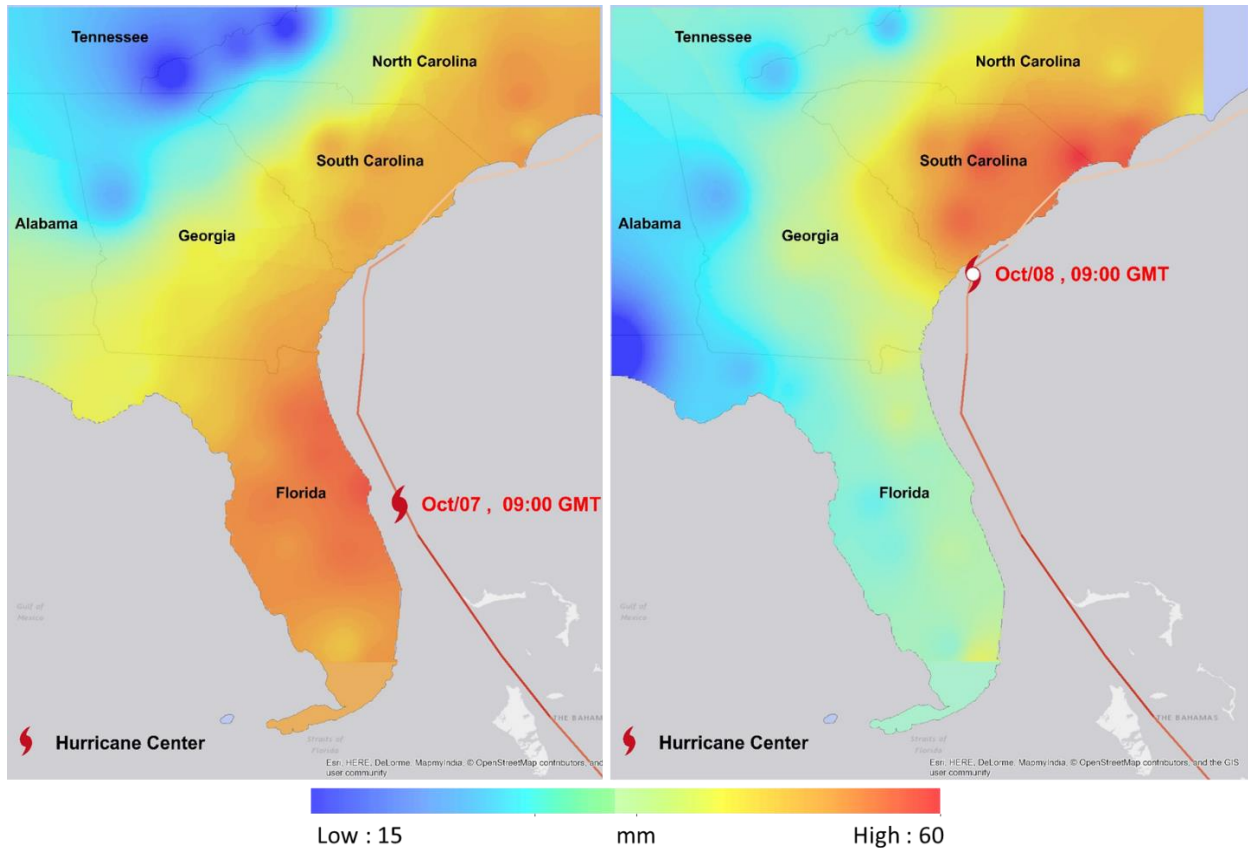
Figure 3-6: PWV variations over the study area on selected time epochs during the Hurricane Matthew, which hit October 7, 2016 at 9 a.m. GMT (left) and 24h later on October 8, 2016 at 9 a.m. GMT (right). The red hurricane symbols represent the location and time of the hurricane center as reported by NHC

As Figure 3-6 shows, the maximum PWV in the area coincides with the area influenced by the low-pressure system and high temperature as shown in Figures 3-3 and 3-4. This confirms the correlation between GNSS-derived PWV and meteorological parameters as pressure and temperature.

3.3. Spatiotemporal variations of GNSS-based PWV during severe weather

To monitor the hurricane movement in the area, the analysis of GNSS-derived PWV over the area during the hurricane is performed. First, the GNSS-derived ZTD variations over time are presented in Figure 3-7. In all stations influenced by the hurricane, a sharp descent followed by an ascending trend in ZTD is identified. The PWV fluctuations time series are also presented in Figure 3-8 referring to Florida GNSS stations including CCV6, DLND, FLBN, and ZJX1 located from the south to northeast part of Florida. The movement pattern of the PWV fluctuations at Florida stations indicates the possible occurrence of the northeast movement of the water vapor that corresponds to the hurricane movement from the south toward the northeast region. The increase of the PWV started from CCV6 around 59 mm and rapidly reached the maximum value of 61 mm corresponding to a period around 4 hours of increment. A similar increase can be seen in other Florida stations with a few hours offset. The monitoring results validated by the reported time and locations of the hurricane-affected areas clearly indicate a general upward trend of PWV just before the reported hurricane time at all stations regardless of the different level of PWV variation at each station. For all stations, the water vapor variation reached the highest level before the time of each event and then dramatically decreased during and after the event. The spatial distribution of PWV along the east coast shows that the highest values were on October 7–8 at Florida stations and on October 8–9 in South Carolina, which was well matched with the reported hurricane occurrence time. The highest values were recorded in the area of Florida (PWV of 0.059 m) and South Carolina (PWV of 0.061 m).
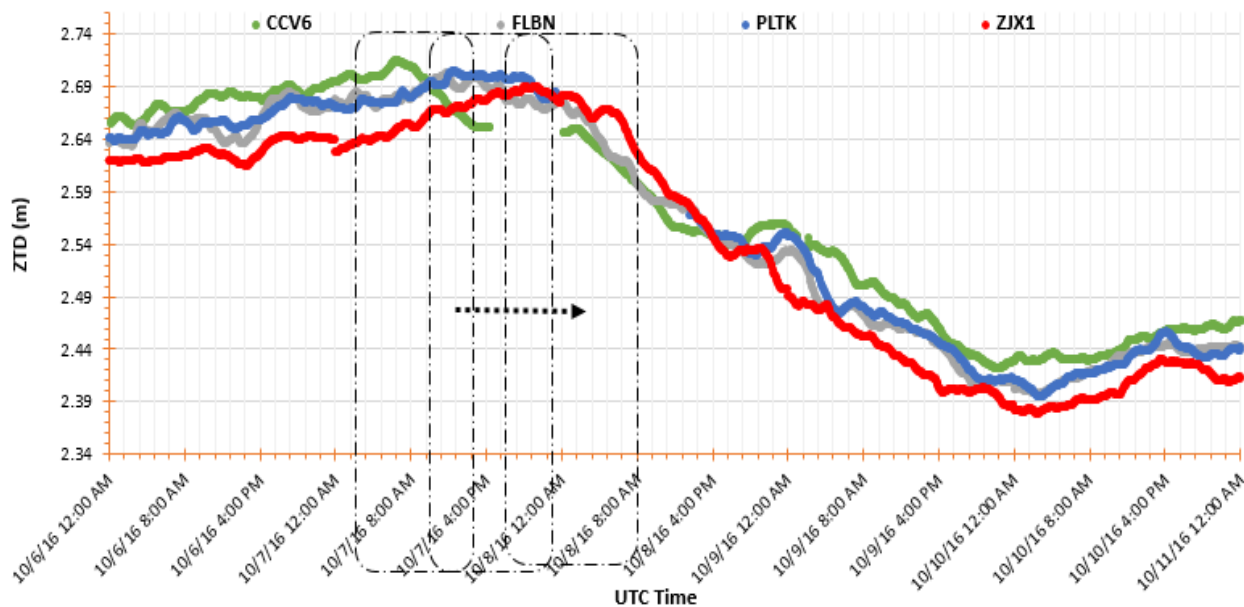
Figure 3-7: ZTD changes over Florida stations during Hurricane Matthew. A similar pattern of PWV fluctuation is observed at the more southern part of Florida (CCV6) toward the more northern part (ZJX1)

Similar behaviors were observed with the gradual increase of PWV to around 0.061 m at GABK on October 7 (4–11 p.m.), which reached the maximum value of 0.063 m on October 8 (10 a.m. –1 p.m.) for SCHY. Because the rain occurred a few hours after a significant PWV peak in the time series of PWV variations, the hurricane effects were estimated at the stations in Georgia and South Carolina in the morning and night of October 8, respectively.
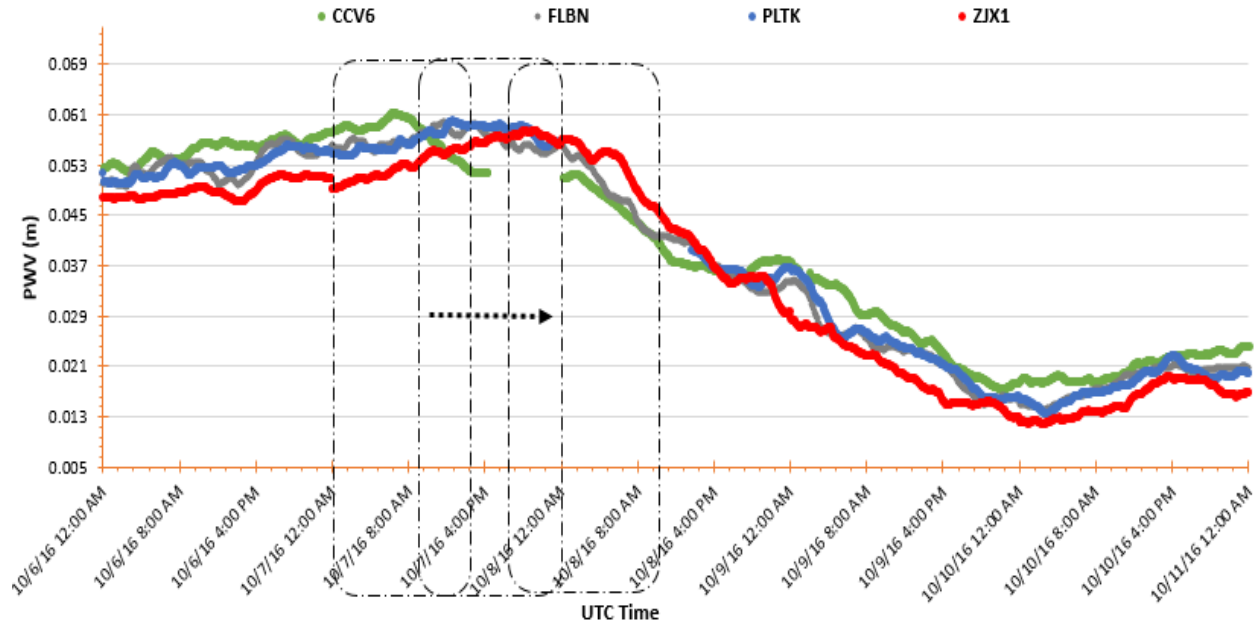
Figure 3-8: GNSS-derived PWV changes over Florida stations during Hurricane Matthew.
A similar pattern of PWV fluctuation is observed at the more southern part of Florida
(CCV6) toward the more northern part (ZJX1)

Figure 3-9 shows the pattern of time series of six CORS stations that cover the entire study area. It shows that the peak occurred first at GABK in Georgia and later at SCHY in South Carolina, indicating the movement of the atmospheric water vapor from the south to the northeast. By considering the peak of PWV time series for GABK and SCHY, one can see that the estimated PWV at SCHY is larger, indicating that the intensity of the hurricane is more significant in South Carolina. The presented discontinuities at some epochs in the graphs show the nonavailability of GNSS data for the corresponding epochs.
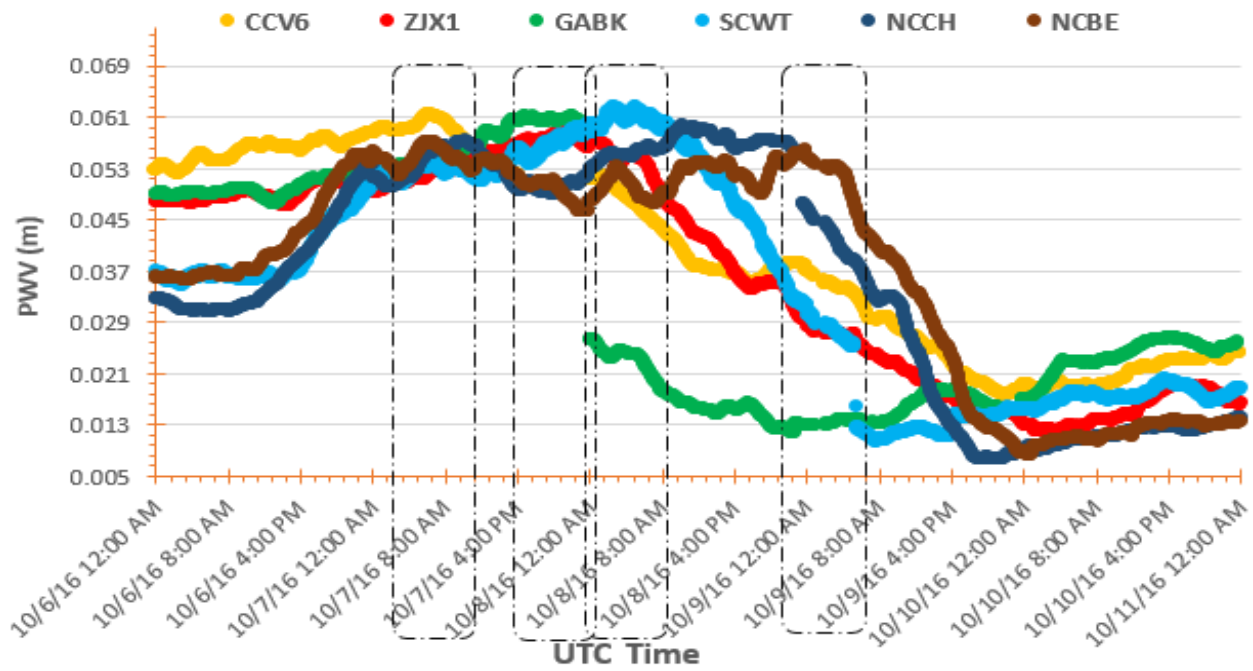
Figure 3-9: PWV fluctuations at five CORS stations located in Florida (CCV6 & ZJX1), Georgia (GABK), South Carolina (SCWT), and North Carolina (NCCH & NCBE) during Hurricane Matthew 2016

3.4. Meteorological patterns and GNSS-based PWV variations

By utilizing the meteorological data during the severe weather, the simultaneous behaviors of PWV and other atmospheric parameters can be identified. Figure 3-10 shows that while the PWV increases (presented in blue bars), the pressure decreases (presented in a black line). In addition, humidity can be considered as another indicator of atmospheric phenomena. During the event of October 6–10, there was a significant decrease of maximum 8 K in temperature and 25 hPa in pressure for all stations in Florida and North Carolina (Figures 3-10 and 3-11). Furthermore, the prominent changes in pressure found during the reported hurricane period, as shown in Figure 3-10, show that a distinct decrease in pressure was observed to occur around 12 hours prior to the precipitation (Figures 3-10 and 3-11). The PWV was greatly increased a few hours prior to the most intense rainfall, and then a sharp decrease was observed a certain time after the heavy rainfall, as also shown by other studies (Priego et al. 2016).
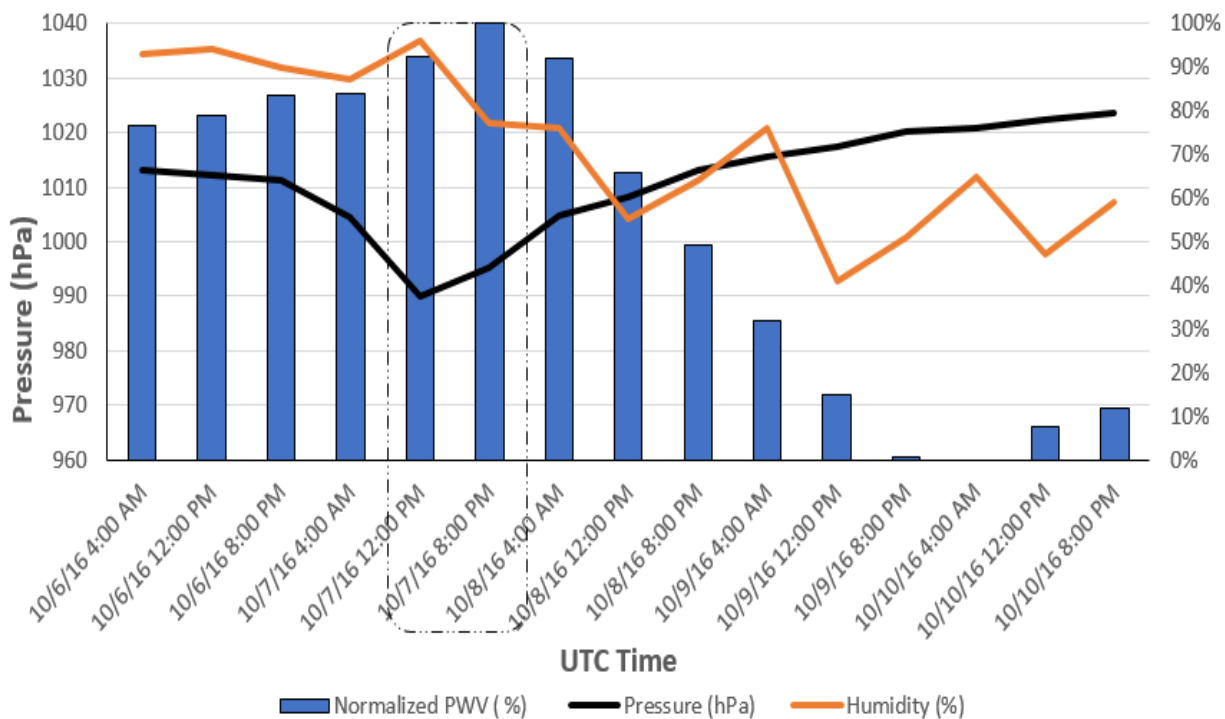
Figure 3-10: PWV, pressure, and humidity fluctuations at ZJX1 in Florida. The dashed box indicates the significant change of the meteorological parameters prior to the most intense precipitation at ZJX1

The sharp decrease in pressure (around 20 hPa), increase in humidity (reaching up to 100%), and the increasing trend of the PWV over the ZJX1 occurred prior to the severe rainfall. It can be seen that the maximum PWV at ZJX1 happened at 8 p.m. on October 7, which is well matched with the interpreted meteorological data. Figure 3-11 presents a similar trend in one of the North Carolina stations, NCFF, from 12 p.m. on October 8. By considering the intense rain in a few hours after the obvious trend in the pressure, humidity, and PWV, the intense rainfall must have occurred after 12 p.m. on October 8. It also coincides with the interpreted meteorological

data, which indicates that the North Carolina region was affected by the severe rainfall from 4 a.m. on October 9.
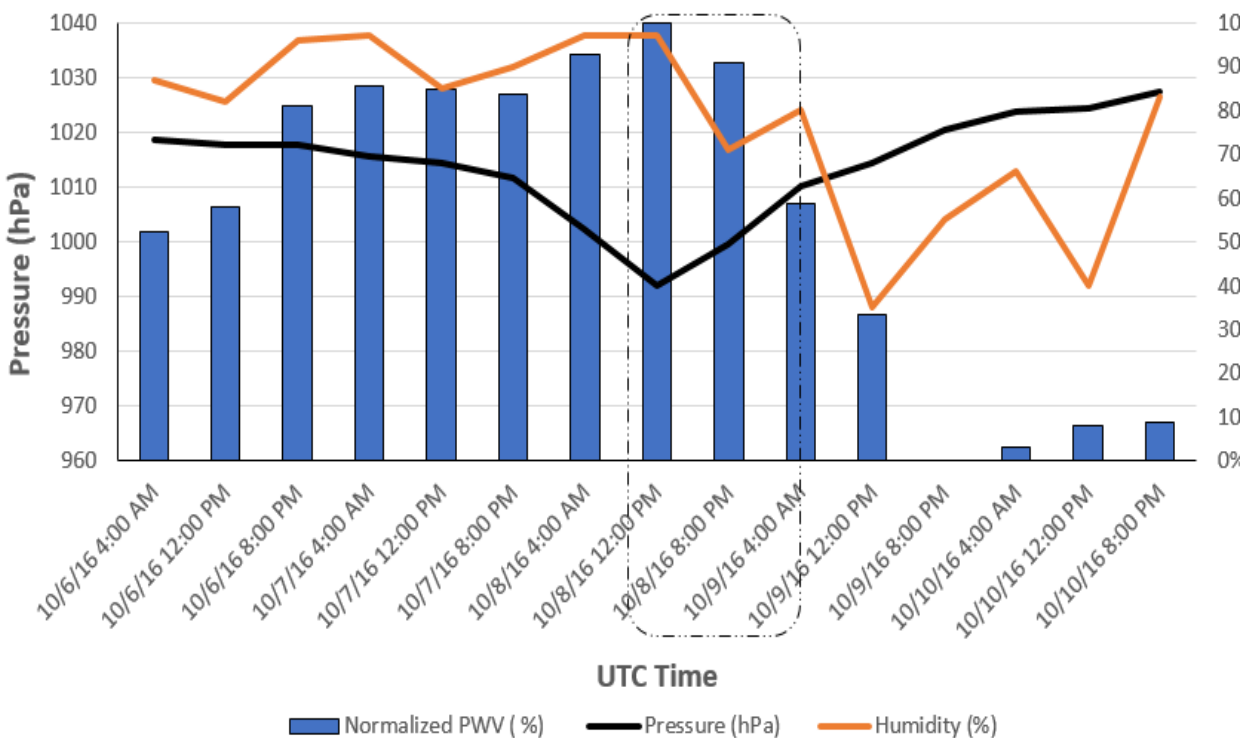
Figure 3-11: PWV, pressure, and humidity fluctuations at NCFF in North Carolina. The dashed box indicates the significant change of the meteorological parameters prior to the most intense precipitation at NCFF

By tracking the trace of a hurricane, it can be further extended to predict the path of the hurricane from the behavior of the PWV ROC (PROC), which is considered a significant indicator for the intensity and duration of the event. For this approach, the PROC in a one-hour interval was computed for two stations, ZJX1 and NCFF in Florida and North Carolina, respectively. At ZJX1 in Florida, the maximum PROC was observed between 9 and 10 p.m. on October 8 (Figure 3-12). By observing the PROC for this event, the threshold of the PROC is empirically set up as 0.030 m/h for the hurricane indicated with the red dashed line, and the associated time windows are marked in black dashed boxes in Figure 3-12 that match up to the actual hurricane event. Based on the definition for the level of hurricane intensity at each station, different thresholds may be applied to classify the intensity. By defining the threshold, the full time series of PROC was analyzed to locate all hours when that threshold was exceeded to indicate a hurricane. The determination of the threshold must be further investigated by considering the other meteorological parameters and the site characteristics, which will be the future work.
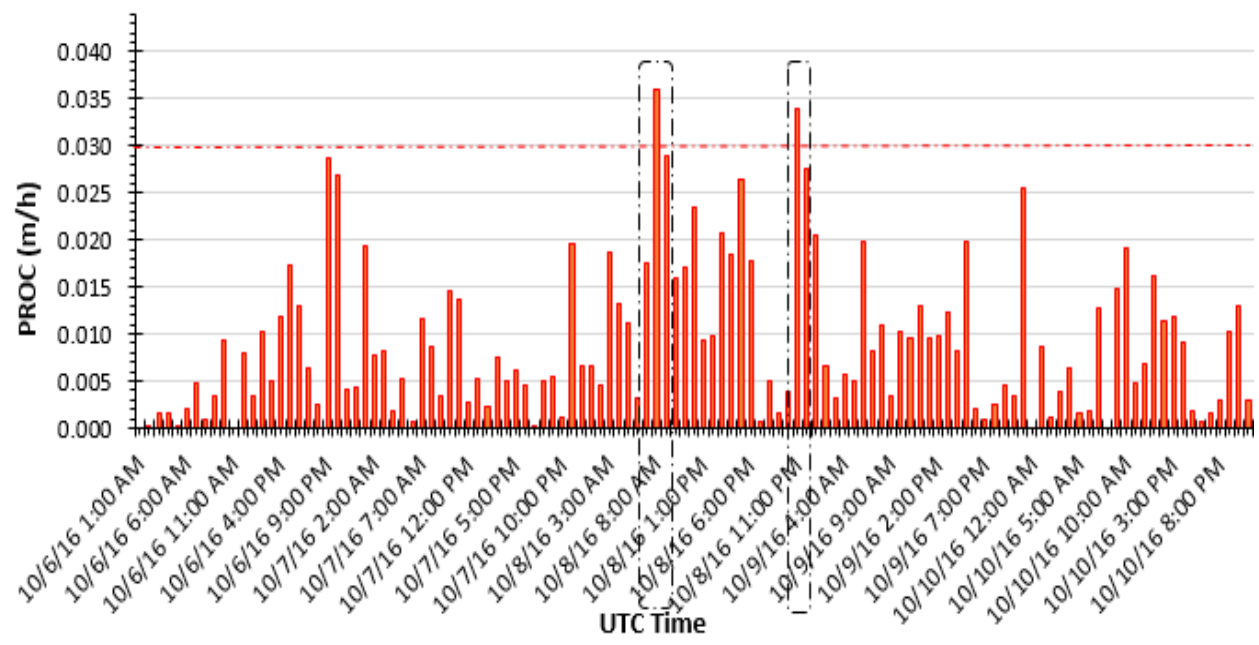
Figure 3-12: PROC at ZJX1 in Florida during Hurricane Matthew's lifetime

Figure 3-12 shows two time windows that match the highest PROC analyzing the time and intensity of the hurricane observed at ZJX1. It seems the most intense parts of the hurricane in the area occurred on October 8, when the PROC was 0.036 m/h. The represented intensive parts of the hurricane are generally associated with the severe precipitation's time suggested by Figure 3-12, indicating the probability of the most intensive precipitation on October 8 for the northern part of Florida.
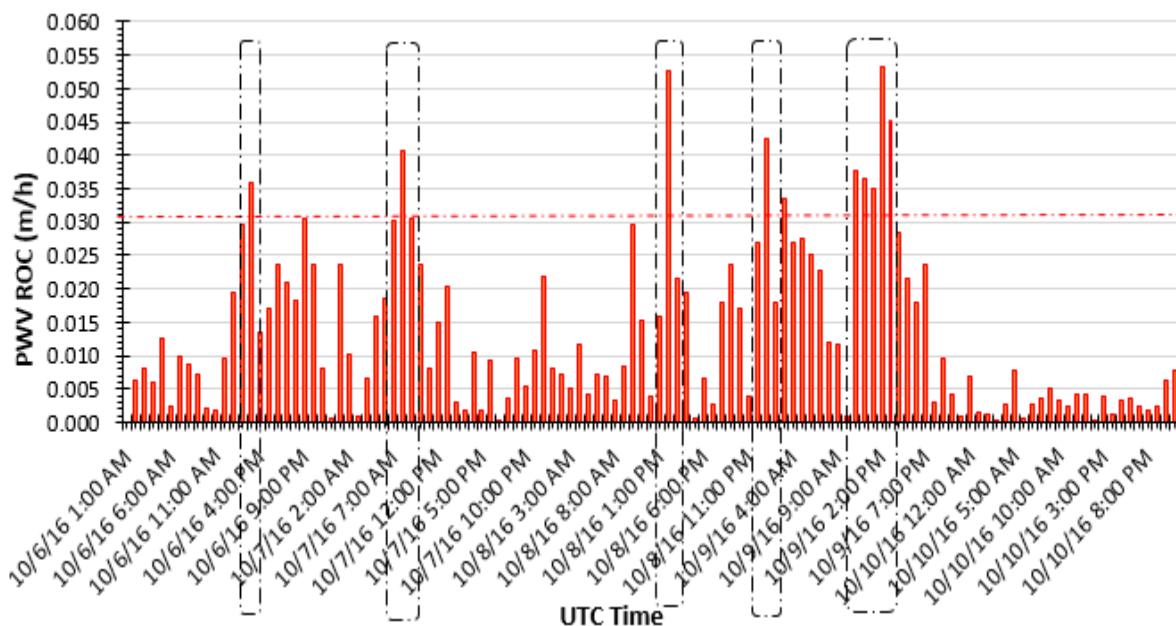
Figure 3- 13: PROC at NCFF in North Carolina during Hurricane Matthew's lifetime

From Figure 3-13, the relation between the maximum PROC and the rain intensity at NCFF can be observed. Figures 3-9 and 3-13 indicate a clear positive correlation between the occurrence time of the maximum PROC and the maximum probability of precipitations. The corresponding time for both the maximum PROC occurrence and the intensive rain is about 2 p.m. on October 8 and 4 a.m.–2 p.m. on October 9, respectively. The greater magnitude of maximum PROC at NCFF (0.053 m/h) in comparison to the corresponding value at ZJX1 (0.036 m/h) is further evidence of

more intense precipitation occurring over North Carolina than Florida. Therefore, by defining the appropriate thresholds based on amplitude of the maximum PROC, this approach can be used to further prediction of time, path, and intensity of the hurricane.

Moreover, the variation of the hurricane intensity and the prediction of its path were monitored based on the dynamical-statistical model using high spatiotemporal resolution GNSS observations. The dynamical-statistical model, which can be considered as a statistical prediction model, quantifies the relationship among a spatiotemporal hurricane intensification, the PROC, and meteorological variables. As discussed earlier, the low-pressure system, where it increases in humidity along with the decreased temperature, is a valuable factor for predicting the time and intensity of the severe rainfall. Based on the aforementioned relationships among the hurricane intensification, the PROC, and the meteorological parameters, a multivariate regression model is proposed to predict the PWV over different locations and times.

CHAPTER 4

4. STATISTICAL MODELING OF PWV DURING HURRICANES

In this chapter a novel short-term forecasting method is proposed to forecast the path of precipitation phenomena by retrieving precipitable water vapor in the troposphere from GNSS data and surface meteorological measures.

4.1. Overview of statistical models for monitoring and predicting hurricanes

Spatial variations of PWV show the transition pattern of water vapor content in the area affected by the hurricane. When PWV are analyzed with the local atmospheric elements, the formation process of a severe precipitation can be observed by assessing the correlation among atmospheric pressure, temperature, and PWV. A low-pressure system leads to the condensation of water vapor as well as formation of cloud and precipitation. In addition to the low-pressure system, high humidity and temperature contribute to forming the precipitation (Weining et al. 1993; Madden and Williams 1997). Because the PWV variation acts as an indication of the precipitation showing the interrelation with other atmospheric parameters, the PWV rate of change (ROC) can be used to observe the atmospheric variation over time. Studies have shown that the PWV greatly increases a few hours prior to intense rainfalls, then sharply decreases when precipitation begins to weaken and finally ceases (Realini et al. 2014; Priego et al. 2017; Tahami et al. 2017; Manandhar et al. 2018). The researchers found that 1) PWV peaks occur a few hours before the precipitation onset and 2) the PWV ROC sharply changes before the start of the rain in most rainfall events. Thus, the significant spatiotemporal variations of PWV and PWV ROC correspond to a rain event and can be identified as important features for short-term precipitation forecasting purposes

(Tahami et al. 2017; Yao et al. 2017; Manandhar et al. 2018). To improve the capability of forecasting the path of severe weather events, a statistical model using PWV derived from GNSS measurements and meteorological data is proposed (Tahami et al. 2020). As the primary input data, the PWV observations are obtained from GNSS data as shown in eq. 2-5. The prediction of PWV is derived from the PWV ROC and meteorological parameters. In eq. 3-1, the PWV at epoch t+1 is estimated by computing the derivatives of PWV, temperature (T), pressure (P), and relative humidity (RH) at epoch t. The derivative of those parameters is calculated by subtracting the weighted mean of measurements in a time window (e.g., $\overline{PWV_t}$)—here, a one-hour window is used—for each parameter from the corresponding parameter at epoch t. The derivative of PWV at t is expressed as ΔPWV_t that is referred to as PWV derivative. Owing to the nature of the meteorological parameters that are related to each other, the multivariate linear regression model is applied. In the proposed multivariate linear regression model, the PWV derivative as a dependent variable is described with respect to the independent explanatory variables of pressure, temperature, and relative humidity. Eq. 3-1 can be simplified to eq. 3-2, where the next value of dependent output (ΔPWV_{t+1}) is regressed on the basis of the previous values of the input regressor ($\Delta PWV_t, \Delta P_t, \Delta T_t, \Delta RH_t$):

$$(PWV_{t+1}) = \overline{PWV_t} + c_1(PWV_t - \overline{PWV_t}) + c_1(P_t - \overline{P_t}) + c_3(T_t - \overline{T_t}) + c_4(RH_t - \overline{RH_t})$$
$$+ e \qquad (4-1)$$

$$(\Delta PWV_{t+1}) = c_i[\Delta PWV_t, \Delta P_t, \Delta T_t, \Delta RH_t] + e \qquad (4-2)$$

where ΔPWV is PWV derivative, P is pressure, T is temperature, RH is relative humidity, c consists of regression coefficients, t is time, and e is the error term. For each prediction time window, the model estimates the prediction of PWV using the hourly PWV ROC and the

derivatives of P, T, and RH. In this study, a model with 12h and 24h lead time is presented to forecast PWV that is applied to predict the hurricane path for 12h and 24h forecasts. Figure 4-1 shows the workflow.
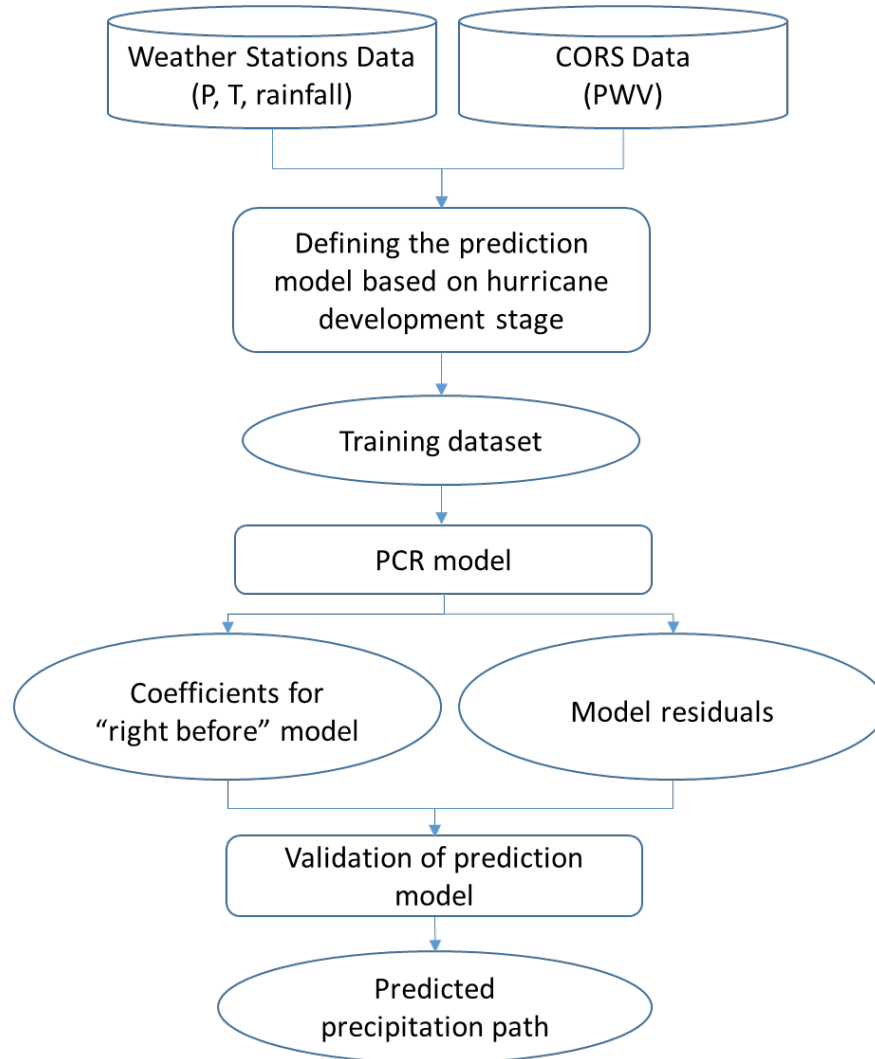
Figure 4-1: Flowchart describing the phases in prediction of severe precipitation path during a hurricane

The process starts with analyzing the fluctuation of metrological data, including the pressure and rainfall, and GNSS-derived PWV to define the hurricane development stages. The PWV variations during the hurricane development stage are then used to classify the prediction

models, which will be explained in section 4.2. For each class of hurricane development, a principal component regression (PCR) model is applied to decorrelate the model parameters in a multiple linear regression analysis for PWV prediction. The detail will be explained in Section 4.3. It should be noted that the CORSs are classified to training and test datasets to be applied in the development and testing of the prediction model. The coefficient of the prediction models is then derived using PCR and the training dataset; more explanation will be given in section 4.4. The PCR is then applied to test the dataset, and the model's residuals are calculated to verify the model. Further explanations will be provided in section 4.5. The model's residuals are then used to track the hurricane path, which will be discussed in more detail in Chapter 5.

4.2. Classification of prediction models based on hurricane development stage

During a hurricane, the PWV in the affected region fluctuates with varying intensity depending on different development stages. The rapid fluctuation of PWV is highly correlated to the severe rainfall and can be modeled in the dynamic statistical multivariate regression model. However, the PWV ROC and other atmospheric parameters behave differently at the different stages of the hurricane, so that the principal regression model introduced in this section should be tailored to each stage in the lifetime of hurricane. Therefore, the time series of PWV observations during a hurricane are divided into multiple classes of *before*, *right before*, *during*, *right after*, and *after* the presence of a hurricane at a PWV observing site—here, CORS—and a unique regression model is developed for each class. To characterize each model, the meteorological parameters and the PWVs from CORSs in the test site are analyzed. In the experiment, a pattern of sudden and sharp increments in the PWV a few hours prior to the onset of precipitation, followed by a sharp descending trend, was observed. Moreover, a correlation between the peaks of PWV and of a hurricane intensity was found. The analysis results show consistent patterns in those meteorological parameters in all sites for each model (Tahami et al. 2017). The results provide evidence that the level of PWV fluctuations can be precisely matched to the meteorological and geographic conditions. This clearly indicates a negative correlation between the pressure and the PWV peaks associated with the intense precipitation in the study area. From the findings, the PWV threshold is set to a range of 0.50–0.055 m, where most of the severe precipitation events occurred when PWV exceeded that threshold. The selection of this threshold is also supported by other studies conducted in different regions and different times whose authors claim that the highest amount of water vapor is observed typically a few hours before the heavy precipitation when the PWV exceeded that threshold (Tahami et al. 2017; Yao et al. 2017; Manandhar et al. 2018). From

the findings of previous studies, the numerical criteria of the classes for this event were determined. Each class is defined by applying the threshold to the GNSS-derived PWV fluctuations. Figure 4-2 is an example (CCV6 station in Hurricane Matthew) showing the PWV, pressure, and rainfall with respect to the aforementioned classes of hurricane stage—*before*, *right before*, *during*, *right after*, and *after*—based on the hurricane occurrence time.
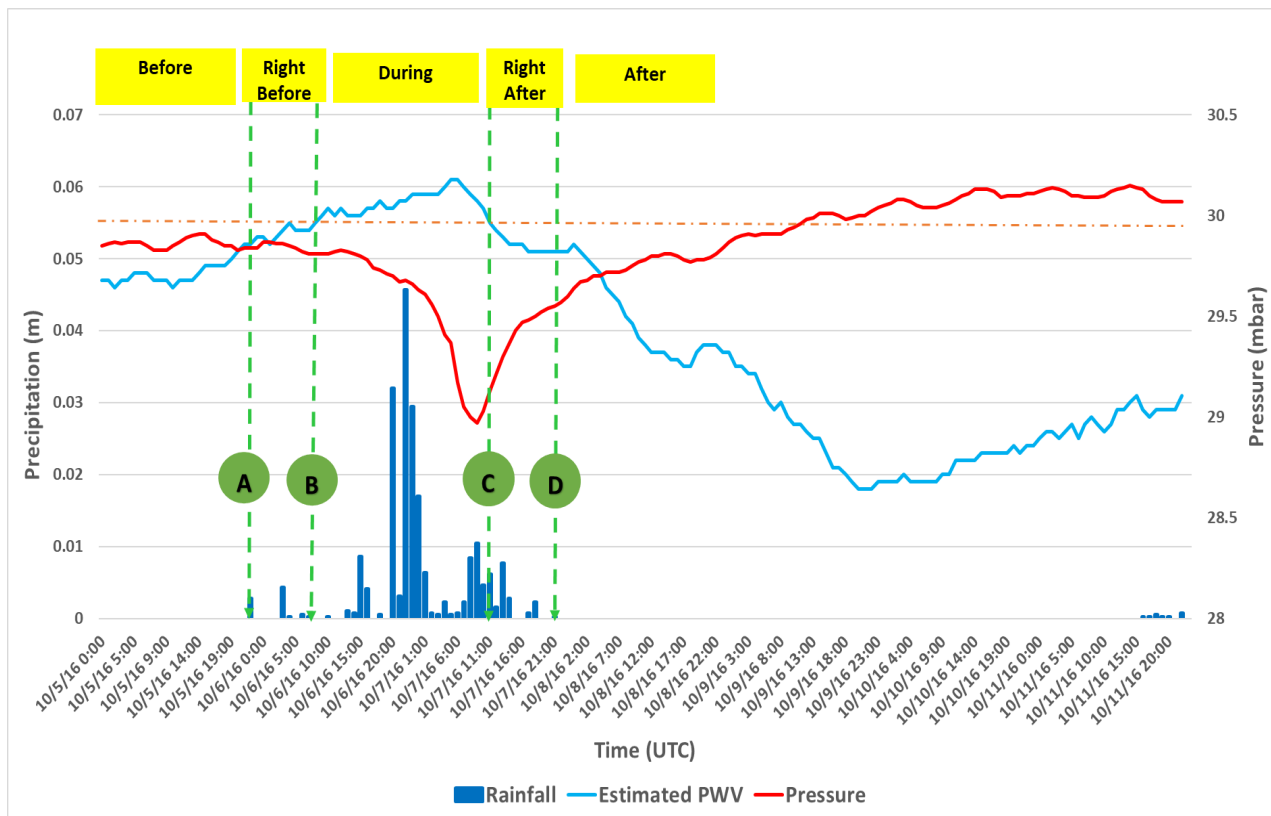
Figure 4-2: Classification of model based on PWV threshold

As seen in Figure 4-2, the GNSS-derived PWV stayed below 0.055m during the *before* class, which is a normal condition, and no severe rainfall was observed during that time. The estimated PWV continuously increased and reached the threshold in the *right before* class when an increase in PWV and decrease in pressure were observed (green symbol indicated as A in Figure

3-2). Therefore, the first epoch of the *right before* class coincides with the beginning of the rainfall. The PWV time series show an active, increasing pattern in the *right before* class. The last epoch of the *right before* class is the time when PWV exceed the threshold (green symbol indicated as B in Figure 4-2). It is the time when the first epoch of the *during* class is also defined. In the *during* class, the rainfall amounts reach their peak. Then the PWV time series dramatically decreases to reach the threshold where the *right after* class is defined (green symbol indicated as C in Figure 4-2). It then decreases to below the threshold, while the *after* class is formed where rainfall begins to cease (green symbol indicated as D in Figure 4-2). It is evident that for this event, all severe precipitations happen when the PWV is fluctuating above 0.055 m. The same strategy is applied to the PWV time series of other stations to define the classes. After defining the classes, a unique regression model can be applied for each class to predict PWV in different prediction time windows to determine the rainfall occurrence during each class. To characterize the model, the training dataset for all the classes, which serve a priori information, are analyzed, and then the models are generalized for detecting the path of hurricane precipitation. The initial condition of forming the hurricane, reflected in the meteorological parameters in the *right before* class for six stations, is used to characterize the model. These stations are typically near the coast, where the onset of a hurricane usually happens. It should be emphasized that this study is specifically focused on the *right before* model, which is the most useful model to analyze the movement of a hurricane. To derive the coefficients, c_i, of each model in eq. 4-2, the representative stations are selected to generate the training datasets of the corresponding model. To derive the coefficient of the *right before* model at the specific time in the study area, six stations, including MTNT, OKCB, ZJX1, GAAU, SCRS, and NCKN, are selected. All of the selected stations in the *right before* model training dataset should reach the threshold in the *right before*

class at the start point of the forecast period. The meteorological and GNSS-derived PWV measurements at a few stations near a hurricane landfall in the area (typically near the coast) are required to serve as the initial information and set the prediction model that makes this method valid for real-world application. This approach is validated by applying the model to other remaining CORSs in the study area as the independent test dataset.

4.3. Principle component regression

A regression model requires a preliminary analysis for identifying the relationships between independent variables and dependent variables to find the multicollinearity problem (Shirzadi Babakan et al.2015; Shirzadi Babakan et al. 2016; Tahami et al. 2016; Tahami et al.2019). The multicollinearity problem occurs as a result of the presence of the correlation between the variables in a model. The multicollinearity can be evaluated by examining the correlation matrix and the variance inflation factor (VIF). The VIF identifies the correlation between independent variables and provides an index for the strength of correlation, that is, severity of existence of multicollinearity. Montgomery et al. (1992) and Adams et al. (2015) suggested that a VIF equal to or less than 5 indicates a moderate correlation and that a VIF greater than 5 implies critical levels of multicollinearity. Table 4-1 shows an example of the correlation coefficient among PWV, P, T, and RH over the stations in the training dataset station and for *right before* classes for our selected test event, which is Hurricane Matthew in 2016. The *right before* class is selected to be used for driving the model coefficient in this section because it is the most important class in the prediction of the hurricane's development. It should be emphasized that the *right before* model is most influential for the purposes of this study to determine the rainfall path during the hurricane because it evaluates the conditions before the passage of the storm front.

Table 4-1: Correlation matrix of variables

Variables	PWV	P	T	RH
PWV	1	-0.760	0.297	0.754
P	-0.760	1	-0.046	-0.719
T	0.297	-0.046	1	-0.243
RH	0.754	-0.719	-0.243	1

Table 4-2 provides multicollinearity statistics for each variable in the model. The statistics include R-squared value (R^2); the tolerance factor, which is (1-R^2); and VIF, which equals the inverse of the tolerance factor. A high value for R^2 and a VIF value greater than 5 may cause nonsignificant parameter estimates in the regression owing to the multicollinearity problem.

Table 4-2: Multicolinearity statistics

	PWV	P	T	RH
R^2	0.840	0.628	0.595	0.815
Tolerance	0.160	0.372	0.405	0.185
VIF	4.235	2.686	2.470	4.416

As shown in Tables 4-1 and 4-2, moderate to significant correlations exist between the tested meteorological parameters. To avoid the multicollinearity from the suggested statistical model, PCR is applied, which is based on the principal component analysis (PCA). The PCA extracts the maximum variance of a dataset as a factor in an iterative process. The resulting factor represents the vector that maximizes the dispersion of the observations (Yahoodik et al.2020; Tahami and Fakhravar 2020). The first principal component (PC) accounts for the largest variability in the data, and each succeeding component accounts for the next biggest variability of the remaining property in the data. PCs are uncorrelated orthogonal linear functions of the original variables obtained by a transformation of the form (Wasimi 1990; Zuur et al. 2010):

$$F = ZA \qquad (4\text{-}3)$$

where F is a set of PCs, Z is a set of original variables, and A is a set of eigenvectors associated with significant eigenvalues obtained from the correlation matrix of the original variables (Zuur et al. 2010). In PCR, the independent variables are standardized to avoid the noncommensurate unit problem of the variables so that:

$$Z = [Z_{tj}] \qquad (4\text{-}4)$$

where t = 1, 2, …, n and j = 1, 2 ,…, p and Z_{tj} is described as

$$Z_{tj} = \frac{X_{tj} - mean(X_{tj})}{std\,(X_{tj})} \qquad (4\text{-}5)$$

where X_{tj} is $\Delta PWV, \Delta P$, ΔT and ΔRH. The Kaiser-Meyer-Olkin (KMO) measure of sampling adequacy and Bartlett's test of sphericity are used to evaluate the suitability of data for factor analysis. The KMO statistic indicates if each variable in a data set is predicted without error by the other variables. KMO can vary between 0 to 1, the higher values (close to 1.0) generally indicate that a factor analysis is useful with the data set. If the value is less than 0.50, the results of the factor analysis is unacceptable for factor analysis. Moreover, Bartlett's test of sphericity tests the hypothesis identifies if the correlation matrix is an identity matrix, which would indicate that the variables are unrelated and therefore unsuitable for factor analysis. Small values (less than 0.05) of the significance level (of 95%) indicate that a factor analysis is suitable for factor analsysis. Therefore, the significant Chi-square value at a 95% confidence level, and the KMO statistic of greater than 0.50 for all variables confirms that PCA is valid for further analysis of data. In the next step, the eigenvalues and eigenvectors are computed from the correlation matrix of the standardized independent variables.

Table 4-3: Eigenvectors resulting from PCA

	F_1	F_2	F_3	F_4
ΔPWV_t	0.588	0.236	0.354	0.088
ΔP_t	-0.575	0.004	0.815	0.071
ΔT_t	0.342	0.921	0.030	-0.082
ΔRH	0.568	-0.309	0.235	-0.013

Table 4-3 shows the correlation among the meteorological variables in Table 4-1 and their PCs (F1–F4). Clearly, the first PC is substantially correlated with PWV, pressure, and relative humidity. The second and third components are correlated with temperature and pressure, respectively. However, the fourth PC is moderately not correlated with the explanatory variables. The contribution of each factor to the total variability of the dataset is shown in Table 4-4.

Table 4-4: Eigenvalues explain most of the variability in data

	F_1	F_2	F_3	F_4
Eigenvalue	2.491	1.157	0.266	0.085
Variability (%)	62.282	28.935	6.662	2.121
Cumulative %	62.282	91.217	97.879	100.000

This demonstrates that the first PC (F_1) accounts for 62.28% of the system variance, while the second (F_2), third (F_3), and fourth (F_4) components account for 28.93%, 6.66%, and 2.12%, respectively. Because reduction of dimensionality is a goal of PCA, several criteria have been applied for determining the proper number of PCs that should be kept in the analysis. Kaiser (1960)

proposed dropping components whose eigenvalues are less than one because these provide less information than is provided by a single variable. Jolliffe (1972) suggested using a cutoff on the eigenvalues of 0.7 when correlation matrices are analyzed. Other authors noted that if the largest eigenvalue is close to one, then holding to a cutoff of one may cause useful components to be dropped. However, if the largest components are several times larger than one, then those near one may be reasonably dropped. Another criterion is to preset a certain percentage of the variation that must be accounted for and then keep enough components so that this variation is achieved (reference: NCSS Chapter 425). For this case study, the total percentage that explains variation is set to larger than 95%. Therefore, all PCs up to a predetermined total percentage of explained variation should be included, and the remaining components should be ignored in the analysis. Therefore, based on the contribution of each component in the dataset and factor loadings of PCs, the first three PCs were chosen for the PCR. The selected PCs explain more than 97% of the variance. The regression model is then described as:

$$y = Fb + e \qquad (4\text{-}6)$$

where y is a dependent variable, F represents PCs, b is the regression coefficients to be estimated, and e indicates an error term.

4.4. Model parametrization

The PCR model in eq. (4-6) generates the set of coefficients for the PCs. The set of regression coefficients shown as b vector in eq. (4-6) as well as the 't' statistic for each coefficient are provided in Table 4-5. A t-test and the corresponding p-values are performed to test a null hypothesis and evaluate the significance of each component in the regression model. The null hypothesis is that the regression equation does not explain the significant variation of a dependent variable; that is, the regression coefficients are equal to zero. The p-values are compared with a significance level (0.05 in this study) to evaluate the null hypothesis. If the p-value for a variable is less than the significance level, the null hypothesis will be rejected.

Table 4-5: Principal component regression coefficients

	VALUE	STANDARD ERROR	T-TEST	Pr
b_1	0.928	0.004	207.867	< 0.0001
b_2	0.254	0.003	56.882	< 0.0001
b_3	0.183	0.004	40.866	< 0.0001

Based on the t-test values and their corresponding p-values, and given the significance level of 5%, the information brought by the following variables is statistically significant and provides significant information to explain the variability of the dependent variable (PWV). When the nonzero regression coefficients are statistically significant, the calculated coefficients can be used to form a PCR model. By applying the derived coefficients to each factor in eq. (3-6), the final model is described as follows:

$$\Delta PWV_{t+1} = b_1(F1) + b_2(F2) + b_3(F3) + e \qquad (4\text{-}7)$$

To validate the model, two statistical tests, including a normality test and evaluation of residuals' autocorrelation, are performed. Though the normal distribution of independent variables is not essential to perform PCR, the normality of PCR residuals is a critical requirement for the ability to use the standard critical value for statistics tests such as t- and F-test. Moreover, autocorrelated PWV residuals lead regression coefficients to be statistically insignificant and make statistic tests unreliable. Therefore, the normality test and autocorrelation function are used to evaluate the conditions of normal distribution and detection of autocorrelation respectively. The proposed statistical model quantifies the relationship between the predicted PWV ROC and meteorological variables. The model is further extended to predict the path of the hurricane by utilizing the behavior of the PWV ROC as a significant indicator of predicting different intensity and duration of the event.

4.5. Validation of the prediction model

For each class in the hurricane development phases represented in Figure 4-2, the derived coefficients from the training dataset are applied to all other CORSs in the independent test dataset to compute the residuals of the models. The reliability of the prediction model is validated by calculating the residuals of the PWV measurements for each model. As an example for the chosen case study, Hurricane Matthew in 2016, the coefficients derived for each class from the training dataset are applied to a CORS in Florida, CCV6, to predict PWV for each class for CCV6. Figure 4-3 depicts the predicted PWV at CCV6 over the period of October 5–12, 2016 and the corresponding residuals using a one-hour prediction model for all classes of event. The bottom panel in Figure 4-3 shows that the residuals of the predicted PWV from the estimated PWV are generally extremely low. The amplitude of the residuals is about 5–10% of the amplitudes of the corresponding PWV. A significant rise in the residual is found at the *after* class, possibly owing to the fact that the prediction models are derived based on the PWV fluctuation during the rainfall so that they are not sensitive to non-rain scenarios such as the *after rain* event. Moreover, the maximum residuals are within the first or last epochs of the corresponding class in each model except the *after* class. This is because of the transition from one model to another.
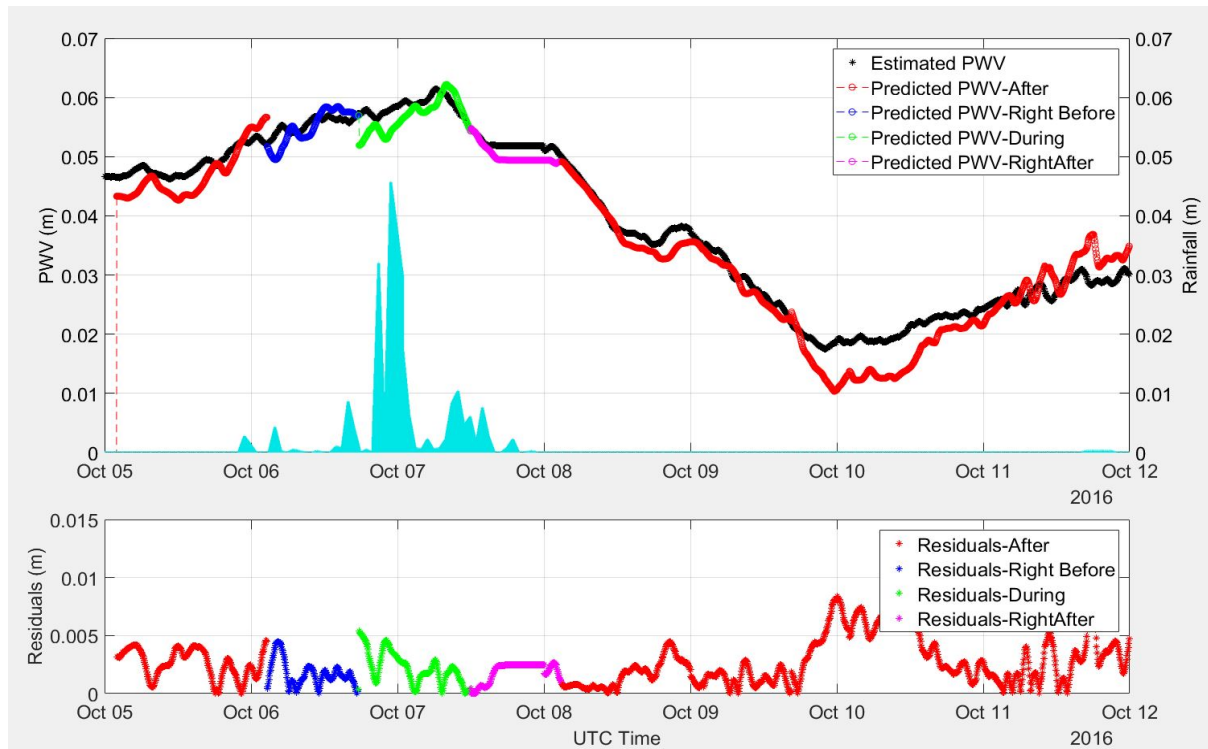
Figure 4-3: Prediction models and the corresponding residuals for CCV6 during October 5–12, 2016; the top panel shows the models in different colors that are mapped over the actual PWV time series (black line), and the blue bars represent the recorded actual rainfall on the station for the mentioned period; the bottom panel shows the residuals of observations with respect to each model

The demonstrated statistical model for predicting PWV can then be used to obtain the temporal variation of PWV at a particular site. By observing the temporal variation of PWV at multiple sites simultaneously, the spatial variation of PWV at a certain epoch can be monitored and analyzed to be applied to forecast the path of a severe weather event, which will be described in Chapter 5.

CHAPTER 5

5. EXPERIMENTS AND RESULTS

Based on the relationship among GNSS-derived PWV ROC and other atmospheric parameters, which are pressure, temperature, and relative humidity, a short-term forecasting method was established in Chapter 4. From the model, the temporal variation of PWV at a particular site can be obtained. By observing the temporal variation of PWV at multiple sites simultaneously, the spatial variation of PWV at a certain epoch can be monitored, and the residuals of PWV from the model are analyzed. In Chapter 4, four PWV prediction models were introduced and defined as a different stage of precipitations. For each model, PWV measurements are compared and the residuals are computed, namely PWV residuals. The site with the minimum residuals for each prediction model site indicates the location of best fit to the actual observations on the specific time window. The PWV residual can be applied to forecast the spatial movement of a severe weather event, such as a hurricane. The distribution pattern and the magnitude of the PWV residual to the prediction model can be applied for determining the direction of the hurricane path. The distribution pattern of minimum PWV residuals is demonstrated by forming clusters in the local area and is used for determination of precipitation path during the hurricane. Moreover, a full analysis of several hurricane categories is performed in this chapter to support the use of GNSS-derived PWV for prediction of the track and intensity of a hurricane accompanied with different levels of precipitation. For each case study, the coefficients of a *right before* model are derived as described in Chapter 4 to predict PWV. The residuals of PWV for the *right before* model are utilized for forecasting hurricane-induced precipitation.

5.1. Description of case studies

To validate the suggested methodology in Chapter 4, four major hurricane events in 2016–2018 were selected. In selection of the case studies the following factors were considered to be evaluated, 1) how different climate characteristics at different locations can affect the prediction results from the proposed methodology, 2) how effective is the proposed methodology by comparison of the case studies occurred at the same location and similar climate characteristics but in different times, and 3) how the proposed methodology can respond to different severity of the storm. The case studies are listed as follows:

Case 1: Hurricane Matthew in October 2016

Hurricane Matthew is one of the most destructive and long-lived hurricanes in the United States. Hurricane Matthew's path caused substantial damage in the US during October 2016. The major landfalls in the United States were along the coasts of Florida, South Carolina, and North Carolina. Overall, 585 direct deaths were attributed to Hurricane Matthew, with more than 500 deaths occurring in Haiti, making Matthew the deadliest Atlantic hurricane since Hurricane Stan in 2005 (NHC Hurricane Matthew report 2017). On October 5–7, 2016, Hurricane Matthew made landfall on the east coast of Florida and was designated as a Category 4. On October 7, Hurricane Matthew's center moved along the Florida coast, but it remained offshore and was designated a Category 2. On the same day, some parts of Georgia experienced significant flooding as Hurricane Matthew's eye traveled northward off the state's coast. During October 8, the eye of Hurricane Matthew approached South Carolina, causing massive flooding in that area as the storm weakened to a Category 1. Then it passed through North Carolina, resulting in severe rainfall. On October 9, Matthew moved from the US east coast and traveled toward the Atlantic Ocean; hence it is

recorded as a post-tropical storm. The effects of Hurricane Matthew on October 10, observed along the North Carolina border.

To retrieve the PWV from GNSS data, a network of thirty-eight Continuously Operating Reference Stations (CORS)s was formed that are regionally distributed along the coasts of Florida, Georgia, and South and North Carolina, and the seven days (October 5–11, 2016) of CORS observations were processed. The PWV was retrieved by proceesing only GPS observations. Fourteen weather stations close to the CORS stations were utilized for this experiment, providing three meteorological parameters: pressure, temperature, and relative humidity. The average interstation distance in the test site is 120 km. The temporal resolution of the GNSS-derived PWV and the meteorological parameters are 5 and 60 minutes, respectively. To jointly process the GNSS data and the meteorological data for the statistical analysis, the meteorological data are temporally interpolated at every 5 minutes. Figure 5-1 shows the geographical distribution of the GNSS CORS and meteorological stations over the study area. It should be noted that for all case studies the number of CORS or weather stations in the area is more than the represented stations in the figure. The represented stations were selected based on data availability during the time of case studies. The figure also indicates the severity of the hurricane and the corresponding location with the time tag with the format of reported time in yyyymmddhh. The reported path and associated hurricane time are based on the reported data from the NHC (https://www.nhc.noaa.gov/gis/). The storm severity scale shown in Figure 5-1 and other figures in this chapter varies among 0, 1, 2, 3, and 4, and each scale is assigned to a different storm type. The storm scale of 0 is defined for the tropical storms, and scales of 1, 2, 3, and 4 represent the hurricane categories 1, 2, 3, and 4, respectively. The Saffir-Simpson Hurricane Wind Scale is generally used for hurricane classification based on the hurricane's intensity at the indicated time (Pielke et al. 2008).

Figure 5-1: The representation of Hurricane Matthew's path and geographic distribution of stations over the study area

Case 2: Hurricane Harvey in August–September 2017

Hurricane Harvey started as a typical weak August tropical storm that affected the Lesser Antilles and dissipated over the central Caribbean Sea. However, after reforming over the Bay of Campeche, Harvey rapidly intensified into a category 4 hurricane (on the Saffir-Simpson Hurricane Wind Scale) before making landfall along the middle Texas coast (NHC Tropical Cyclone Report 2017). The storm then stalled, with its center over or near the Texas coast for four days, dropping historic amounts of rainfall of more than 60 inches over southeastern Texas. The rains caused catastrophic flooding, and Harvey is the second most costly hurricane in US history, after accounting for inflation, behind only Katrina (2005) (NHC Tropical Cyclone Report 2017). Hurricanes reaching Category 3 and higher are considered major hurricanes because of their potential for significant loss of life and damage. Category 1 and 2 storms are still dangerous, however, and require preventative measures. To investigate the GNSS-derived PWV during the selected event, 10-day (August 23–31, 2017) observations of selected CORS were used to track the path of the hurricane. In this study, a network is formulated, which consists of twenty two CORS stations and seventeen meteorological stations. The nearby weather stations to the CORS stations were utilized for this experiment to provide meteorological parameters in one hour of temporal resolution as described in Case 1. The GNSS and meteorological stations were selected based on the data availability between August 23 and 31, 2017, including the event period covering a few days before, during, and after the severe hurricane event. Figure 5-2 shows the geographical distribution of the GNSS CORS and meteorological stations and the hurricane's path over the study area.
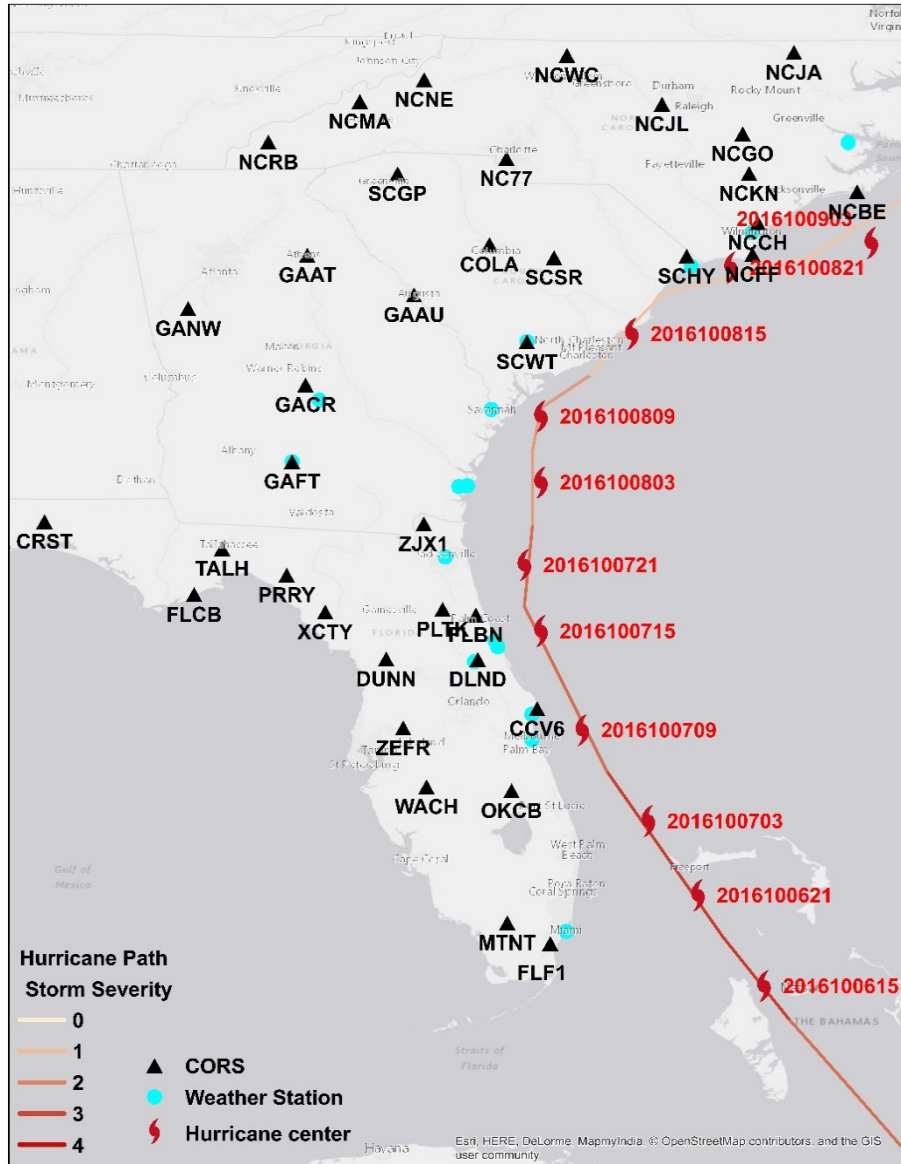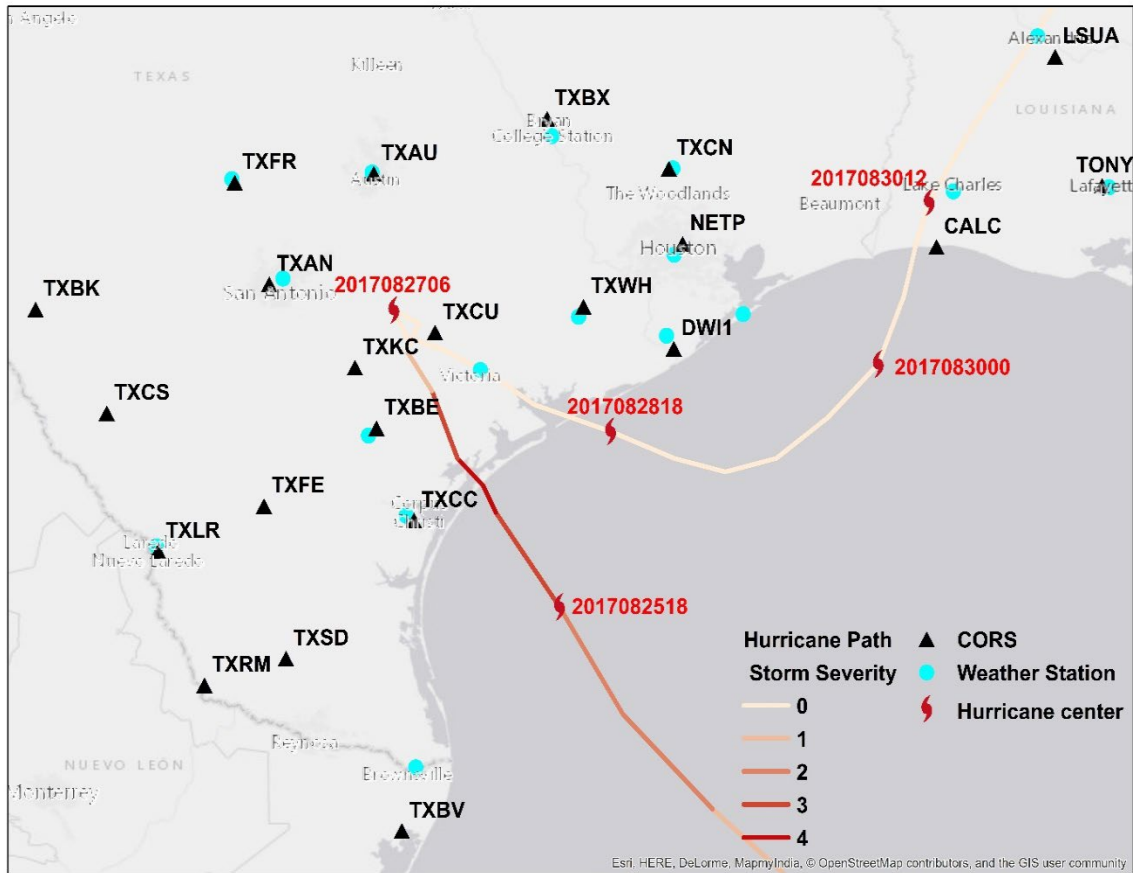
Figure 5-2: The representation of Hurricane Harvey's path and geographic distribution of stations over the study

Case 3: Hurricane Irma in August–September 2017

Irma was a long-lived Cape Verde hurricane that reached category 5 intensity on the Saffir-Simpson Hurricane Wind Scale. The catastrophic hurricane made seven landfalls, four of which occurred as a category 5 hurricane across the northern Caribbean Islands. Irma made landfall as a category 4 hurricane in the Florida Keys and struck southwestern Florida at category 3 intensity. Irma caused widespread devastation across the affected areas and was one of the strongest and costliest hurricanes on record in the Atlantic basin. The distribution of the CORS and meteorological stations, the hurricane's path, and rainfall map over the study area are presented in Figure 5-3. The data selected covered September 8–15, 2017, to include a few days before, during,

and after the hurricane event. Although some parts of the study area affected by Hurricanes Mathew and Irma are similar, covering certain parts of Florida and Georgia, the distribution of CORS stations is different in each study area. This is explained by 1) the GNSS data availability during each hurricane's lifetime and 2) the different direction of the hurricanes' development inside the land. The direction of the hurricane's development changed from the northeast direction in Hurricane Matthew to the northwest direction in Hurricane Irma. Therefore, some CORS stations are selected differently in the case of Hurricanes Harvey and Mathew to ensure that the CORS stations with available observations cover the area along with the hurricanes' path.
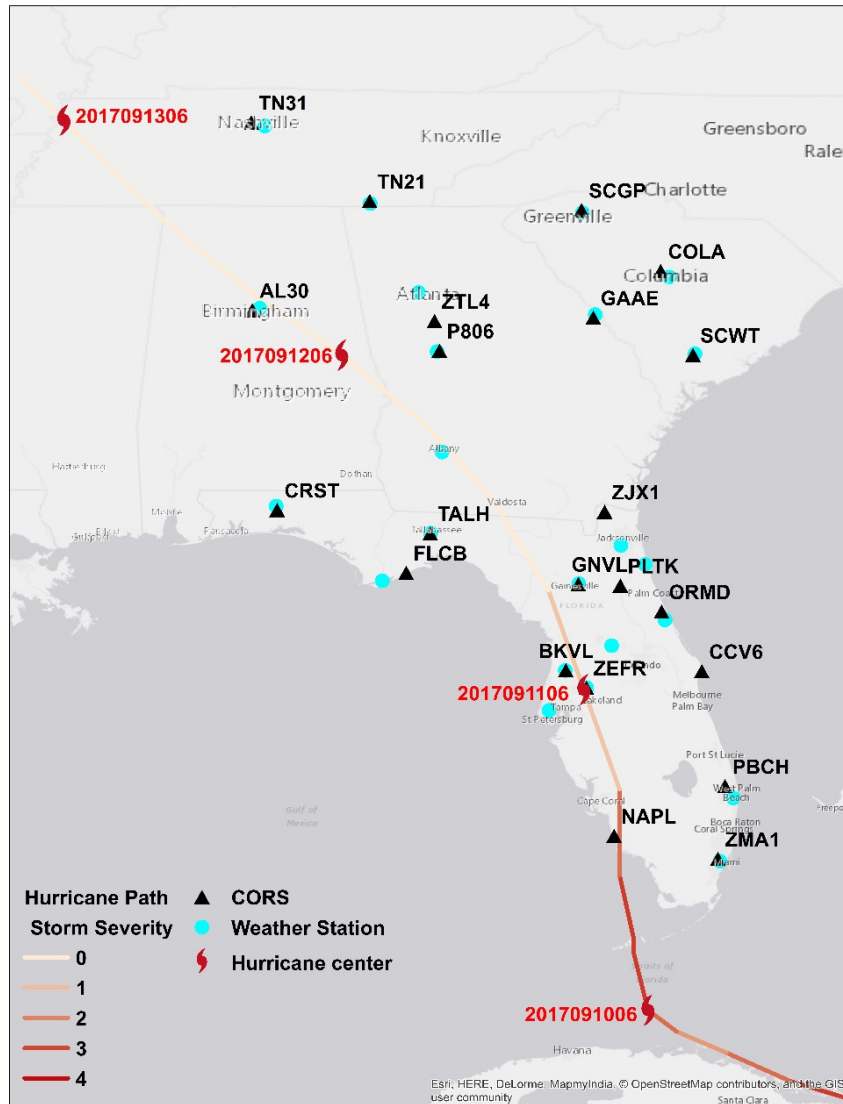
Figure 5-3: The representation of Hurricane Irma's path and geographic distribution of stations over the study area

Case 4: Hurricane Florence in August–September 2018

Hurricane Florence was a long-lived Cape Verde hurricane and the wettest tropical cyclone on record in the Carolinas. Florence became a tropical depression near Cape Verde on August 31 and progressed west-northwest, becoming a tropical storm on September 1. Florence strengthened rapidly on September 4–5, becoming a Category 4 storm on the Saffir-Simpson wind

scale. Florence weakened to a tropical storm by September 7, but the system regained hurricane strength on September 9 and attained major hurricane status with winds of 140 mph on September 10. By the evening of September 13, Florence had been downgraded to a Category 1 hurricane. Hurricane Florence made landfall near Wrightsville Beach early on September 14 and weakened further as it slowly moved inland. Florence produced extensive wind damage along the North Carolina coast from Cape Lookout across Carteret, Onslow, Pender, and New Hanover counties. The historic legacy of Hurricane Florence was a record-breaking storm surge of 9–13 feet and devastating rainfall of 20–30 inches, which produced catastrophic and life-threatening flooding.

To study the Florence hurricane, seventeen CORS covering the landfall area were selected during September 12–19, 2018. Figure 5-4 shows the distribution of CORS and weather stations as well as hurricane's path over the study area.
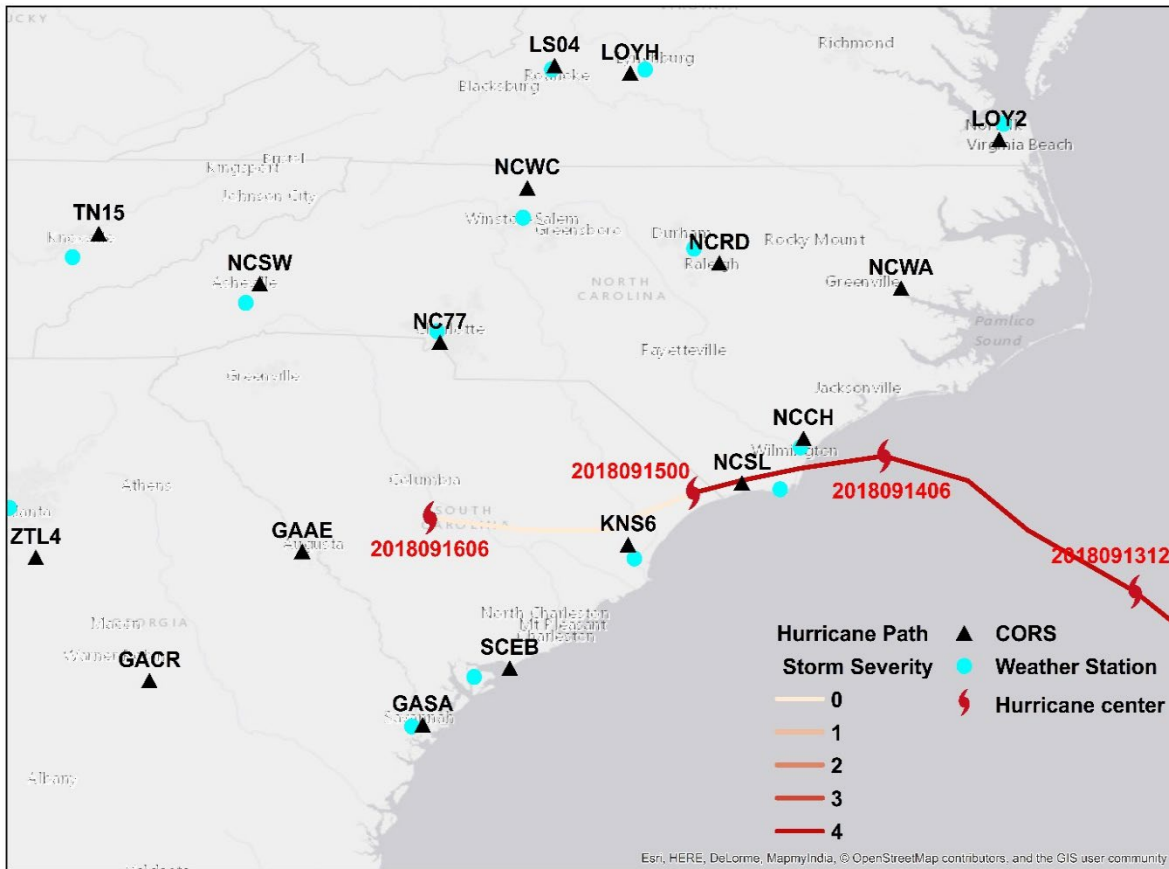
Figure 5-4: The representation of Hurricane Florence's path and geographic distribution of stations over the study area

5.2. Experiments: Spatiotemporal analysis of PWV for predicting hurricane paths

In this section the methodology described in Chapter 4 is applied to the aforementioned case studies, and the experiment results are presented.

Hurricane Matthew

To investigate the PWV responses to the storm front, the PWV residuals of *right before* and *right after* models are derived for all stations in the study area for each hurricane case. Figures 5-5 and 5-6 present the residuals of PWV for a one-hour prediction model for Hurricane Matthew. Figure 5-5 shows the PWV residuals for a *right before* model when the rain event approached Florida during Hurricane Matthew, and Figure 5-6 shows the PWV residual for a *right after* model when the rain event passed that area. In Figure 5-6, the increase of residuals at Florida stations corresponds to the time period when the extinction of the convective storm in the area was observed.
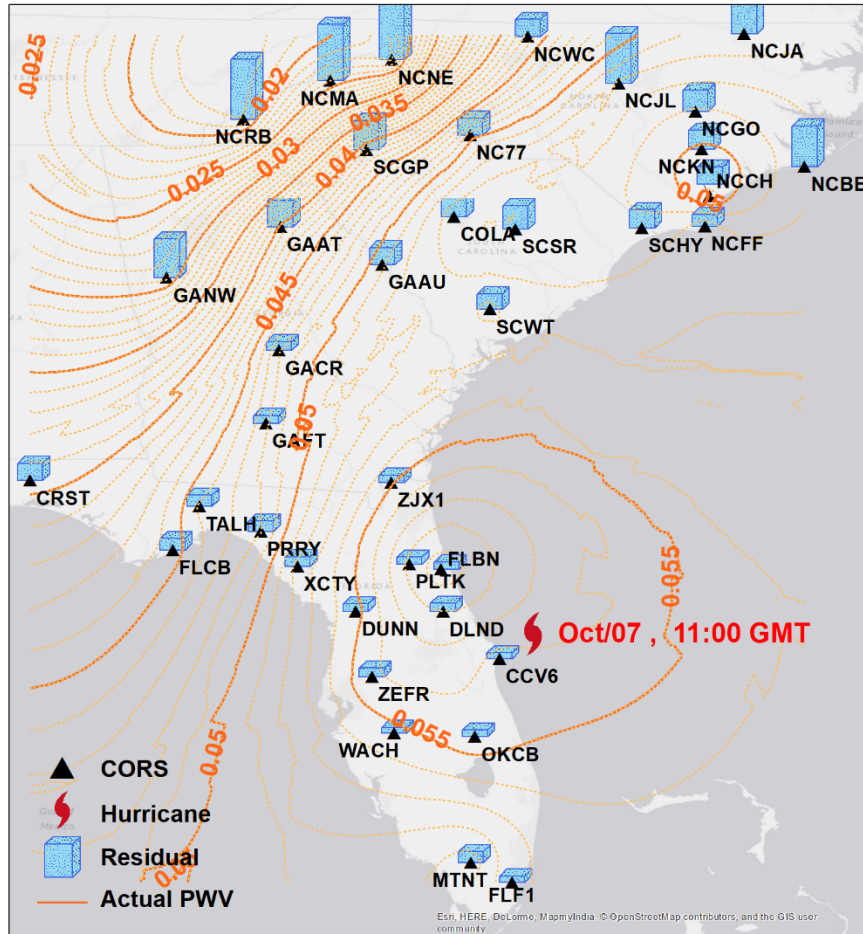
Figure 5-5: Distribution of actual PWV and the residuals for the *right before* model on October 7 at 11 a.m. over the area corresponding to Hurricane Matthew. The red hurricane mark shows the actual reported time and location of the hurricane eye provided by NHC
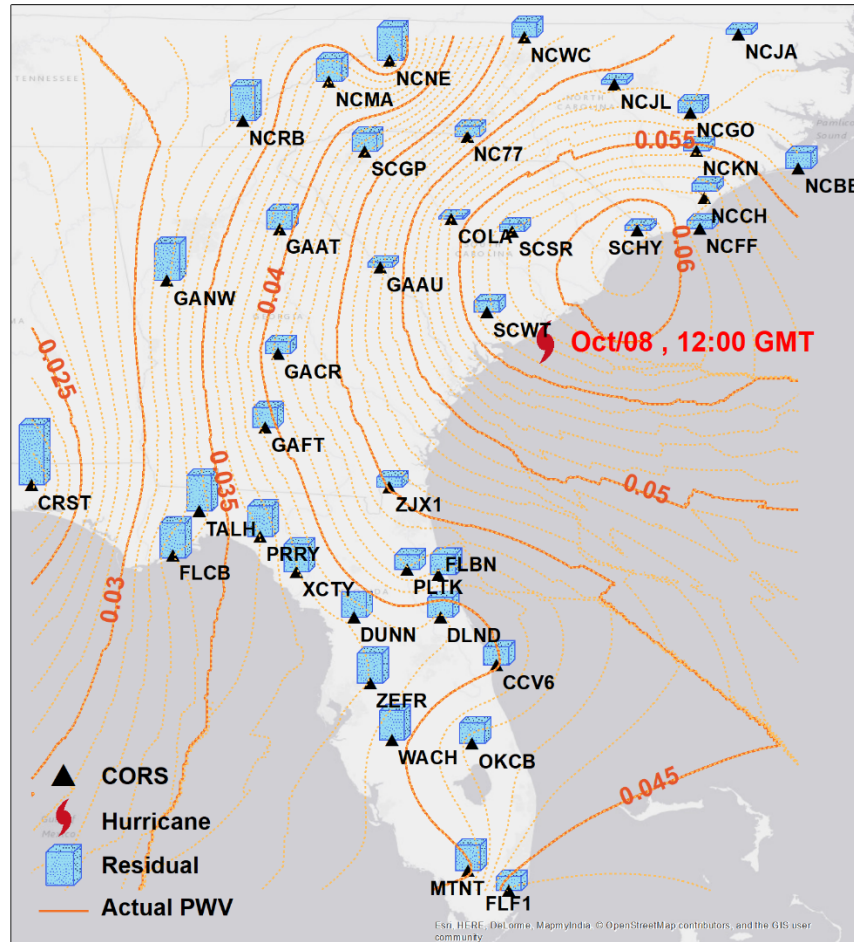
Figure 5-6: Distribution of actual PWV and the residuals for the *right after* model on October 8 at 12 p.m. over the area corresponding to Hurricane Matthew. The red hurricane mark shows the actual reported time and location of the hurricane eye provided by NHC

The experimental results in both prediction models show the distribution pattern of the residual bars, the magnitude, and the actual observed PWV in the region. They also show that the location of the minimum residuals along the hurricane days agree with the observed rain pattern, which is used for prediction of the hurricane path. The smaller residual appeared a few hours before the hurricane passage, demonstrating a higher concentration of the rainfall in the area of the *right before* model. In this model, the larger residuals corresponded to either 1) the area not yet affected

by the hurricane or 2) the area where rain ceases; that is, the area with smaller residuals can be considered as a probable area to be affected by a hurricane.

Table 5-1 presents the statistics for the residual of the observed PWV of the *right before* model over different time lags at CCV6 for Hurricane Matthew. Because the *right before* model is most influential for determining the hurricane path by evaluating the condition before the passage of the storm front, this study is mostly focused on this prediction model.

The hurricane path can be determined by observing the predictions of PWV at multiple sites in different directions. The stations with the minimum residuals of the *right before* model can be considered as an indicator for the most probable region to be affected by the hurricane. The residuals of the *right before* model at those sites are compared for the prediction time lags of 1–24 hours over the study area.

Table 5-1: Residuals for the prediction model (right before the hurricane) in prediction time lags (unit: mm)

	1h	6h	12h	24h
Mean	4	3	3	3
Standard deviation	0.01	0.09	0.01	0.01

Considering the uncertainty from the measurement noise and other error sources in the GNSS-derived PWV, the residual PWV at multiple sites are evaluated within the grids of 200×200 km^2 in the test area. The grid size was determined based on the area of the test site and the geometric distribution of available CORS. Figure 5-7 presents the residuals to the *right before* models at the stations in the Hurricane Matthew study area for 12-hour and 24-hour forecasts in Figures 5-7 (a) and 5-7 (b), respectively. In Figure 5-7, each cell is wide enough to cover multiple

CORSs, which reduces the risk of failure or error of a particular station. Furthermore, the cell is small enough to distinguish the directions of potential paths of hurricanes. The optimization of grid size determination based on the distance between available CORS as well as the area coverage is left for the future. Unlike the conventional method of NHC forecast, which provides the different size of probability circles for the location of hurricane eyes, our proposed approach indicates the most probable cell for the hurricane path with the mean and standard deviation of the model residuals.
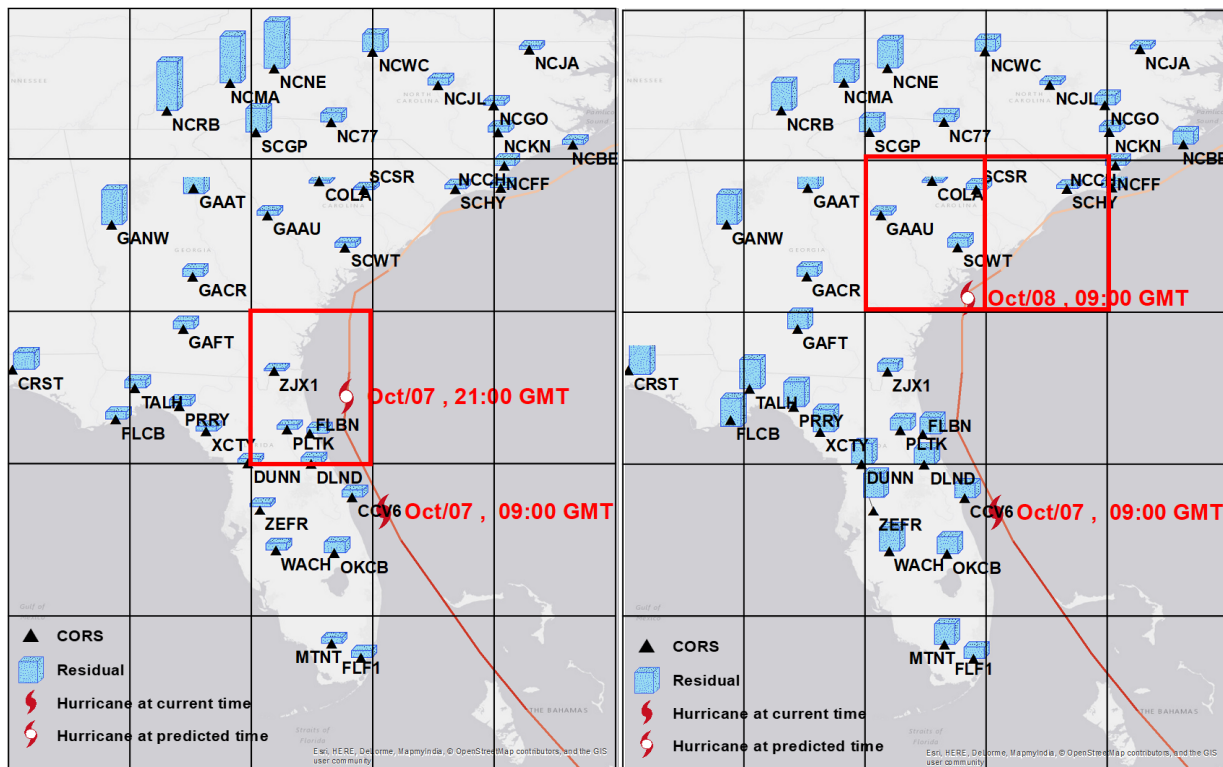
Figure 5-7: Predicted residuals over the study area by applying prediction model to CCV6 at Hurricane Matthew on October 7, 2016. The hurricane hit the area close to CCV6 on October 7 at 9 a.m. GMT. The red hurricane mark shows the reported time and location of the hurricane provided by NHC. The red curve shows the reported hurricane path. Red grids show the stations that fall into the hurricane's path, and black grids show the stations located outside the hurricane's eye. The residuals correspond to the *right before* model in 1h and 24h time prediction lead time in the left panel and right panel, respectively

CCV6 is located at the area where Hurricane Matthew landed at around 9 a.m. on October 7. The *right before* model is applied to CCV6 station, and the residuals for different time lag intervals are shown in the figures. The hurricane's path is determined based on the direction of grids containing the sites with the smallest residuals among all grids. Figure 5-7 (a) shows the observational residuals of the *right before* model on CCV6 station in the 12h prediction time lag. The red line in figures is the reported path during the hurricane's lifespan from NHC. The reported time of the hurricane's eye along this path is presented in Fig 5-1.

Based on the residuals, two types of grid clusters of stations are specified. The grid cluster in red indicates the stations with the lowest residuals, while the other cluster in the black grid contains the stations with the higher rate of residuals. By comparing the average residuals within each grid, the hurricane path can be predicted in each time frame. The observations from 9–10 a.m. on October 7 are then used in a 24h prediction time lag to predict the path. As shown in Figure 5-7 (b), the cluster with the minimum residual determining the path of hurricane-induced precipitation is moving toward the northeast 24 hours after the reference time. Moreover, the residuals within the corresponding cluster can also be used to investigate the intensity of rainfall in the hurricane's path. For instance, among the stations in Figure 5-7 (a), ZJX1 in the red grid represents the lowest residual. This means that after a 12-hour time lag (9 p.m. on October 7), ZJX1 station will be hit more severely by the hurricane than the other stations in the study area. The same strategy is applied for the 24-hour prediction time lag showing the hurricane's movement toward South Carolina and North Carolina on 9 a.m. on October 8. The numerical comparisons of prediction residuals for the grids located inside and outside of the hurricane are provided in Figures 5-8 (a) and 5-8 (b), respectively.

Figure 5-8: Residuals and their standard deviation in parentheses (in mm) for the grids inside Hurricane Matthew (red cell) and outside Hurricane Matthew (white cell). The results in the left panel (Figure 5-8 [a]) and right panel (Figure 5-8 [b]) are attributed to the *right before* prediction model at 9 a.m. on October 7, 2016 (reference time) to predict the PWV after 12h and 24h from the reference time, respectively

As shown in Figure 5-8, the characteristic PWV residual in each cell plays a role as a forecast indicator to predict the path of the hurricane and its relative intensity at different prediction time windows. Regarding the prediction of precipitation's relative intensity, comparing the magnitude of residuals shows that the stations with the lower residuals within that grid show the more severe areas of precipitation during the hurricane. The experimental results shown in Figures 5-7 and 5-8 indicate a sequence of rapidly predicted PWV residual decrements for each station, starting from Florida at 9 a.m. GMT October 7 and reaching South and North Carolina after 24 hours at 9 a.m. on October 8; our experimental result is confirmed by the reported hurricane path in Figure 5-1. Because different hurricanes have their own characteristics, the proposed method was applied to the other hurricane case studies to investigate the versatility of the model with consideration of individual characteristics of each hurricane. The following are the experimental results for Hurricanes Harvey, Irma, and Florence. Two time lags for the *right before* prediction

model were chosen, which were 12 hours and 24 hours in each experiment. To verify the predicted path of precipitation during the hurricane events, radar base reflectivity images from Doppler radar were used to demonstrate the precipitation distribution and its intensity at the selected prediction time. In the base reflectivity image, the radar is located in the center of the image, and the colors represent the strength of returned energy to the radar expressed in values of decibels (dBZ). As dBZ values increase, so does the intensity of the rainfall. When the radar is in precipitation mode, the scale represents dBZ values from 5–75. The scale of dBZ values is also related to the intensity of rainfall. Typically, light rain is occurring when the dBZ value reaches 20. The higher the dBZ, the stronger the rain rate.

Hurricane Harvey

To assess the performance of the *right before* prediction model, it was applied to the Hurricane Harvey study area, which has different geographic features and climate properties in comparison to Hurricane Matthew. Figures 5-9 (a) and (b) demonstrate the distribution of the residuals for the *right before* model at 12h and 24h prediction time lags, respectively. For both prediction cases, the observations on August 25, 2017 at 6 p.m. were used as the observation of the reference time to predict the precipitation path. Numerical comparison of prediction residuals over the study is shown in Figure 5-9. In Figures 5-9 and 5-10, the red grids containing the minimum residuals projected the most probable location of the severe precipitation 12h and 24h later than the reference time at 8 a.m. on August 25 and 6 p.m. on August 26, respectively.
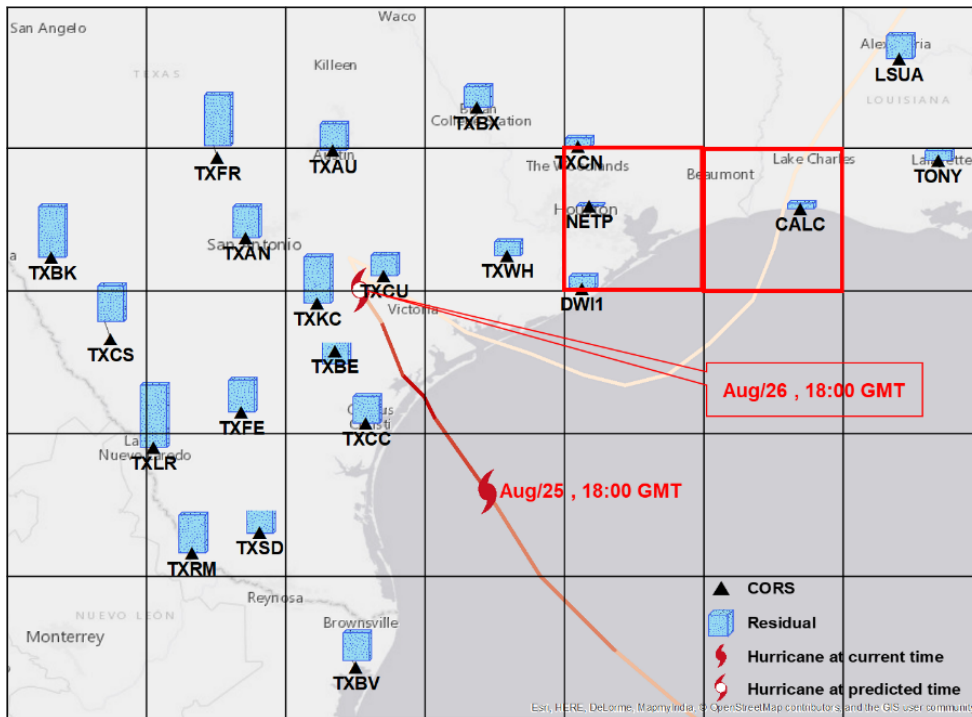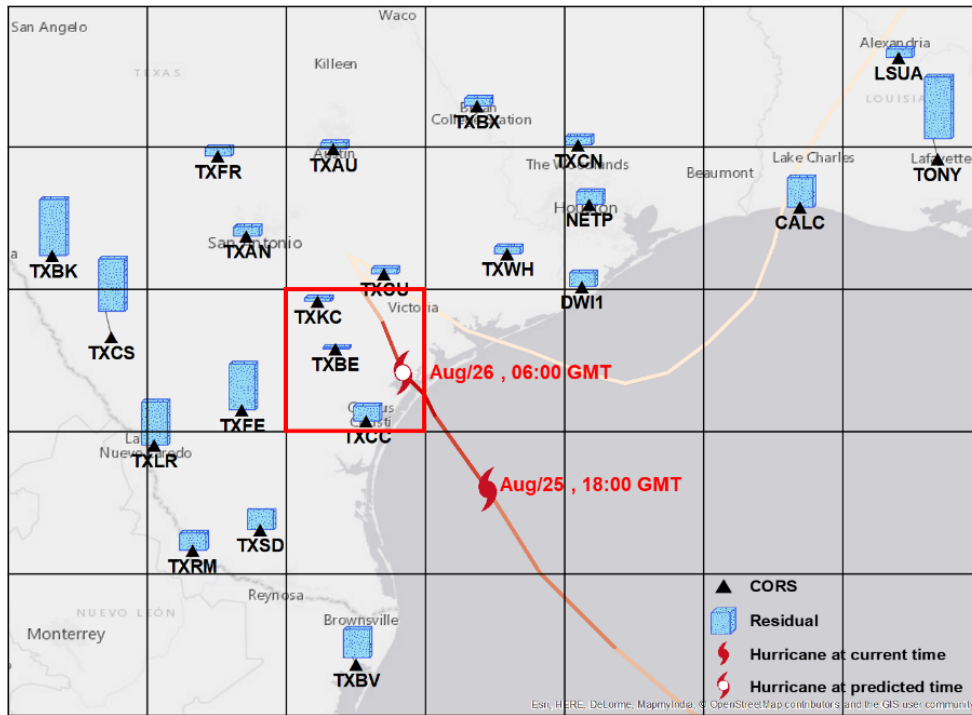
Figure 5-9: Distribution of the prediction residuals related to Hurricane Harvey over the study area. Hurricane Harvey hit the ocean on August 25, 2017 at 6 p.m. (reference time). The residuals corresponding to the *right before* model 12h and 24h later than the reference

time are shown in the upper panel (Figure 5-9 [a]) and lower panel (Figure 5-9 [b] respectively). The red mark shows the time and location of the hurricane reported by NHC

Left panel (Figure 5-10 [a]):

			5(0)			6(0)
39(0)	6(1)	5(0)	5(0)	8(2)	21(0)	44(0)
37(0)	32(0)	4(1)				
	19(3)					
		20(0)				

Right panel (Figure 5-10 [b]):

			11(0)			13(0)
29(0)	23(7)	13(2)	7(0)	4(1)	4(0)	5(0)
20(0)	18(0)	20(1)				
		26(7)				
		15(0)				

Figure 5-10: Residuals and their standard deviation in parentheses (in mm) for the grids inside Hurricane Harvey (red cell) and outside Hurricane Harvey (white cell). The results in the left panel (Figure 5-10 [a]) and right panel (Figure 5-10 [b]) are attributed to the *right before* prediction model at 6 p.m. on August 25, 2017 (reference time) to predict the PWV after 12h and 24h from the reference time, respectively

As Figure 5-10 (b) shows, the predicted path of precipitation is toward the northeast of the reference hurricane's center after 24h from the reference time, while at the same time the NHC-reported center of the hurricane is toward the northwest of the reference hurricane's center. The difference between the predicted path from the *right before* model and the location reported by NHC is ascribed to the fact that the proposed prediction model is aimed at predicting the most intense rainfall and is sensitive to the presence of water vapor content in the area, while the NHC-forecast models are mostly reliant on the presence of wind. In addition, the storm scale was downgraded from hurricane scale 1 at the reference time to a tropical storm at the prediction time (NHC Hurricane Harvey report 2017). This shows that while the storm intensity was downgraded

after 24h from the reference time, the severe precipitation existing in the area can still be predicted by the prediction model. However, the NHC-reported center of the hurricane did not project the location of the severe precipitation because the Saffir-Simpson scale does not account for rainfall levels or storm surges, and those factors have a direct impact on rainfall prediction. Figure 5-11 illustrates the most probable path of precipitation derived from the *right before* model along with the radar reflectivity base image and NHC-reported predicted hurricane path. Comparing the previous results with the radar reflectivity images shows the correlation between the amplitude of the predicted residual and the intensity of the rainfall reflected by the radar images. This is because both figures show that the grids with the minimum residuals are located in the area with the most intense rainfall according to radar images.
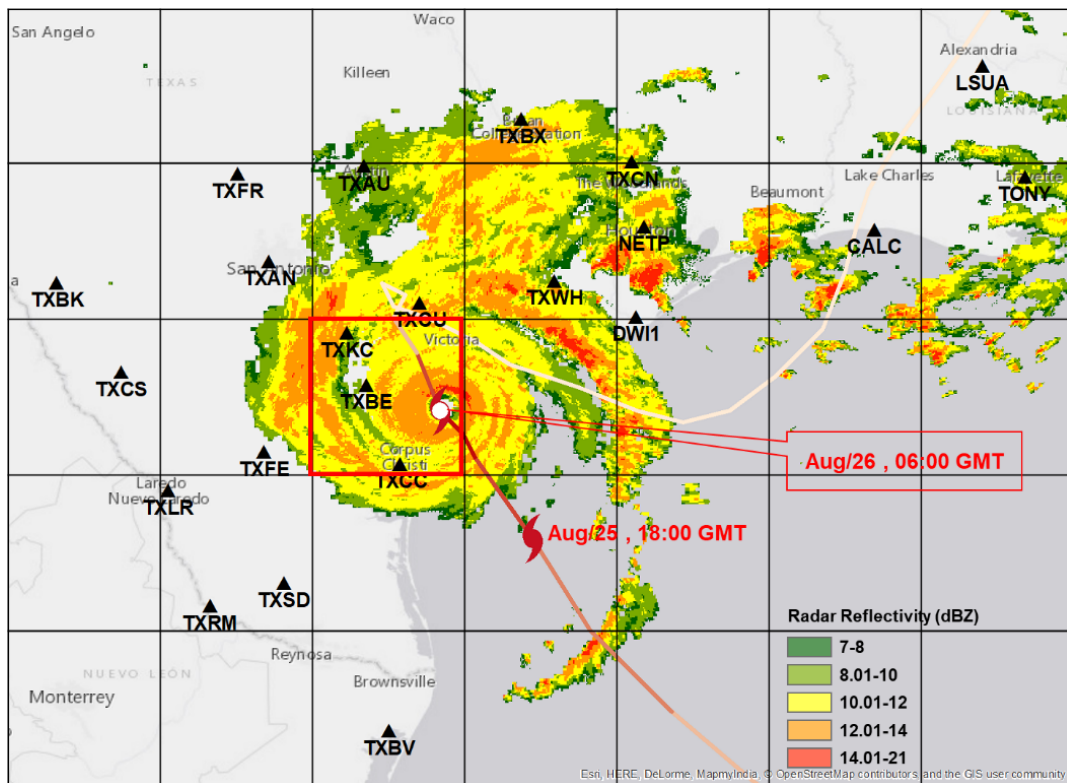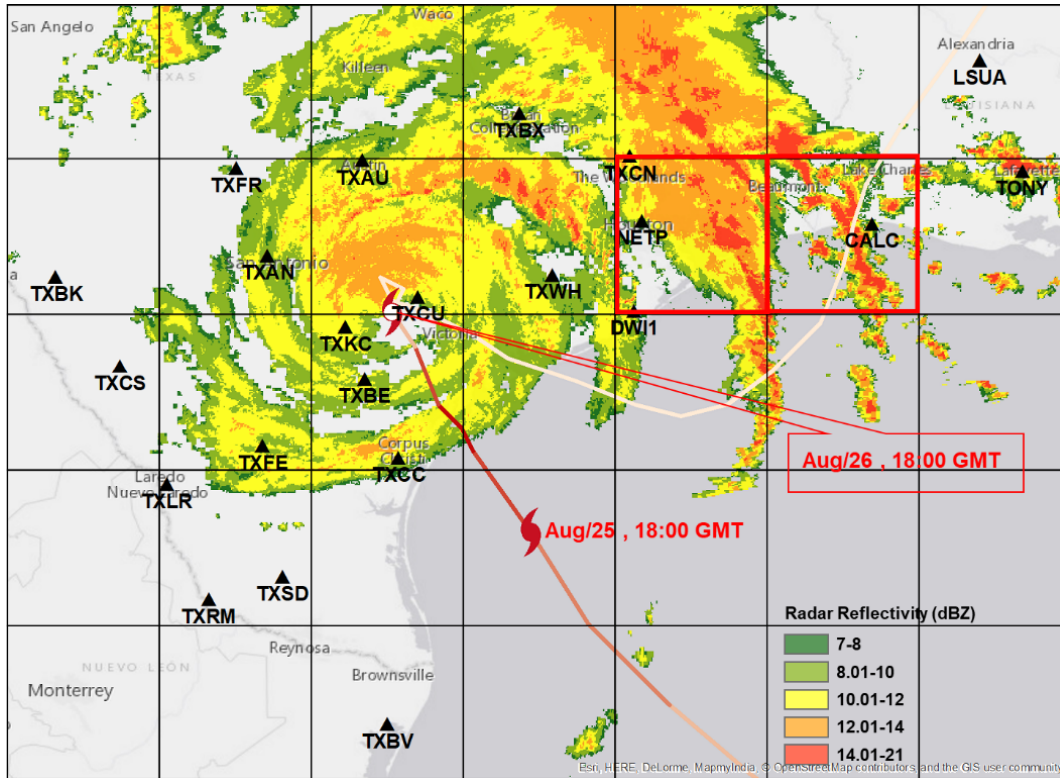
Figure 5-11: Most probable precipitation path during Hurricane Harvey. Hurricane Harvey hit the ocean on August 25, 2017 at 6 p.m. GMT (reference time). The results in the upper figure (Figure 5-11 [a]) and lower figure (Figure 5-11 [b]) are attributed to the *right before* prediction model at the reference time to predict the precipitation path after 12h and 24h from the reference time, respectively. The red mark shows the reported time and location of the hurricane provided by NHC. Radar reflectivity shows the precipitation over the area at the prediction time

Figure 5-12 demonstrates the observed PWV during Hurricane Harvey. According to the reported hurricane path in Figure 5-2, TXCC and TXCU are the CORSs in the most intense area of the hurricane with the storm severity scale of 4 denoting hurricane category 4, while the storms affecting DWL1, CALC, and LSUA are considered tropical storms with storm severity of zero. TXLR is one of the stations outside the hurricane path. The analysis of CORS GNSS time series shows that the lowest amount of PWV during the observation time is associated with the CORSs

located away from the hurricane path (TXLR). Moreover, the PWV fluctuation above the applied threshold (red line in the figure) shows the consistent pattern over time for the stations close to the hurricane eye. In this figure, for all the stations excluding TXLR and LSUA, the PWV fluctuates consistently during August 26, 2017. PWV variation above the threshold during this time is the rainfall indicator at the corresponding time for these stations, as also shown in Figures 5-10 and 5-11.
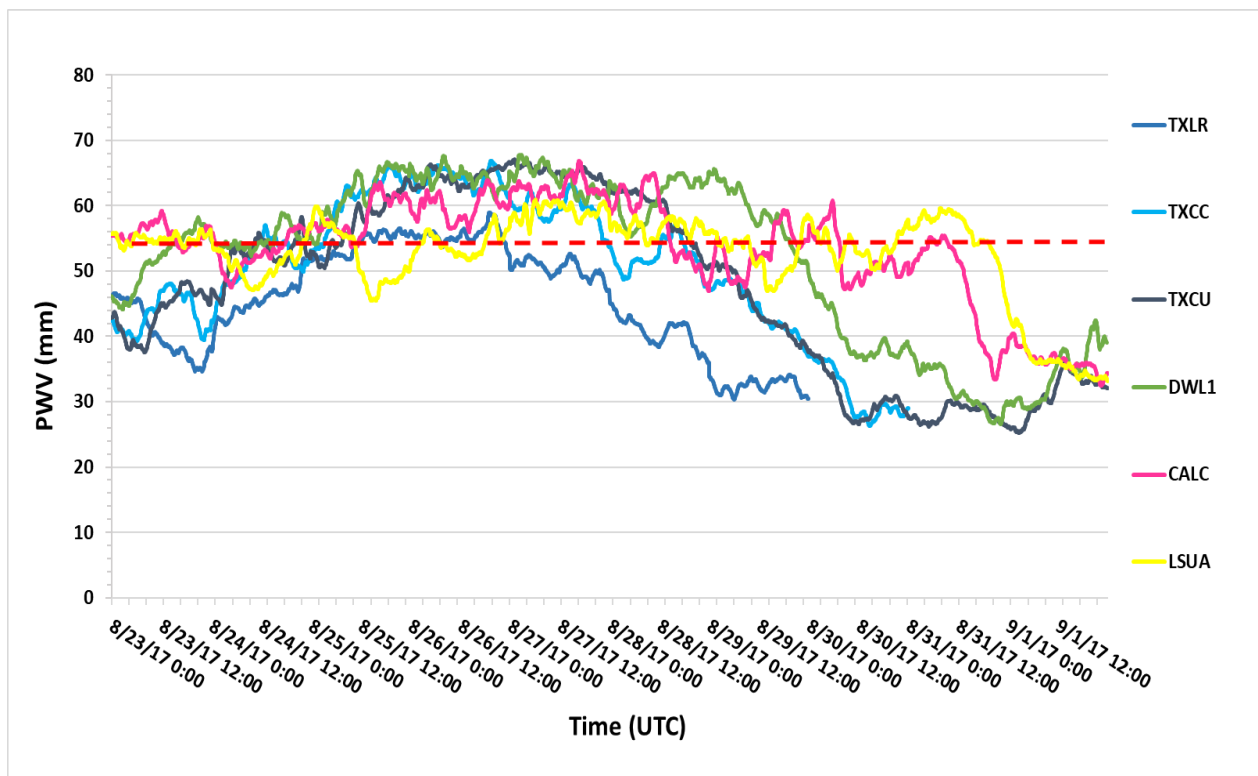
Figure 5-12: Observed PWV variations during Hurricane Harvey over the study area. Time series are associated with selected GNSS CORS inside and outside the hurricane's path. The red dashed line shows the applied threshold for the PWV forecast, which is set to 55 mm for the Hurricane Harvey case study

Hurricane Irma

The performance of the prediction model was also evaluated with the Hurricane Irma case study. For this evaluation, the prediction results for Hurricane Irma can be compared to Hurricane Mathew owing to the similarity of geographic and climate characteristics of the affected areas in both case studies, although the hurricanes occurred in different years. Hurricane Irma hit the area close to NAPL on September 10, 2017 at 6 p.m., which was set as the reference time. The _right before_ model is applied to the stations in the Hurricane Irma case study to forecast the precipitation path for 12h and 24h later than the reference time. Figures 5-13 (a) and 5-13 (b) show the distribution of the prediction residuals for 12h and 24h forecast times, respectively. Figure 5-13 (a) shows that after 12h from the reference time, at 6 a.m. on September 11, 2017, most of the stations in Florida reflect the high intensity of precipitation because of the low amplitude of the prediction residuals. However, the lowest residuals are distributed in the northern part of the reference point, showing that the most severe precipitation path is toward western Florida. On the other hand, after 24h from the reference time, the majority of the stations reflect the higher magnitude of the prediction residuals, showing that the precipitation intensity decreases over time. Comparing the magnitude of residuals in Figure 5-13 (b) shows that the intense part of precipitation exits Florida and enters northwest neighboring states 24h later than the reference time at 6 p.m. on September 11, 2017.
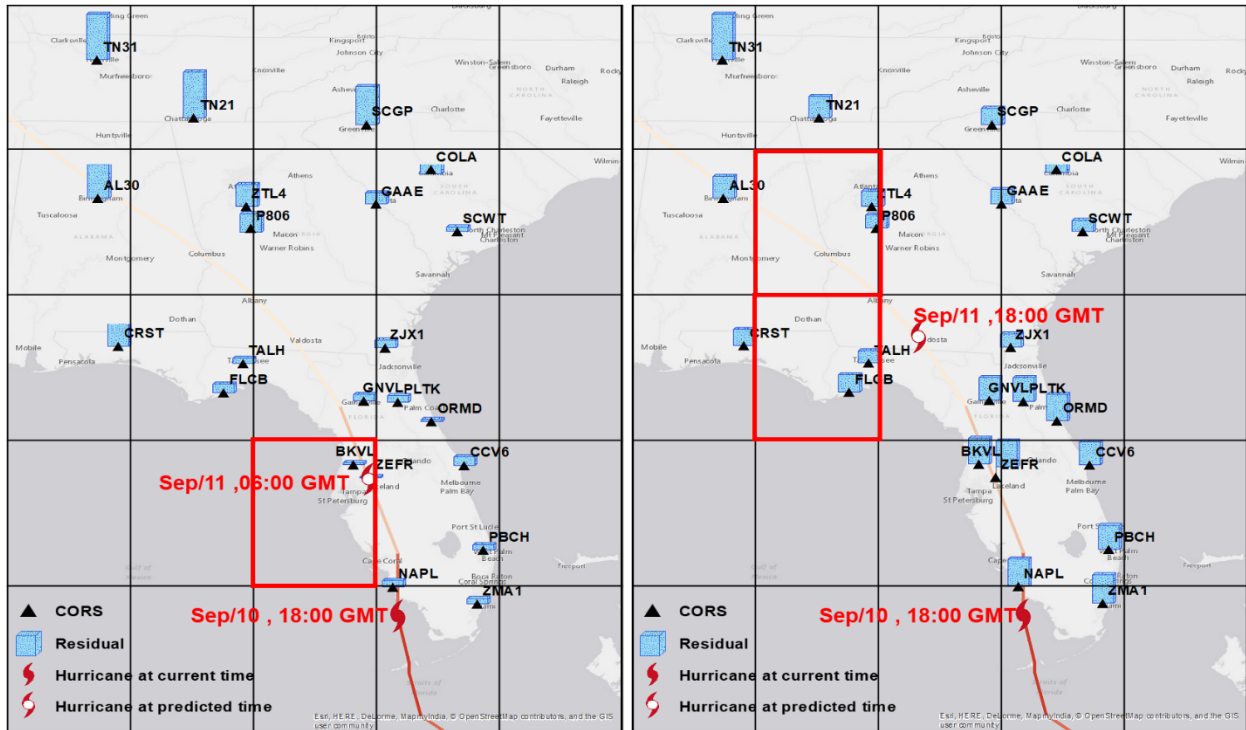
Figure 5-13: Predicted residuals over the study area corresponding to the *right before* model in 12h and 24h prediction lead time in the left panel (Figure 5-13 [a]) and right panel (Figure 5-13 [b]) respectively. Hurricane Irma hit the area close to NAPL on September 10, 2017 at 6 p.m. GMT. The red mark shows the reported time and location of the hurricane provided by NHC

The magnitude of the prediction residuals for the *right before* model is shown in Figures 5-14(a) and 5-14(b) for 12h and 24h later than the reference time. The clustered minimum residuals projected in the red grids indicate that the precipitation path during Hurricane Irma is toward the north and northwest of the reference point for 12h and 24h forecast times, respectively.

42(0)	42 (0)	35(0)		
31(0)	18(1)		8(3)	
22(0)	6(1)	6(0)	4(1)	
		1(0)	6(1)	
		5(0)		

42(0)	20 (0)	15(0)		
20(0)	13(1)		15(1)	
15(0)	13(2)	21(0)	23(1)	
		24(0)	25(1)	
		25(0)		

Figure 5- 14: Residuals and their standard deviation in parentheses (in mm) for the grids inside Hurricane Irma (red cell) and outside Hurricane Irma (white cell). The results in the left panel (Figure 5-14 [a]) and right panel (Figure 5-14 [b]) are attributed to the *right before* prediction model at 6 p.m. GMT on October 10, 2017 (reference time) to predict the PWV after 12h and 24h from the reference time, respectively

Figure 5-15(a) shows that, though the clustered minimum residuals during Hurricane Irma (red grids) reflect the most probable location hit by the hurricane 12h later than the reference time, the amplitude of the distributed residuals projects the severity of the rainfall along the predicted path, which is similar to what radar images reflect as the rainfall intensity.
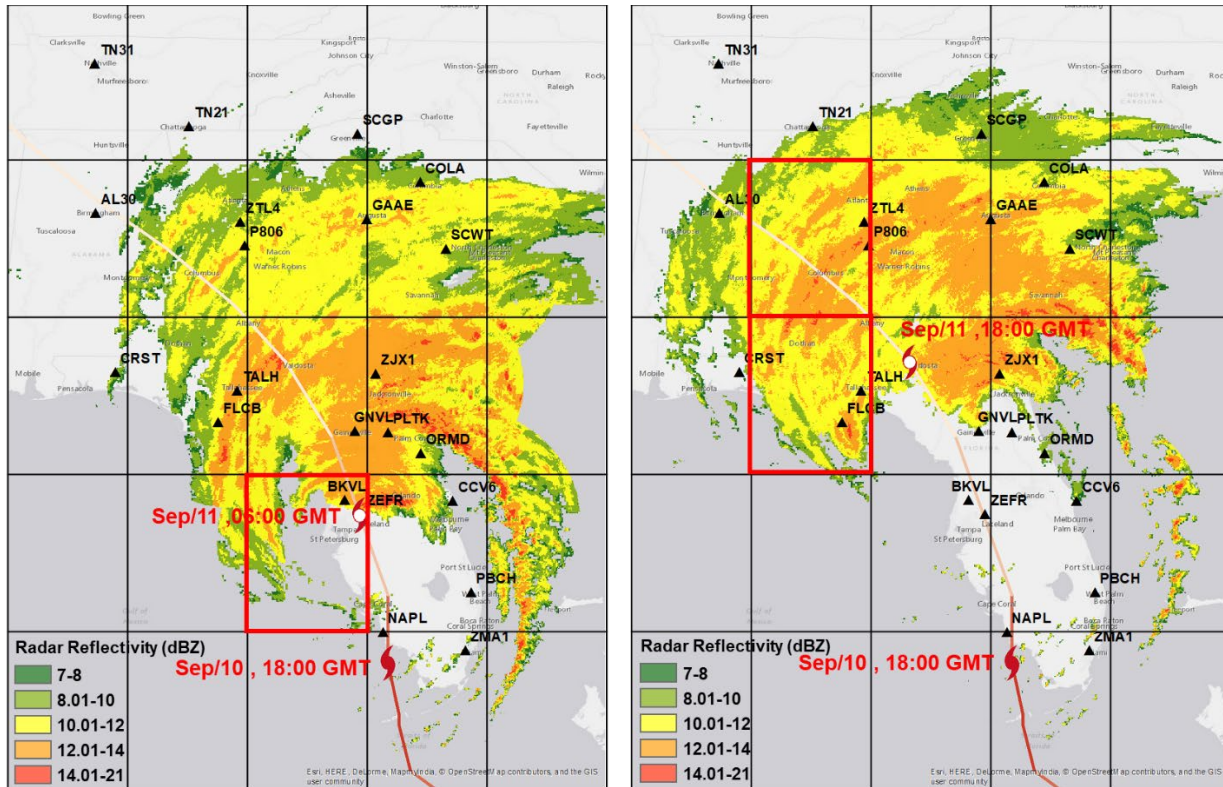
Figure 5-15: The most probable precipitation path during Hurricane Irma. Hurricane Irma hit the area close to NAPL on September 10, 2017 at 6 p.m. GMT (reference time). The results in the left figure (Figure 5-15 [a]) and right figure (Figure 5-15 [b]) are attributed to the right before prediction model at the reference time to predict the precipitation path after 12h and 24h from the reference time, respectively. The red mark shows the reported time and location of the hurricane provided by NHC. Radar reflectivity shows the precipitation over the area at the prediction time

The time series of observed PWV variation during Hurricane Irma are presented in Figure 5-16. The maximum PWV values are observed with a similar trend at the stations close to the hurricane's path, including NAPL and ZEFR. During September 10–11 2017, the maximum PWV are observed at NAPL and then reach ZEFR, showing the precipitation path is from NAPL toward ZEFR. In addition, compared to ZEFR, the PWV values at NAPL are higher, showing more intense rainfall for this station. During that time, PWV values at TALH, CRST, and COLA are fluctuating

below the threshold, showing that these two stations will not be affected by severe rainfall as also shown by Figure 5-15.
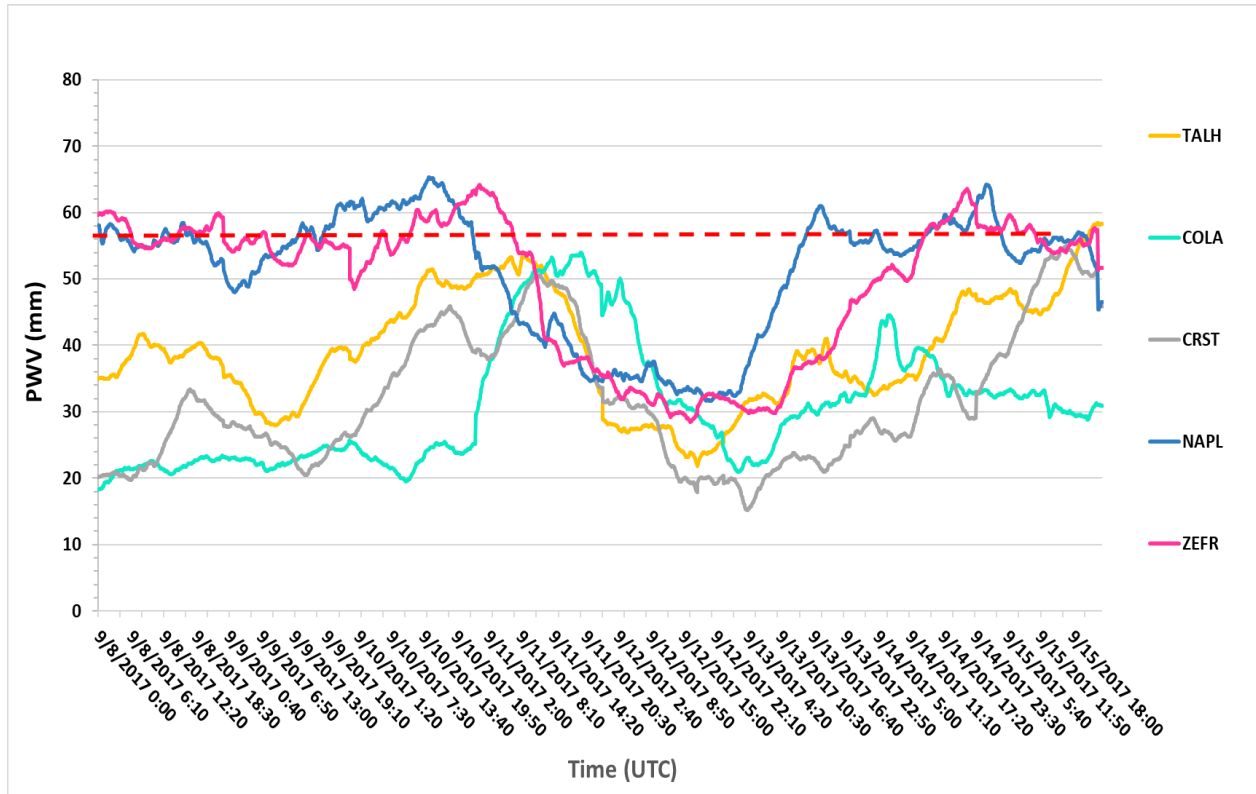
Figure 5-16: Observed PWV variations during Hurricane Irma over the study area. Time series are associated with selected GNSS CORS inside and outside the hurricane's path. The red dashed line shows the applied threshold for PWV forecast, which is set to 55 mm for the Hurricane Harvey case study

Hurricane Florence

The prediction model was also tested for Hurricane Florence, which occurred in 2018. The importance of this case study is that many of the weather prediction models failed to forecast the hurricane's intensity as Florence approached the coastline. As Florence approached the East Coast, it was downgraded, which meant that at landfall in North Carolina it was declared a Category 1

hurricane, while at an earlier stage, it was predicted as a Category 5 hurricane by meteorologists. There is no classification stronger than a Category 5, but because hurricane categories are based mostly on wind speed, they do not reflect the precipitation level in the affected area. Wind speed can fluctuate as hurricanes travel, and storms like Florence ultimately tend to weaken as they pass over land, but that does not guarantee freedom from life-threatening flooding caused by severe precipitation. Therefore, in this case study, the performance of the prediction model proposed in this study is compared to the forecast results derived from hurricane forecast models to reveal the strength of the prediction model for reflecting the path of severe precipitation. To apply the *right before* model, the reference time was set to September 14, 2018 at 6 a.m. GMT when Hurricane Florence made its way toward the coast of the Carolinas. Prediction time lags of 12h and 24h are applied to determine the precipitation path for 12h and 24h later than the reference time. Figures 5-17 (a) and 5-17 (b) demonstrate the prediction results using the *right before* prediction model corresponding to 12h and 24h prediction time lags, respectively. Figures 5-18 (a) and 5-18 (b) represent the magnitude of the residuals for the corresponding models.
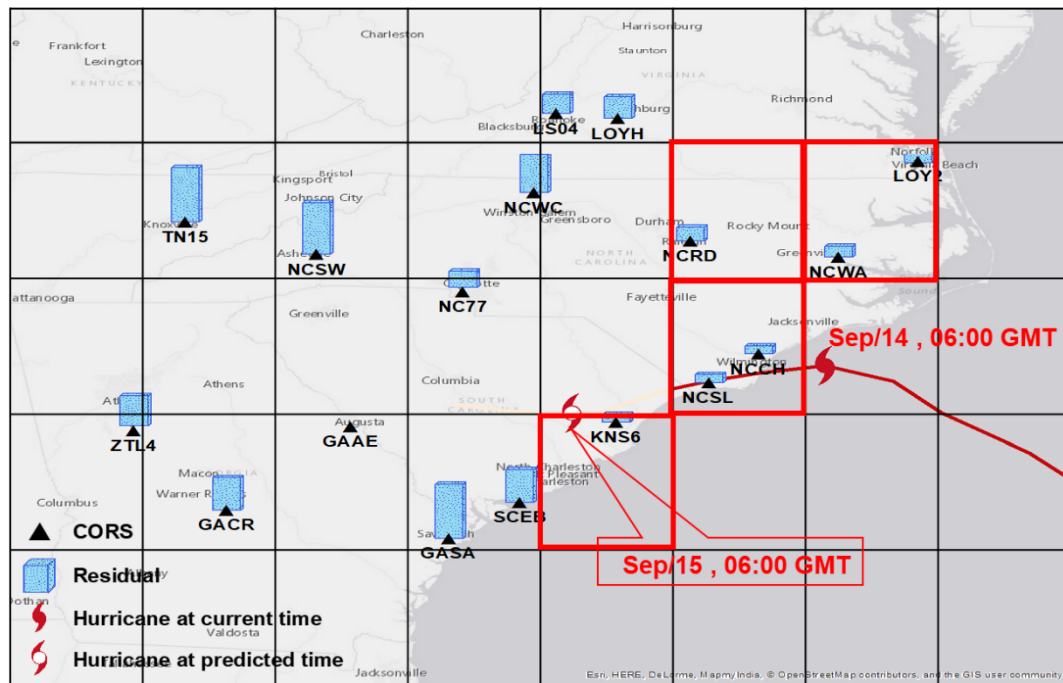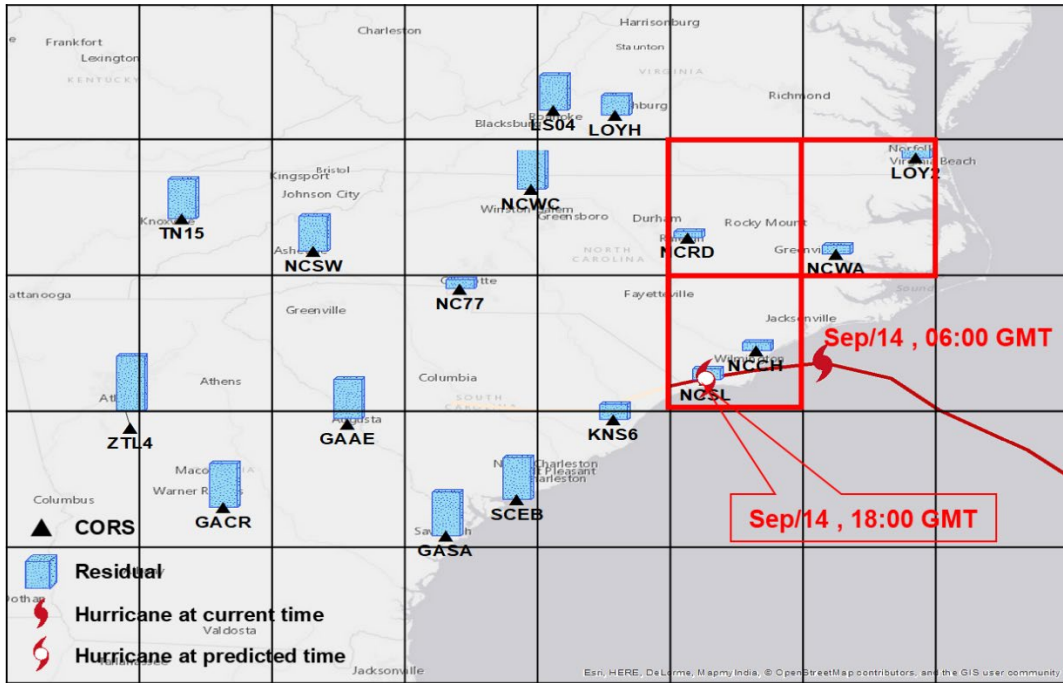
Figure 5-17: Predicted residuals related to Hurricane Florence over the study area corresponding to the right before model in 12h and 24h prediction lead times in the upper panel (Figure 5-17 [a]) and lower panel (Figure 5-17 [b]), respectively. Hurricane Florence hit the ocean on September 14, 2018 at 6 a.m. GMT. The red mark shows the reported time and location of the hurricane provided by NHC

As Figure 5-17 (a) shows, the severe precipitation path is toward North Carolina after 12h from the reference time. Figure 5-17 (b) shows that after 24h from the reference time, while large portions of North Carolina still experience intense rainfall, the storm also affects the South Carolina coastline with severe precipitation. Figures 5-18 (a) and 5-18 (b) show the numerical comparison of the magnitude of the prediction models' residuals. Comparing the location of red cells and corresponding magnitude of the residuals in these figures reveals that even after 24h from the reference time, almost exactly the same area is affected by severe precipitation with almost the same intensity.

Left panel (Figure 5-18 [a]):

				12(4)			
	18(0)	16(0)	18(0)		3(0)	3(0)	
			4(0)		3(1)		
25(0)	20(0)	18(0)	19(1)	7(0)			

Right panel (Figure 5-18 [b]):

				7(1)			
	20(0)	19(0)	14(0)		4(0)	4(0)	
			6(0)		4(1)		
11(0)	12(0)	16(0)	16(2)	4(0)			

Figure 5-18: Residuals and their standard deviation in parenthesis (in mm) for the grids inside Hurricane Florence (red cell) and outside Hurricane Florence (white cell). The results in the left panel (Figure 5-18 [a]) and right panel (Figure 5-18 [b]) are attributed to the right before prediction model at 6 a.m. GMT on September 14, 2018 (reference time) to predict the PWV after 12h and 24h from the reference time, respectively

Though in both cases the red grid cell contains the NHC-reported hurricane center at the prediction time, the direction of the precipitation path during the hurricane's lifespan is slightly different from the NHC-projected path. Figures 5-19 (a) and 5-19 (b) demonstrate the comparison of the prediction results with respect to two other sources: NHC-reported hurricane path and radar

base reflectivity image. Both figures show that the red cells within the study area are located in the most intense precipitation projected by the radar base reflectivity image. However, the NHC-predicted path does not pass through the parts with the intense rainfall and therefore cannot fully project the severe precipitation path. For example, in Figure 5-19 (a), NCSL is the CORS station closed by the NHC-predicted hurricane center 12h after the reference time. This station shows the minimum magnitude of the prediction residuals and is also located in the high precipitation intensity reflected by the radar image. Meanwhile, 24h after the reference time, as Figure 5-19 (b) shows, KNS6 is the closest station to the NHC hurricane center and is along the NHC-predicted path at the prediction time. This station falls within the area with lower intensity of precipitation as shown by the radar reflectivity map. However, the NHC hurricane path does not project the precipitation path; referring to Figure 5-4, the NHC-predicted path shows clearly that the storm was downgraded from the category of hurricane at 6 p.m. on September 14, 2018 to tropical storm at 6 a.m. on September 15, 2018, which is similar to what the radar intensity map shows for the aforementioned prediction times.
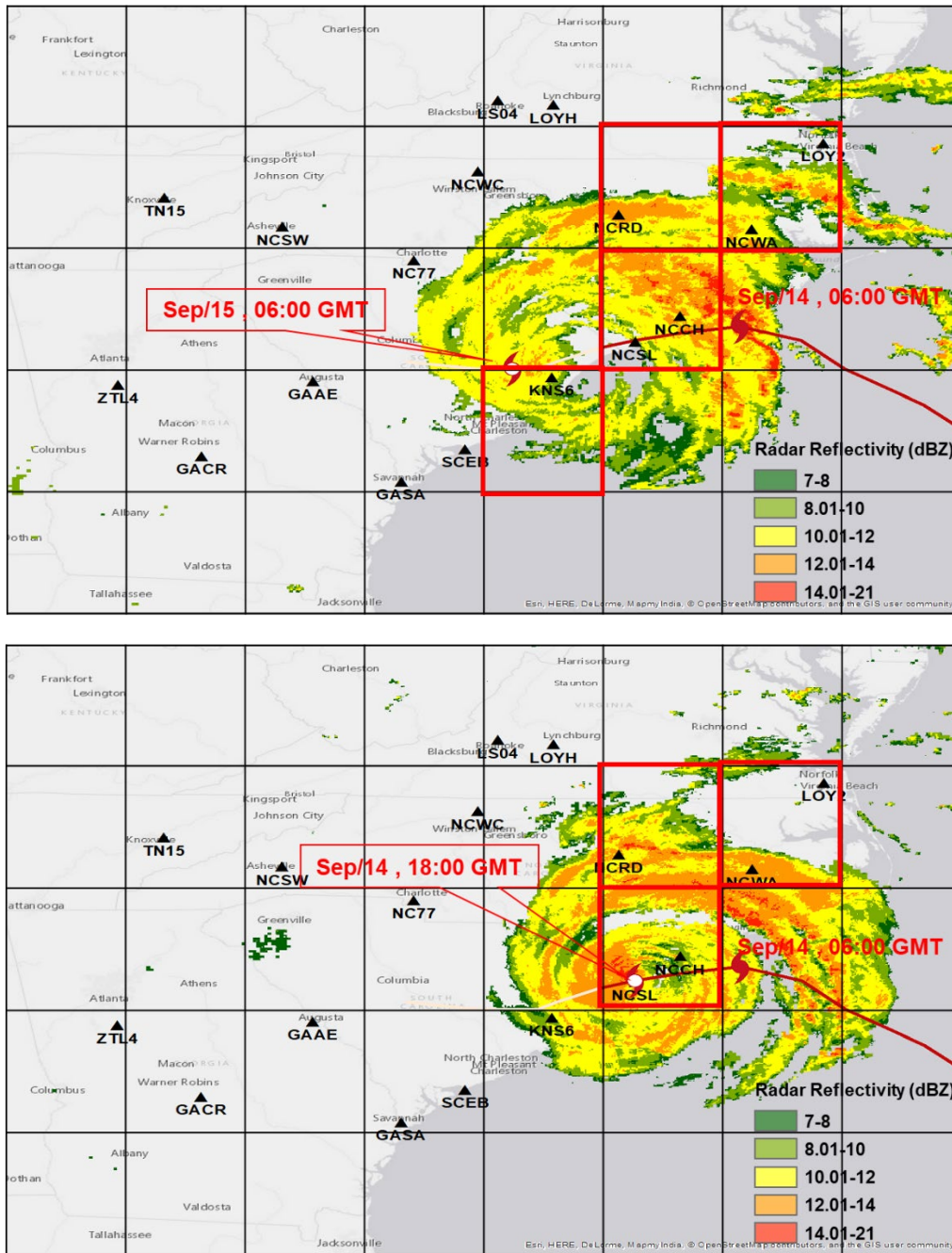
Figure 5-19: The most probable precipitation path during Hurricane Florence. Hurricane Florence hit the ocean on September 14, 2018 at 6 a.m. GMT (reference time). The results in the upper figure (Figure 5-16 [a]) and lower figure (Figure 5-16 [b]) are attributed to the right before prediction model at the reference time to predict the precipitation path after 12h and 24h from the reference time, respectively. The red mark shows the reported time and location of the hurricane provided by NHC. Radar reflectivity shows the precipitation over the area at the prediction time

Figure 5-20 demonstrates the observed PWV variation at sample CORSs during the Hurricane Florence observation time. Among the listed stations in Figure 5-20, ZTLA, GAAE, and NCSW are examples of CORSs in the study area with the consistent PWV variations below the threshold. Considering Figure 5-19, these stations are not located either along the hurricane path or in the precipitation area. Figure 5-20 also shows that, despite the distance between the NCWA location and the reported hurricane path, PWV fluctuates above the threshold mostly during September 14 and 15, 2018, which is an indication of precipitation in this area during that time. This is also confirmed by Figure 5-19 showing the relative intense rainfall over NCWA at that time.
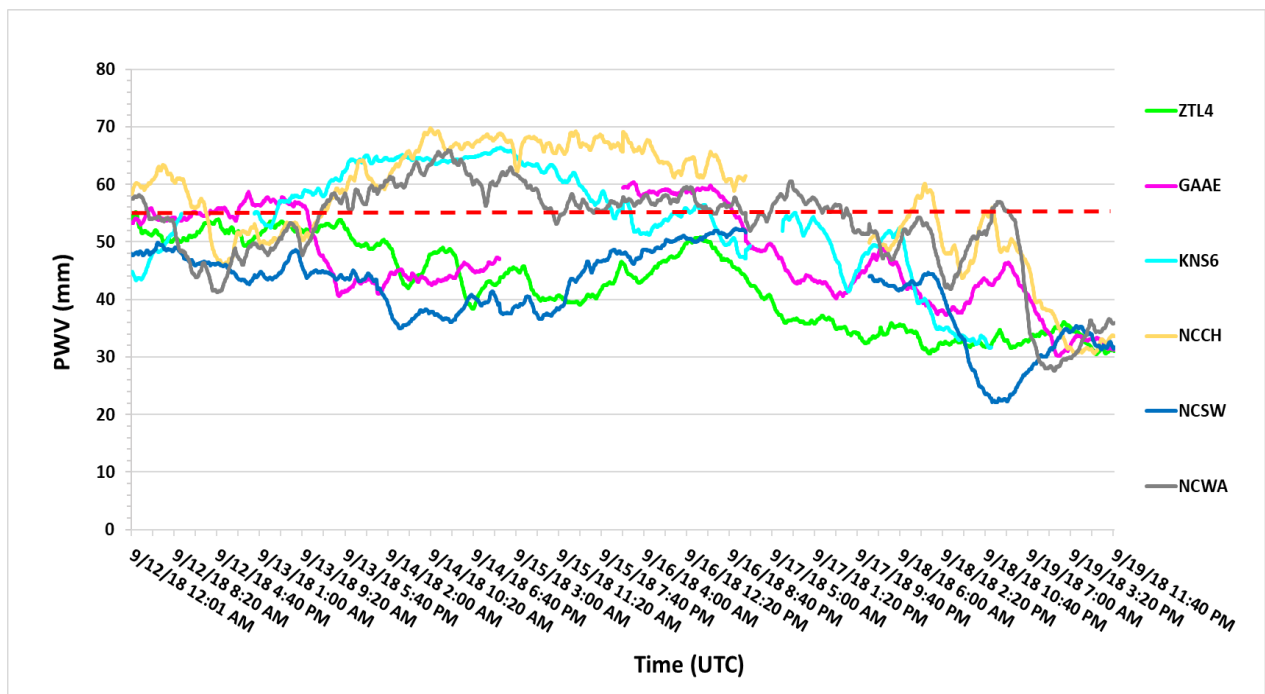
Figure 5-20: Observed PWV variations during Hurricane Florence over the study area. Time series are associated with selected GNSS CORS inside and outside the hurricane's path. The red dashed line shows the applied threshold for PWV forecast, which is set to 55 mm for the Hurricane Harvey case study

On the other hand, for NCCH and KBS6, the PWV fluctuations are above the threshold during the hurricane's reported time. Compared to KNS, NCCH shows the higher PWV values during the same time period of September 14–16 2018, which can be an indicator of more severe rainfall at NCCH at that time. The more severe precipitation at NCCH compared to other stations is also shown in Figure 5-19 using the radar images.

5.3. Summary of the results and comparison

Because various hurricanes have their own spatial and temporal characteristics, the prediction model was applied to several hurricane events to validate the model's performance. In this section, the results for all case studies are compared and discussed. Table 5-2 shows the comparison of hurricane characteristics at the reference and prediction times. The reference time is the time for which the hurricane exists in the area, and the input data used in the prediction model is associated with the reference time. In this study the prediction times are 12h and 24h after the reference time. According to the table for all hurricane cases, the intensity was downgraded over time. The hurricane's intensity is shown by the storm scale in the table. Except for Hurricane Matthew, all other hurricanes were degraded to tropical storms after 24h from the associated reference time. In the table the major difference between the predicted location of the severe precipitation and reported NHC hurricane landfall centers are associated with a time when the storm was downgraded to a tropical storm. As discussed earlier in Figures 5-13 and 5-16, for these cases the NHC-reported hurricane centers are not aligned with the intense part of precipitation reflected by the radar reflectivity map, while the predicted locations from the *right before* model are well matched with the most intense rainfall. This can be considered as the model's strength point to predict the path of most intense precipitation during the hurricanes. The table also shows the probability of the minimum residuals for each case study. It shows that predicted locations (cells) are contained at maximums less than 25% and 32% of total residuals in the area for 12h and 24h prediction time lags, respectively. Among all hurricane case studies, the predicted location during Hurricanes Irma and Florence for the 12h prediction time lag shows the lowest rate of residuals that can be related to the lower hurricane scale for said hurricanes at that time. As the table shows for the 12h prediction time lag, the minimum residual percentage is 5% and 19% of

total residuals for Hurricanes Irma and Florence respectively, and the storm scale at that time is hurricane category 1. Meanwhile, for other cases in the 12h prediction time lag, the predicted locations fall into the area with the higher storm scale, and therefore the percentage of minimum residual with respect to the total residuals is higher.

Table 5-2: Comparison of the hurricane characteristics and prediction results

Storm Name	Time	"right before" model Prediction			NHC Prediction			
		LAT	LON	Intensity % of total residuals	LAT	LON	Storm Type	Storm Scale
Matthew	2016100709				28.2	-80	Hurricane	3
	2016100721	29.8	-81.5	25%	30.2	-80.7	Hurricane	3
	2016100809	32.4	-80.5	24%	32	-80.5	Hurricane	2
Harvey	2017082518				27.1	-96.3	Hurricane	3
	2017082606	28.4	-97.7	21%	28.2	-97.1	Hurricane	3
	2017082618	29.8	-94.9	24%	29	-97.5	Tropical Storm	0
Irma	2017091018				25.6	-81.7	Hurricane	3
	2017091106	28.5	-82.5	5%	28.2	-82.2	Hurricane	1
	2017091118	31.4	-85.0	11%	30.9	-83.5	Tropical Storm	0
Florence	2018091406				34.2	-77.2	Hurricane	1
	2018091418	35.2	-78.2	19%	34	-78.4	Hurricane	1
	2018091506	33.9	-78.6	32%	33.7	-79.3	Tropical Storm	0

reference time	12h predictions time	24h prediction time

CHAPTER 6

6. Conclusion

Highly accurate atmospheric water vapor measurements are important in monitoring the Earth's weather system. Different methods and techniques are used to measure the water content in the atmosphere, and GNSS is one of them. While the primary use of a GNSS is PNT, various GNSS applications have emerged over recent decades that include GNSS meteorology. GNSS meteorology remotely senses the atmospheric constituents in the neutral atmosphere—mostly in the troposphere—using GNSS to deliver information about the state of the atmosphere. The troposphere is the densest and heaviest layer in the atmosphere, holding almost all atmospheric water vapor. PWV is the total amount of water vapor in a column of air above the earth's surface that varies rapidly with short temporal and spatial scale during severe meteorological phenomena. The amount of PWV contained in the neutral atmosphere can be retrieved from GNSS signals received by ground-based GNSS observations. GNSS is an excellent tool in that it is not affected by weather conditions (e.g., presence of clouds, which pose a challenge to traditional weather monitoring technologies). Another benefit of GNSS is the data availability and accessibility. Currently, the densely distributed CORS network provides seamless observations with a high temporal resolution as well as a continuously improving spatial resolution up to a few kilometers for some local networks.

This dissertation was focused on developing a PWV prediction model using GNSS observations to monitor and forecast the path of severe precipitations induced by hurricanes. The dynamic perturbations of PWV as a result of hurricanes were detected from the tropospheric observations of GNSS signals. By analyzing GNSS-based PWV with the local atmospheric

elements that were temperature and pressure, the formation process of a severe precipitation was observed by assessing the correlation among atmospheric pressure, temperature, and PWV. The author of this study derived a PWV prediction model by numerically analyzing the meteorological constituents using a multivariate regression model. In developing the prediction model, the high correlation between variables can cause parameter estimates to be inaccurate and unreliable. To avoid the correlation effect between those variables, a PCR was performed. By using the GNSS-derived PWV and meteorological variables, the trend of the water vapor distribution was determined for the time frames of *before*, *during*, and *after* the severe precipitation. For each time frame a unique prediction model was developed. The developed model can forecast the severe precipitation track induced by a hurricane up to 24 hours in advance. In this dissertation the prediction models were examined using a proposed statistical model for different types of hurricanes. The case studies were: 1) Hurricane Mathew in 2016, 2) Hurricane Harvey in 2017, 3) Hurricane Irma in 2017, and 4) Hurricane Florence in 2018. In each hurricane case study, the patterns of the GNSS-derived PWV fluctuations were analyzed. In particular, a sudden and sharp increment in the PWV, followed by sharp descending trends, was observed a few hours prior to the onset of precipitation. Furthermore, the predicted PWV rate of change was dramatically increased prior to a severe precipitation. Moreover, in each case study, the probability of precipitation rapidly increased when the PWV reached a threshold in the range of 50–55 mm. The threshold was determined by analyzing the correlation between PWV fluctuations and occurrence of rainfall during the hurricane's lifetime. The threshold was applied for classification of prediction models into the *right before*, *during*, and *right after* models based on the hurricane development stage. It should be emphasized that this study was especially focused on the *right before* model, which was the most useful model to analyze the movement of the hurricane.

The proposed method was validated by analyzing the distribution pattern of the predicted PWV residual, its magnitude, and the actual observed PWV in the test site. For a robust analysis considering the uncertainty from the measurement noise and other error sources in the GNSS-derived PWV, the prediction residual at multiple sites in a local area was evaluated within the grids in the test area. The grid size was determined with the consideration of the test site and the geometric distribution of available CORS. The highly probable location of heavy precipitation by the grid-based prediction was in good agreement with the observed rain pattern that can be used for predicting the hurricane path. In addition, the negative correlation between the residuals of PWV measurements with the prediction model and the magnitude of precipitation was revealed. This shows that the magnitude of the predicted model residuals can be used for hurricane tracking and potentially applies to evaluation of the storm intensity. The probability of the minimum residuals for each case study was provided. The study showed that predicted locations (cells) were contained at maximums of less than 25% and 32% of total residuals in the area for 12h and 24h prediction time lags, respectively. Among all hurricane case studies, the predicted location during Hurricanes Irma and Florence for the 12h prediction time lag showed the lowest rate of residuals, which can be related to lower hurricane scales for said hurricanes at that time. For the 12h prediction time lag, the minimum residual percentage was 5% and 19% of total residuals for Hurricanes Irma and Florence, respectively, and the storm scale for that time was hurricane category 1. Meanwhile, for other cases in the 12h prediction time lag, the predicted locations fell into the area with the higher storm scale, and therefore, the percentage of minimum residual with respect to the total residuals was higher. It should be noted that the quality and accuracy of meteorological observations and the level of uncertainty in GNSS-derived PWV can influence the prediction results. However, the results were validated by the radar reflectivity map and reported

NHC hurricane landfall centers. The results, showing a major difference between the predicted location of the severe precipitation and reported NHC hurricane landfall centers, were associated with a time when the storm was downgraded to a tropical storm. For these cases, the NHC-reported hurricane centers were not aligned to the intense part of precipitation reflected by the radar reflectivity map, while the predicted locations from the right before model were well matched with the most intense rainfall. This can be considered as the model's strength point to predict the path of more intense precipitation during the hurricanes. The proposed prediction model can be improved by automation of residuals grouping through applying an automatic clustering approach and ML technique. In addition, because the processes responsible for the formation of the perceptible water suspended in the atmosphere are highly complex and nonlinear, determining a fixed value of threshold from GNSS-derived PWV may not be sufficient to predict the severe precipitation in different scenarios. Moreover, it can be dependent on the geographic locations. Therefore, more exploration is needed for the accurate threshold detection and is left for future investigation. The parametrization for a prediction model can be further expanded by considering the wind effect on the trace and intensity of the hurricane. Furthermore, owing to the complexity of the dynamics in the meteorological parameters' behavior, the nonlinear characteristics of the atmospheric parameters in forming storms and hurricanes can be explored to refine the model. The current model considers a linear relationship between parameters, and any nonlinear behavior can be tested in the future. This study demonstrates the feasibility of GNSS for monitoring severe precipitations and proves the effectiveness of the statistical model for forecasting the precipitation path during the hurricane that is potentially applied to a hazard early warning system.

BIBLIOGRAPHY

Akilan, A, K K Abdul Azeez, S Balaji, H Schuh, and Y Srinivas. 2015. "GPS Derived Zenith Total Delay (ZTD) Observed at Tropical Locations in South India during Atmospheric Storms and Depressions." Journal of Atmospheric and Solar-Terrestrial Physics 125–126:1–7. https://doi.org/https://doi.org/10.1016/j.jastp.2015.02.003.

Albert, P, R Bennartz, and J Fischer. 2001. "Remote Sensing of Atmospheric Water Vapor from Backscattered Sunlight in Cloudy Atmospheres." Journal of Atmospheric and Oceanic Technology 18 (6):865–74.

https://doi.org/10.1175/1520-0426(2001)018<0865:RSOAWV>2.0.CO;2.

Antonio, Andrea. (2013), "Atmospheric probabilistic retrieval through GNSS signals." PhD diss., Tor Vergata University.

Askne, J, and H Nordius. 1987. "Estimation of Tropospheric Delay for Microwaves from Surface Weather Data." Radio Science 22 (3). John Wiley & Sons, Ltd:379–86. https://doi.org/10.1029/RS022i003p00379.

Banville, Simon, and Richard B Langley. 2013. "Mitigating the Impact of Ionospheric Cycle Slips in GNSS Observations." Journal of Geodesy 87 (2):179–93. https://doi.org/10.1007/s00190-012-0604-1.

Banville, Simon, Santerre, Rock, Cocard, Marc, Langley, Richard B., "Satellite and Receiver Phase Bias Calibration for Undifferenced Ambiguity Resolution," *Proceedings of the 2008 National Technical Meeting of The Institute of Navigation*, San Diego, CA, January 2008, pp. 711-719.

Bayram, Ahmet. (2016), "Multi-GNSS Precise Point Positioning Using GPS, GLONASS and Galileo." Master's thesis., The Ohio State University.

Bender, Michael, Ralf Stosius, Florian Zus, Galina Dick, Jens Wickert, and Armin Raabe. 2011. "GNSS Water Vapour Tomography – Expected Improvements by Combining GPS, GLONASS and Galileo Observations." Advances in Space Research 47 (5):886–97. https://doi.org/https://doi.org/10.1016/j.asr.2010.09.011.

Benevides, P, J Catalao, and P M A Miranda. 2015. "On the Inclusion of GPS Precipitable Water Vapour in the Nowcasting of Rainfall." Natural Hazards and Earth System Sciences 15 (12):2605–16. https://doi.org/10.5194/nhess-15-2605-2015.

Bennartz, Ralf, and Jürgen Fischer. 2001. "Retrieval of Columnar Water Vapour over Land from Backscattered Solar Radiation Using the Medium Resolution Imaging Spectrometer." Remote Sensing of Environment 78 (3):274–83.

https://doi.org/https://doi.org/10.1016/S0034-4257(01)00218-8.

Bevis, Michael, Steven Businger, Thomas A Herring, Christian Rocken, Richard A Anthes, and Randolph H Ware. 1992. "GPS Meteorology: Remote Sensing of Atmospheric Water Vapor Using the Global Positioning System." Journal of Geophysical Research: Atmospheres 97 (D14). John Wiley & Sons, Ltd:15787–801. https://doi.org/10.1029/92JD01517.

Blewitt, Geoffrey. 1990. "An Automatic Editing Algorithm for GPS Data." Geophysical Research Letters 17 (3). John Wiley & Sons, Ltd:199–202. https://doi.org/10.1029/GL017i003p00199.

Bilich, Andria, Penina Axelrad, and KM Larson. 2007. "Scientific Utility of the Signal-to-Noise Ratio (SNR) Reported by Geodetic GPS Receivers.", of the Satellite Division of the , 1999–

2010.

Boehm, Johannes, Birgit Werl, and Harald Schuh. 2006. "Troposphere Mapping Functions for GPS and Very Long Baseline Interferometry from European Centre for Medium-Range Weather Forecasts Operational Analysis Data." Journal of Geophysical Research: Solid Earth 111 (B2). John Wiley & Sons, Ltd. https://doi.org/10.1029/2005JB003629.

Boniface, K, V Ducrocq, G Jaubert, X Yan, P Brousseau, F Masson, C Champollion, J Chery, and E Doerflinger. 2009. "Impact of High-Resolution Data Assimilation of GPS Zenith Delay on Mediterranean Heavy Rainfall Forecasting." ANNALES GEOPHYSICAE 27 (7):2739–53. https://doi.org/10.5194/angeo-27-2739-2009.

Bordi, Isabella, Tayeb Raziei, Luis Santos Pereira, and Alfonso Sutera. 2015. "Ground-Based GPS Measurements of Precipitable Water Vapor and Their Usefulness for Hydrological Applications." Water Resources Management 29 (2):471–86.

https://doi.org/10.1007/s11269-014-0672-5.

Cai, Changsheng, Chang He, Rock Santerre, Lin Pan, Xianqiang Cui, and Jianjun Zhu. 2016. "A Comparative Analysis of Measurement Noise and Multipath for Four Constellations: GPS, BeiDou, GLONASS and Galileo." Survey Review 48 (349). Taylor & Francis:287–95. https://doi.org/10.1179/1752270615Y.0000000032.

Cai, Changsheng, Zhizhao Liu, Pengfei Xia, and Wujiao Dai. 2013. "Cycle Slip Detection and Repair for Undifferenced GPS Observations under High Ionospheric Activity." GPS Solutions 17 (2):247–60. https://doi.org/10.1007/s10291-012-0275-7.

Cao, Yujing, Hang Guo, Rongwei Liao, and Marcin Uradzinski. 2016. "Analysis of Water Vapor

Characteristics of Regional Rainfall around Poyang Lake Using Ground-Based GPS Observations." Acta Geodaetica et Geophysica 51 (3):467–79. https://doi.org/10.1007/s40328-015-0137-1.

Champollion, C, F Masson, J Van Baelen, A Walpersdorf, J Chéry, and E Doerflinger. 2004. "GPS Monitoring of the Tropospheric Water Vapor Distribution and Variation during the 9 September 2002 Torrential Precipitation Episode in the Cévennes (Southern France)." Journal of Geophysical Research: Atmospheres 109 (D24). John Wiley & Sons, Ltd. https://doi.org/10.1029/2004JD004897.

COLLINS, PAUL, SUNIL BISNATH, FRANÇOIS LAHAYE, and PIERRE HÉROUX. 2010. "Undifferenced GPS Ambiguity Resolution Using the Decoupled Clock Model and Ambiguity Datum Fixing." NAVIGATION 57 (2). John Wiley & Sons, Ltd:123–35. https://doi.org/10.1002/j.2161-4296.2010.tb01772.x.

Dai, Zhen. 2012. "MATLAB Software for GPS Cycle-Slip Processing." GPS Solut. 16 (2). Berlin, Heidelberg: Springer-Verlag:267–272.

Dai, Zhen, Stefan Knedlik, and Otmar Loffeld. 2009a. "Instantaneous Triple-Frequency GPS Cycle-Slip Detection and Repair." International Journal of Navigation and Observation 2009:1–15.

Dayan, U, K Nissen, and U Ulbrich. 2015. "Review Article: Atmospheric Conditions Inducing Extreme Precipitation over the Eastern and Western Mediterranean." Natural Hazards and Earth System Sciences 15 (11). Department of Geography, Hebrew University of Jerusalem, Jerusalem, Israel ; Institute of Meteorology, Free University of Berlin, Berlin, Germany ; Department of Geography, Hebrew University of Jerusalem, Jerusalem, Israel: Copernicus

GmbH:2525–44. https://doi.org/http://dx.doi.org/10.5194/nhess-15-2525-2015.

El-Mowafy, A. and Deo, M. 2015. "Cycle Slip and Clock Jump Repair with Multi-Frequency Multi-Constellation GNSS data for Precise Point Positioning." Proceedings of the International Global Navigation Satellite Systems Society (IGNSS) Symposium, Jul 14-16 2015, pp. 1-15. Burleigh Heads, Qld., Australia: IGNSS.

England, Martin N, R A Ferrare, S H Melfi, D N Whiteman, and T A Clark. 1992. "Atmospheric Water Vapor Measurements: Comparison of Microwave Radiometry and Lidar." Journal of Geophysical Research: Atmospheres 97 (D1). John Wiley & Sons, Ltd:899–916. https://doi.org/10.1029/91JD02384.

Gao, Bo-Cai, and Yoram J. Kaufman. 2003a. "Water Vapor Retrievals Using Moderate Resolution Imaging Spectroradiometer (MODIS) near-Infrared Channels." Journal of Geophysical Research: Atmospheres 108 (D13):n/a-n/a. https://doi.org/10.1029/2002JD003023.

Gao, Bo-Cai, and Yoram J Kaufman. 2003b. "Water Vapor Retrievals Using Moderate Resolution Imaging Spectroradiometer (MODIS) near-Infrared Channels." Journal of Geophysical Research: Atmospheres 108 (D13). John Wiley & Sons, Ltd.

https://doi.org/10.1029/2002JD003023.

Gao, Xiao, Wujiao Dai, Zhiyong Song, and Changsheng Cai. 2017. "Reference Satellite Selection Method for GNSS High-Precision Relative Positioning." Geodesy and Geodynamics 8 (2):125–29. https://doi.org/https://doi.org/10.1016/j.geog.2016.07.007.

Ge, M, G Gendt, M Rothacher, C Shi, and J Liu. 2008. "Resolution of GPS Carrier-Phase Ambiguities in Precise Point Positioning (PPP) with Daily Observations." Journal of Geodesy

82 (7):389–99. https://doi.org/10.1007/s00190-007-0187-4.

Geng, Jianghui, Chuang Shi, Maorong Ge, Alan H Dodson, Yidong Lou, Qile Zhao, and Jingnan Liu. 2012. "Improving the Estimation of Fractional-Cycle Biases for Ambiguity Resolution in Precise Point Positioning." Journal of Geodesy 86 (8):579–89. https://doi.org/10.1007/s00190-011-0537-0.

Gradinarsky, L P, J M Johansson, H R Bouma, H.-G. Scherneck, and G Elgered. 2002. "Climate Monitoring Using GPS." Physics and Chemistry of the Earth, Parts A/B/C 27 (4):335–40. https://doi.org/https://doi.org/10.1016/S1474-7065(02)00009-8.

Guo, Fei, and Xiaohong Zhang. 2014. "Real-Time Clock Jump Compensation for Precise Point Positioning." GPS Solutions 18 (1):41–50. https://doi.org/10.1007/s10291-012-0307-3.

Gutman, Seth I, and Stanley G Benjamin. 2001. "The Role of Ground-Based GPS Meteorological Observations in Numerical Weather Prediction." GPS Solutions 4 (4). NOAA Forecast Systems Laboratory, 325 Broadway, Boulder, CO 80305, US ; NOAA Forecast Systems Laboratory, 325 Broadway, Boulder, CO 80305, US: Springer Nature B.V.:16–24. https://doi.org/http://dx.doi.org/10.1007/PL00012860.

Haase, Jennifer, Maorong Ge, Henrik Vedel, and Eric Calais. 2003. "Accuracy and Variability of GPS Tropospheric Delay Measurements of Water Vapor in the Western Mediterranean." Journal of Applied Meteorology 42 (11):1547–68. https://doi.org/10.1175/1520-0450(2003)042<1547:AAVOGT>2.0.CO;2.

Hofmann-Wellenhof, Bernhard, Herbert Lichtenegger, and Elmar Wasle. 2008. "GNSS – Global Navigation Satellite Systems."

Håkansson, Martin, Anna B O Jensen, Milan Horemuz, and Gunnar Hedling. 2017. "Review of Code and Phase Biases in Multi-GNSS Positioning." GPS Solutions 21 (3):849–60. https://doi.org/10.1007/s10291-016-0572-7.

Hasler, A F, K Palaniappan, C Kambhammetu, P Black, E Uhlhorn, and D Chesters. 1998. "High-Resolution Wind Fields within the Inner Core and Eye of a Mature Tropical Cyclone from GOES 1-Min Images." Bulletin of the American Meteorological Society 79 (11):2483–96. https://doi.org/10.1175/1520-0477(1998)079<2483:HRWFWT>2.0.CO;2.

Huang, Lingyong, Zhiping Lu, Guojun Zhai, Yongzhong Ouyang, Motao Huang, Xiuping Lu, Taiqi Wu, and Kaifeng Li. 2016. "A New Triple-Frequency Cycle Slip Detecting Algorithm Validated with BDS Data." GPS Solutions 20 (4):761–69. https://doi.org/10.1007/s10291-015-0487-8.

Jade, Sridevi, M S M Vijayan, V K Gaur, Tushar P Prabhu, and S C Sahu. 2005. "Estimates of Precipitable Water Vapour from GPS Data over the Indian Subcontinent." Journal of Atmospheric and Solar-Terrestrial Physics 67 (6):623–35.

https://doi.org/https://doi.org/10.1016/j.jastp.2004.12.010.

Jin, Shuanggen, Jong-Uk Park, Jung-Ho Cho, and Pil-Ho Park. 2007. "Seasonal Variability of GPS-Derived Zenith Tropospheric Delay (1994–2006) and Climate Implications." Journal of Geophysical Research: Atmospheres 112 (D9). John Wiley & Sons, Ltd. https://doi.org/10.1029/2006JD007772.

Kazmierski, Kamil; Hadas, Tomasz; Sośnica, Krzysztof. 2018. "Weighting of Multi-GNSS Observations in Real-Time Precise Point Positioning." Remote Sens. 10, no. 1: 84.

Kiely, Gerard, John D Albertson, Marc B Parlange, and Richard W Katz. 1998. "Conditioning Stochastic Properties of Daily Precipitation on Indices of Atmospheric Circulation." Meteorological Applications 5 (1). John Wiley & Sons, Ltd:75–87.

https://doi.org/10.1017/S1350482798000656.

Kouba, J. 2003. "A Guide To Using International Gnss Service (Igs) Products." In .

Krypiak-Gregorczyk, Anna; Wielgosz, Pawel; Borkowski, Andrzej. 2017. "Ionosphere Model for European Region Based on Multi-GNSS Data and TPS Interpolation." Remote Sens. 9, no. 12: 1221.

Lacy, Maria Clara de, Mirko Reguzzoni, and Fernando Sansò. 2012. "Real-Time Cycle Slip Detection in Triple-Frequency GNSS." GPS Solutions 16 (3). Departamento Ingeniería Cartográfica, Geodésica y Fotogrametría, Universidad de Jaén, Jaén, Andalusia, Spain ; DIIAR, Politecnico di Milano, Milan, CO, Italy ; DIIAR, Politecnico di Milano, Polo Regionale di Como, Milan, CO, Italy ; Departamento Ingeniería Cartográfica, Geodésica y Fotogrametría, Universidad de Jaén, Jaén, Andalusia, Spain: Springer Nature B.V.:353–62. https://doi.org/http://dx.doi.org/10.1007/s10291-011-0237-5.

Lacy, Maria Clara de, Mirko Reguzzoni, Fernando Sansò, and Giovanna Venuti. 2008. "The Bayesian Detection of Discontinuities in a Polynomial Regression and Its Application to the Cycle-Slip Problem." Journal of Geodesy 82 (9):527–42. https://doi.org/10.1007/s00190-007-0203-8.

Li, Xingxing, Xiaohong Zhang, Xiaodong Ren, Mathias Fritsche, Jens Wickert, and Harald Schuh. 2015. "Precise Positioning with Current Multi-Constellation Global Navigation Satellite Systems: GPS, GLONASS, Galileo and BeiDou." Scientific Reports 5 (1):8328.

https://doi.org/10.1038/srep08328.

Li, Tao. and Melachroninos Stavros. 2016, Real-Time Cycle Slip Detection and Repair for Network Multi-GNSS , Multi-Frequency Data Processing, International Global Navigation Satellite Systems Association IGNSS Conference 2016, Colombo Theatres, Kensington Campus, UNSW Australia 6 – 8 December 2016.

Liu, Zhizhao, Man Sing Wong, Janet Nichol, and P. W. Chan. 2013. "A Multi-Sensor Study of Water Vapour from Radiosonde, MODIS and AERONET: A Case Study of Hong Kong." International Journal of Climatology 33 (1):109–20. https://doi.org/10.1002/joc.3412.

Liu, X. C., Wang, Y. Q. & Zhang, Z. L. "Analysis of Harbin Area Atmosphere Precipitable Water Vapor by Using GPSTechnology." Bull. Surv. Mapp. 4, 10–16 (2006).

Madden, R. A., & Williams, J. (1978). "The correlation between temperature and precipitation in the United States and Europe". Monthly Weather Review, 106, 142-147. doi:10.1175/1520-0493(1978)106<0142:TCBTAP>2.0.CO;2

Manandhar, S, Y H Lee, Y S Meng, F Yuan, and J T Ong. 2018. "GPS-Derived PWV for Rainfall Nowcasting in Tropical Region." IEEE Transactions on Geoscience and Remote Sensing 56 (8):4835–44. https://doi.org/10.1109/TGRS.2018.2839899.

Nash, J., 2015." Measurement of upper-air pressure, temperature and humidity." World Meteorological Organization IOM Rep. No. 121, 87 pp.

Navpedia website, https://gssc.esa.int/navipedia/index.php/Examples_of_multi-frequency_Cycle-Slip_Detectors (Accessed Jan 15, 2020)

Niell, A E. 2001. "Preliminary Evaluation of Atmospheric Mapping Functions Based on

Numerical Weather Models." Physics and Chemistry of the Earth, Part A: Solid Earth and Geodesy 26 (6):475–80. https://doi.org/https://doi.org/10.1016/S1464-1895(01)00087-4.

Ning, Tong. (2012), "GPS Meteorology With Focus on Climate Applications." PhD diss., Department of Earth and Space Sciences, Chalmers University of Technology. https://core.ac.uk/download/pdf/70594409.pdf

Nykiel, Grzegorz, Mariusz Figurski, and Zofia Baldysz. 2019. "Analysis of GNSS Sensed Precipitable Water Vapour and Tropospheric Gradients during the Derecho Event in Poland of 11th August 2017." Journal of Atmospheric and Solar-Terrestrial Physics 193:105082. https://doi.org/https://doi.org/10.1016/j.jastp.2019.105082.

Pan, Lin, Xiaohong Zhang, Xingxing Li, Xin Li, Cuixian Lu, Jingnan Liu, and Qianxin Wang. 2019. "Satellite Availability and Point Positioning Accuracy Evaluation on a Global Scale for Integration of GPS, GLONASS, BeiDou and Galileo." Advances in Space Research 63 (9):2696–2710. https://doi.org/https://doi.org/10.1016/j.asr.2017.07.029.

Pavelyev, A G, Y A Liou, J Wickert, T Schmidt, and A A Pavelyev. 2009. "Phase Acceleration: A New Important Parameter in GPS Occultation Technology." GPS Solutions 14 (1):3. https://doi.org/10.1007/s10291-009-0128-1.

Pielke Jr., R. A., Gratz, J., Landsea, C. W., Collins, D., Saunders, M. A., and Musulin, R.: Normalized Hurricane Damage in the United States: 1900–2005, Natural Hazards Review, 31, 29–42, 2008.

Priego, E, J Jones, M J Porres, and A Seco. 2017. "Monitoring Water Vapour with GNSS during a Heavy Rainfall Event in the Spanish Mediterranean Area." Geomatics, Natural Hazards and Risk 8 (2). Taylor & Francis:282–94. https://doi.org/10.1080/19475705.2016.1201150.

Qianqian, Zhang, and Gui Qingming. 2013. "Bayesian Methods for Outliers Detection in GNSS Time Series." Journal of Geodesy 87 (7):609–27.

https://doi.org/10.1007/s00190-013-0640-5.

Realini, Eugenio, Kazutoshi Sato, Toshitaka Tsuda, Masanori Oigawa, Yuya Iwaki, Yoshinori Shoji, and Hiromu Seko. 2016. "Local-Scale Precipitable Water Vapor Retrieval from High-Elevation Slant Tropospheric Delays Using a Dense Network of GNSS Receivers BT - IAG 150 Years." In , edited by Chris Rizos and Pascal Willis, 485–90. Cham: Springer International Publishing.

Realini, Eugenio, Kazutoshi Sato, Toshitaka Tsuda, Susilo, and Timbul Manik. 2014. "An Observation Campaign of Precipitable Water Vapor with Multiple GPS Receivers in Western Java, Indonesia." Progress in Earth and Planetary Science 1 (1):17. https://doi.org/10.1186/2197-4284-1-17.

Rocken, Christian, Randolph Ware, Teresa Van Hove, Fredrick Solheim, Chris Alber, James Johnson, Mike Bevis, and Steven Businger. 1993. "Sensing Atmospheric Water Vapor with the Global Positioning System." Geophysical Research Letters 20 (23). John Wiley & Sons, Ltd:2631–34. https://doi.org/10.1029/93GL02935.

Sanz Subirana, J., Juan Zornoza, J.M., and Hernández-Pajares., M. 2011. "Antenna Phase Centre." Available at: Gssc.esa.int.

https://gssc.esa.int/navipedia/index.php/Antenna_Phase_Centre [Accessed 13 Nov. 2019].

Sanz Subirana, J., Juan Zornoza, J.M., and Hernández-Pajares., M. 2011." Receiver Antenna Phase Centre". Available at:

https://gssc.esa.int/navipedia/index.php/Receiver_Antenna_Phase_Centre[Accessed 13 Nov. 2019]

Sapucci, L F, L A T Machado, E de Souza, and T B Campos. 2016. "GPS-PWV Jumps before Intense Rain Events." Atmospheric Measurement Techniques Discussions 2016:1–27. https://doi.org/10.5194/amt-2016-378.

Schuler, Torben. (2001), "On Ground-Based Tropospheric Delay Estimation." PhD diss., Univ. der Bundeswehr Mu¨nchen, Neubiberg, Germany.

Seco, Andres, Francisco Ramírez, Eduardo Serna, Eduardo Prieto, Rafael García, Aitor Moreno, Juan Carlos Cantera, Luis Miqueleiz, and Jose Enrique Priego. 2012. "Rain Pattern Analysis and Forecast Model Based on GPS Estimated Atmospheric Water Vapor Content." Atmospheric Environment 49:85–93.

https://doi.org/https://doi.org/10.1016/j.atmosenv.2011.12.019.

Shi, J, C Xu, J Guo, and Y Gao. 2015. "Real-Time GPS Precise Point Positioning-Based Precipitable Water Vapor Estimation for Rainfall Monitoring and Forecasting." IEEE Transactions on Geoscience and Remote Sensing 53 (6):3452–59. https://doi.org/10.1109/TGRS.2014.2377041.

Shirzadi Babakan, Ali, and Abbas Alimohammadi. 2016. "An Agent-Based Simulation of Residential Location Choice of Tenants in Tehran, Iran." Transactions in GIS 20 (1). John Wiley & Sons, Ltd:101–25. https://doi.org/10.1111/tgis.12144.

Shirzadi Babakan, Ali, and Mohammad Taleai. 2015. "Impacts of Transport Development on Residence Choice of Renter Households: An Agent-Based Evaluation." Habitat International

49:275–85. https://doi.org/https://doi.org/10.1016/j.habitatint.2015.05.033.

Shoji, Yoshinori, Hiroshi Yamauchi, Wataru Mashiko, and Eiichi Sato. 2014. "Estimation of Local-Scale Precipitable Water Vapor Distribution Around Each GNSS Station Using Slant Path Delay." SOLA 10:29–33. https://doi.org/10.2151/sola.2014-007.

Strode, Philip R R, and Paul D Groves. 2016. "GNSS Multipath Detection Using Three-Frequency Signal-to-Noise Measurements." GPS Solutions 20 (3):399–412.

https://doi.org/10.1007/s10291-015-0449-1.

Subirana, J.Sanz, J. M.Juan Zornoza, and M. Hernandez-Pajares. 2013. "Gnss Data Processing Volumen I: Fundamentals and Algorithms."

Tahami, Hesamoddin, Abolfazl Mirzazadeh, Alireza Arshadi-khamseh, and Aref Gholami-Qadikolaei. 2016. "A Periodic Review Integrated Inventory Model for Buyer's Unidentified Protection Interval Demand Distribution." Edited by Manoj Kumar Tiwari. Cogent Engineering 3 (1). Cogent OA:1206689. https://doi.org/10.1080/23311916.2016.1206689.

Tahami, Hesamoddin, Abolfazl Mirzazadeh, and Aref Gholami-Qadikolaei. 2019. "Simultaneous Control on Lead Time Elements and Ordering Cost for an Inflationary Inventory-Production Model with Mixture of Normal Distributions LTD under Finite Capacity." RAIRO-Oper. Res. 53 (4):1357–84. https://doi.org/10.1051/ro/2019060.

Tahami, Hoda, Basiri Anahid, Moore Terry, Park Jihye, Bonenberg Lukasz. 2018. "Virtual spatial diversity antenna for GNSS based Mobile positioning in the harsh environments." In: Paper presented at the the 31st international technical meeting of the satellite division of the Institute of Navigation (ION GNSS+ 2018), Miami

Tahami, Hesamoddin, Fakhravar, Hengameh. 2020. "Multilevel Reorder Strategy-based Supply Chain Model." 5th North American Conference on Industrial Engineering and Operations Management (IEOM), Michigan, USA.

Tahami, Hoda, Park Jihye, Choi Yunsoo. 2017. "The Preliminary Study on the Prediction of a Hurricane Path by GNSS Derived PWV Analysis." Paper presented at the Proceedings of the ION 2017 Pacific PNT meeting, Honolulu

Tahami, Hoda, and Park, Jihye. 2020. "Spatial-Temporal Characterization of Hurricane Path Using GNSS-Derived Precipitable Water Vapor: Case Study of Hurricane Matthew in 2016." Geoinformatica: An International Journal 7 (1):1–17.

http://www.cscjournals.org/manuscript/Journals/GIIJ/Volume7/Issue1/GIIJ-31.pdf.

Takasu, Tomoji and Akio Yasuda. 2013. "RTKLIB Ver. 2.4.2 Manual." (C):181.

Teunissen, P J G, and A Khodabandeh. 2015. "Review and Principles of PPP-RTK Methods." Journal of Geodesy 89 (3):217–40. https://doi.org/10.1007/s00190-014-0771-3.

Tian, Fuyou, Yongguang Zheng, Tao Zhang, Xiaoling Zhang, Dongyan Mao, Jianhua Sun, and Sixiong Zhao. 2015. "Statistical Characteristics of Environmental Parameters for Warm Season Short-Duration Heavy Rainfall over Central and Eastern China." Journal of Meteorological Research 29 (3):370–84. https://doi.org/10.1007/s13351-014-4119-y.

Vaclavovic, Pavel, and Jan Dousa. 2016. "G-Nut/Anubis: Open-Source Tool for Multi-GNSS Data Monitoring with a Multipath Detection for New Signals, Frequencies and Constellations BT - IAG 150 Years." In , edited by Chris Rizos and Pascal Willis, 775–82. Cham: Springer International Publishing.

Vedel, H, X.-Y. Huang, J Haase, M Ge, and E Calais. 2004. "Impact of GPS Zenith Tropospheric Delay Data on Precipitation Forecasts in Mediterranean France and Spain." Geophysical Research Letters 31 (2). John Wiley & Sons, Ltd. https://doi.org/10.1029/2003GL017715.

Wang, Y, Z Guo, Y Liu, H Xu, K Ding, and D Wen. 2010. "The Study of Rainfall Forecast Based on Neural Network and GPS Precipitable Water Vapor." In 2010 The 2nd Conference on Environmental Science and Information Application Technology, 1:17–20. https://doi.org/10.1109/ESIAT.2010.5568487.

Weining Zhao, and M. A.K. Khalil. 1993. "The Relationship between Precipitation and Temperature over the Contiguous United States." Journal of Climate.

Xiao, Guorui, Michael Mayer, Bernhard Heck, Lifen Sui, Tian Zeng, and Dongming Zhao. 2017. "Improved Time-Differenced Cycle Slip Detect and Repair for GNSS Undifferenced Observations." GPS Solutions 22 (1):6. https://doi.org/10.1007/s10291-017-0677-7.

Xiaohong, Zhang, and Li Xingxing. 2012. "Instantaneous Re-Initialization in Real-Time Kinematic PPP with Cycle Slip Fixing." GPS Solutions 16 (3):315–27. https://doi.org/10.1007/s10291-011-0233-9.

Yahoodik, Sarah, Tahami Hesamoddin, Unverricht James, Yamani Yusuke, Handley Holly, Thompson Deborah. (2020). "Blink Rate as a Measure of Driver Workload during Simulated Driving." Proceedings of the Human Factors and Ergonomics Society 2020 Annual Meeting, Chicago, IL.

Yao, Yibin, Lulu Shan, and Qingzhi Zhao. 2017. "Establishing a Method of Short-Term Rainfall Forecasting Based on GNSS-Derived PWV and Its Application." Scientific Reports 7 (1):12465. https://doi.org/10.1038/s41598-017-12593-z.

Yu, Chen, Nigel T Penna, and Zhenhong Li. 2017. "Generation of Real-Time Mode High-Resolution Water Vapor Fields from GPS Observations." Journal of Geophysical Research: Atmospheres 122 (3). John Wiley & Sons, Ltd:2008–25.

https://doi.org/10.1002/2016JD025753.

Zhang, Xiaohong, and Pan Li. 2016. "Benefits of the Third Frequency Signal on Cycle Slip Correction." GPS Solutions 20 (3):451–60. https://doi.org/10.1007/s10291-015-0456-2.

Zhao, Dongsheng, Roberts, Gethin Wyn, Hancock, Craig M., Lau, Lawrence, Bai, Ruibin, "Cycle-slip Detection for Triple-frequency GPS Observations Under Ionospheric Scintillation," Proceedings of the 30th International Technical Meeting of the Satellite Division of The Institute of Navigation (ION GNSS+ 2017), Portland, Oregon, September 2017, pp. 4046-4054.

https://doi.org/10.33012/2017.15326

Zhao, Qingzhi, Yibin Yao, Wanqiang Yao, and Zufeng Li. 2018. "Real-Time Precise Point Positioning-Based Zenith Tropospheric Delay for Precipitation Forecasting." Scientific Reports 8 (1):7939. https://doi.org/10.1038/s41598-018-26299-3.

Zhu, S Y, F.-H. Massmann, Y Yu, and Ch. Reigber. 2003. "Satellite Antenna Phase Center Offsets and Scale Errors in GPS Solutions." Journal of Geodesy 76 (11):668–72. https://doi.org/10.1007/s00190-002-0294-1.